

Experimental Biology and Medicine

Editor-in-Chief

Nicola Conran

University of Campinas,
Brazil



SEBM Executive Council

PRESIDENT

Michael Lehman
Kent State University

TREASURER

Jian Feng
State University of New York at Buffalo

PAST PRESIDENT

Stephania Cormier
Louisiana State University

TREASURER ELECT

Louis Justement
University of Alabama Birmingham

PRESIDENT ELECT

Clint Allred
University of North Carolina, Greensboro

Publication Committee

Robert T Mallet '25, Chairperson
Stephanie A Cormier '24,
Muriel Lambert '25,
Aleksander F Sikorski '24

Society for Experimental Biology and Medicine
3220 N Street NW, #179
Washington DC 20007, USA
Executive Director – ed@sebm.org

www.sebm.org

Editorial Board

Editor-in-Chief
Nicola Conran
University of Campinas

DEPUTY EDITOR
Sulev Kõks
Murdoch University

GLOBAL EDITORS

Africa
Gordon Awandare
University of Ghana

Asia
Shaw-Jenq Tsai
National Cheng Kung University

Europe
Farzin Farzaneh
King's College London

Americas
Nicola Conran
University of Campinas

Australia/Oceania
Sulev Kõks
Murdoch University

Anatomy/Pathology

Associate Editor

Ian Zagon
Penn State University College of Medicine

William Banks
Alexander V. Ljubimov

Patricia J. McLaughlin
Artur Pasternak

Biomedical Engineering

Associate Editor

F. Kurtis Kasper
University of Texas Health Science Center at
Houston

Angela Pannier

Artificial Intelligence/Machine Learning Applications to Biomedical Research

Associate Editor

Huixiao Hong
US Food and Drug Administration

Xiaohui Fan
Ping Gong
Ruili Huang
Jie Liu
Fred Prior

Paul Rogers
Tielu Shi
Wei Shi
Wenming Xiao

Bionanoscience

Associate Editor

Juan Melendez
University of Albany

Nathaniel Cady
Hassan A. Elfawal
Jonathan F. Lovell
Ya-Ping Sun

Maria Tomassone
Siyang Zheng

Biochemistry and Molecular Biology

Associate Editor

Muriel A. Lambert
Rutgers New Jersey Medical School

Brian D Adams
Bin Guo

J. Patrick O'Connor

Cell and Developmental Biology

Associate Editor

Lidiane Torres
Albert Einstein College of Medicine

David Dean
Leszek Kotula
Huihui Li

Harold I Saavedra
Yigang Wang
Warren Zimmer

Bioimaging

Associate Editor

Shuliang Jiao
Florida International University

Kamran Avanaki
Zygmunt Gryczynski
Xinmai Yang

Xincheng Yao
Baohong Yuan
Weizhao Zhao

Clinical Trials

Giuseppe Pizzorno
Daniel Vaena

Endocrinology and Nutrition

Co Associate Editors

Clint Allred and Keith Erikson
University of North Carolina Greensboro

Demin Cai
Sam Dagogo-Jack
Weiqun Wang

Malcolm Watford
Chia-Shan Wu

Environmental Health/Biomarkers/Precision Medicine

Associate Editor

William Slikker, Jr.
Retired

Gary Steven Friedman
Donald Johann
Oh-Seung Kwon

Ann M. Marini
Igor Pogribny

Genomics, Proteomics, and Bioinformatics

Associate Editor

Sulev Kõks
Murdoch University

Mark Geraci
Paul Potter

John P Quinn
Giovanni Stracquandano

Immunology/Microbiology/Virology

Co Associate Editors

Flávio Guimarães Da Fonseca
Federal University of Minas Gerais

Renata Sesti-Costa
State University of Campinas

Andrea Doria
Farzin Farzaneh

Kam Hui
Francois Villinger

Mechanisms of Aging

Associate Editor

Shigemi Matsuyama
Case Western Reserve University

Ricki Colman
Aolin Allen Hsu
Akihiro Ikeda

Masaru Miyagi
Vincent Monnier

Neuroscience

Associate Editor

Michael Neal Lehman
Kent State University

Lique M. Coolen
Terrence Deak
Max L. Fletcher

Sandra Mooney
Gregg Stanwood
Richard M Xu

Pharmacology/Toxicology

Associate Editor

Santosh Kumar
University of Tennessee Health Science Center

Guzel Bikbova
Pawel Brzuzan
Laetitia Dou
Jianxiong Jiang
Youngmi Jung
Li-Fu Li

Jonathan Shannahan
Manish Tripathi
Chaowu Xiao
Wuxiang Xie
Qihe Xu

Physiology and Pathophysiology

Associate Editor

Robert T. Mallet
University of North Texas Health Science Center

Rong Ma
Gabor Tigyi
Shaw-Jenq Tsai

Samuel Verges
Lei Xi
Chunyu Zeng

Population Health

Associate Editor

Ashish Joshi
School of Public Health, University of Memphis

Stem Cell Biology

Associate Editor

Jian Feng
State University of New York at Buffalo

Vania Broccoli
Jose Cibelli
Guoping Fan

Antonis Hatzopoulos
Dan S. Kaufman
Chun-Li Zhang

Structural Biology

Associate Editor

Tom Thompson
University of Cincinnati

Andrew P. Hinck
James Horn
Rhett Kovall

Vincent Luca
Rick Page

Synthetic Biology

Tara Deans
Ahmad Khalil

Aditya M. Kunjapur
Kevin Solomon

Systems Biology and Microphysiological Systems

Salman Khetani
Deok-Ho Kim

Andre Levchenko

Translational Research

Associate Editor

Chia-Ching (Josh) Wu
National Cheng Kung University

Jing An
Pan Pan Chong
Hyacinth Idu Hyacinth
Monica M. Jablonski

Chulso Moon
Esther Obeng
Athena Starland-Davenport

EBM eBook Copyright Statement

The copyright in the text of individual articles in this eBook is the property of their respective authors or their respective institutions or funders. The copyright in graphics and images within each article may be subject to copyright of other parties. In both cases this is subject to a license granted to Frontiers.

The compilation of articles constituting this eBook is the property of Frontiers.

Each article within this eBook, and the eBook itself, are published under the most recent version of the Creative Commons CC-BY licence. The version current at the date of publication of this eBook is CC-BY 4.0. If the CC-BY licence is updated, the licence granted by Frontiers is automatically updated to the new version.

When exercising any right under the CC-BY licence, Frontiers must be attributed as the original publisher of the article or eBook, as applicable.

Authors have the responsibility of ensuring that any graphics or other materials which are the property of others may be included in the CC-BY licence, but this should be checked before relying on the CC-BY licence to reproduce those materials. Any copyright notices relating to those materials must be complied with.

Copyright and source acknowledgement notices may not be removed and must be displayed in any copy, derivative work or partial copy which includes the elements in question.

All copyright, and all rights therein, are protected by national and international copyright laws. The above represents a summary only. For further information please read Frontiers' Conditions for Website Use and Copyright Statement, and the applicable CC-BY licence.

ISSN 1535-3699

ISBN 978-2-8325-6694-7

DOI 10.3389/978-2-8325-6694-7

Generative AI statement

Any alternative text (Alt text) provided alongside figures in the articles in this ebook has been generated by Frontiers with the support of artificial intelligence and reasonable efforts have been made to ensure accuracy, including review by the authors wherever possible. If you identify any issues, please contact us.

Table of contents

Bioimaging

Original Research

- 07 **In-ovo imaging using ostrich eggs: biodistribution of F-18-FDG in ostrich embryos**
Thomas Winkens, Pauline Schweitzer, Olga Perkas, Christian Kühnel, Ferdinand Ndum, Marta Pomraenke, Julia Greiser and Martin Freesmeyer

Bionanoscience

Highlight

Original Research

- 22 **Correlation study of CAR, PLR, NLR with the prognosis of cardiogenic cerebral embolism patients**
Xiaojing Du, Xiaohui Li, Sheng Yue, Yuzhen Sun, Mengzhen Zhao, Lingshan Zhou, Xingwei Wang and Yapan Yang

Clinical Trials

Highlight

Original Research

- 32 **Dependence of mitochondrial dysfunction in peripheral blood mononuclear cells on cervicocephalic atherosclerotic burden in acute ischemic stroke**
Xiaoxi Zhao, Yi Yang, Xiangying Du, Luguang Li, Chengbei Hou, Yanning Cai and Xin Ma

Endocrinology and Nutrition

Original Research

- 43 **Selective association of plasma sphingolipid species with insulin sensitivity and secretion in normoglycemic Black and White American adults**
Peace Asuzu, Naser Aliye Feto, Jim Wan, Frankie Stentz, Nawajes Mandal and Samuel Dagogo-Jack

Genomics, Proteomics and Bioinformatics

Original Research

- 53 **An innovative full-size pathogenic tandem duplication mutation precise detection system based on next-generation sequencing**
Li-Li Zhang, Zhe Wang, Ying Zhou, Dai-Yang Li, Xiao-Nian Tu, Yu-Xia Li, Ke-Ming Du and Zhong-Zheng Zheng

Original Research**Immunology/Microbiology/Virology**

- 67 **Functional antibody responses to SARS-CoV-2 variants before and after booster vaccination among adults in Ghana**

F. D. Partey, A. N. A. Pobee, I. K. Damphey, F. Osei, M. M. A. K. Owusu-Amponsah, Y. A. A. Ansah, C. Ye, S. Bradfute, I. Hurwitz, P. K. Quashie, M. F. Ofori, A. K. Kusi, D. J. Perkins and G. A. Awandare

Brief Communication**Neuroscience**

- 79 **Impact of aging and body mass index on upper extremity motor unit number index and size**

Lauren I. Gulley Cox, Nicholas Dias, Chuan Zhang, Yingchun Zhang and Stacey L. Gorniak



OPEN ACCESS

*CORRESPONDENCE

Martin Freesmeyer,
✉ martin.freesmeyer@med.uni-jena.de

RECEIVED 02 March 2025

ACCEPTED 03 June 2025

PUBLISHED 19 June 2025

CITATION

Winkens T, Schweitzer P, Perkas O, Kühnel C, Ndum F, Pomraenke M, Greiser J and Freesmeyer M (2025) In-ovo imaging using ostrich eggs: biodistribution of F-18-FDG in ostrich embryos. *Exp. Biol. Med.* 250:10560. doi: 10.3389/ebm.2025.10560

COPYRIGHT

© 2025 Winkens, Schweitzer, Perkas, Kühnel, Ndum, Pomraenke, Greiser and Freesmeyer. This is an open-access article distributed under the terms of the [Creative Commons Attribution License \(CC BY\)](https://creativecommons.org/licenses/by/4.0/). The use, distribution or reproduction in other forums is permitted, provided the original author(s) and the copyright owner(s) are credited and that the original publication in this journal is cited, in accordance with accepted academic practice. No use, distribution or reproduction is permitted which does not comply with these terms.

In-ovo imaging using ostrich eggs: biodistribution of F-18-FDG in ostrich embryos

Thomas Winkens^{1,2}, Pauline Schweitzer¹, Olga Perkas¹, Christian Kühnel¹, Ferdinand Ndum¹, Marta Pomraenke^{1,2}, Julia Greiser^{1,2} and Martin Freesmeyer^{1,2*}

¹Clinic of Nuclear Medicine, Jena University Hospital, Jena, Germany, ²Working Group for Translational Nuclear Medicine and Radiopharmacy, Clinic of Nuclear Medicine, Jena University Hospital, Jena, Germany

Abstract

In-ovo imaging using ostrich eggs has been described as an alternative to animal testing using rodents. This approach is not considered an animal experiment and it does not require small-animal imaging devices as ostrich eggs provide good image quality on regular CT, MRI or PET used in humans. The aims of this study were 1) to describe methods of radiopharmaceutical injection, 2) to explore normal biodistribution of F-18-FDG during a 60-min list-mode-PET/CT examination and 3) to compare biodistribution in-ovo to existing literature considering chicken and rodents. Vessel access was successful in 54/78 ostrich eggs. Highest FDG-uptake was observed in epiphyseal plates (0.36 ± 0.06 IA%/g; range 0.29–0.48 IA%/g) and brain (0.25 ± 0.05 IA%/g; range 0.21–0.36 IA%/g). *In-vivo* activity distribution on PET and *ex-vivo* activity distribution (well counter) showed comparable results (Spearman's Rho range 0.795–0.882). No significant differences were observed regarding previous isoflurane exposure. Normal biodistribution of F-18-FDG in ostrich embryos using a standard PET/CT system for humans was mainly found as expected with highest uptake in epiphyseal plates and brain which is comparable to results on rodents and chicken embryos. Isoflurane anesthesia did not reveal significant differences regarding organ uptake. The results of this normal distribution study allow for interpretation of future disease models (inflammation, tumor) in ostrich embryos using F-18-FDG as radiopharmaceutical.

KEYWORDS

in-ovo imaging, ostrich eggs, animal model, glucose metabolism, preclinical imaging

Impact statement

This work shows that normal biodistribution of F-18-FDG in ostrich embryos is comparable to chicken embryos, rodents and humans. Thus, in-ovo-imaging using ostrich embryos represents a promising alternative to reduce animal research using rodents.

Introduction

Recently, preclinical imaging using ostrich eggs has been described as a potential alternative concept to common animal testing using rats or mice [1–4]. This approach bears the advantage that, according to national and international legislation, research using eggs does not qualify as animal testing as long as all experiments are carried out before hatching [5–8]. Thus, elaborate application for permission to conduct an animal experiment as well as adequate animal housing, trained personnel and specific equipment is – at least in part – expendable.

Usually, chicken embryos are used for in-ovo imaging; however, this requires dedicated small animal imaging devices which represents a disadvantage regarding limited access [1, 2, 4]. A concept using substantially larger ostrich eggs and imaging devices commonly used in routine clinical examinations in humans has been published before [1, 2, 4]. Important questions have been answered regarding implementation in a nuclear medicine research facility, physiological embryo development on serial CT-scans and immobilization using narcotic gases in order to minimize embryo movement during scans, e.g., list-mode PET/CT [1, 2, 4, 9, 10]. Given these preliminary studies regarding ostrich-based imaging, the next step requires systematic description of well-known radiopharmaceuticals in this novel preclinical imaging model which exceeds the information known from previous studies [4].

Thus, this study aims at describing methods of intravenous injection in ostrich embryos and investigating normal biodistribution of F-18-FDG in ostrich embryos using a standard PET/CT system on development day (DD) 37. Data obtained from dynamic list-mode examinations over 60 min are quantified and interpreted regarding image quality and compared to data obtained from studies investigating rodents and chicken eggs. Additionally, effect of isoflurane narcotic gas on F-18-FDG distribution is assessed. The understanding of normal biodistribution of F-18-FDG is necessary in order to develop disease models (e.g., inflammation or tumor models).

Materials and methods

Ostrich eggs

Ostrich eggs were obtained from a local ostrich farm 15 km from the research facility between April and September. Artificial incubation was carried out using a multistage egg incubator (Sofie 3, Hemel, Verl, Germany) with constant incubation properties at 36.5°C and 25% air humidity as described elsewhere [2, 4]. If artificially incubated, ostrich eggs usually hatch after 42 days [11]. As it was a requirement to end all experiments before hatching, studies were performed on DD 37.

This embryo study did not qualify as an animal research study according to the Federal German Animal Protection Act. Registration took place with the Office for Consumer Protection of the Thuringia State, registration number 22-2684-04-02-114/16. All experiments were carried out in compliance with German and international animal welfare legislation.

Immobilization

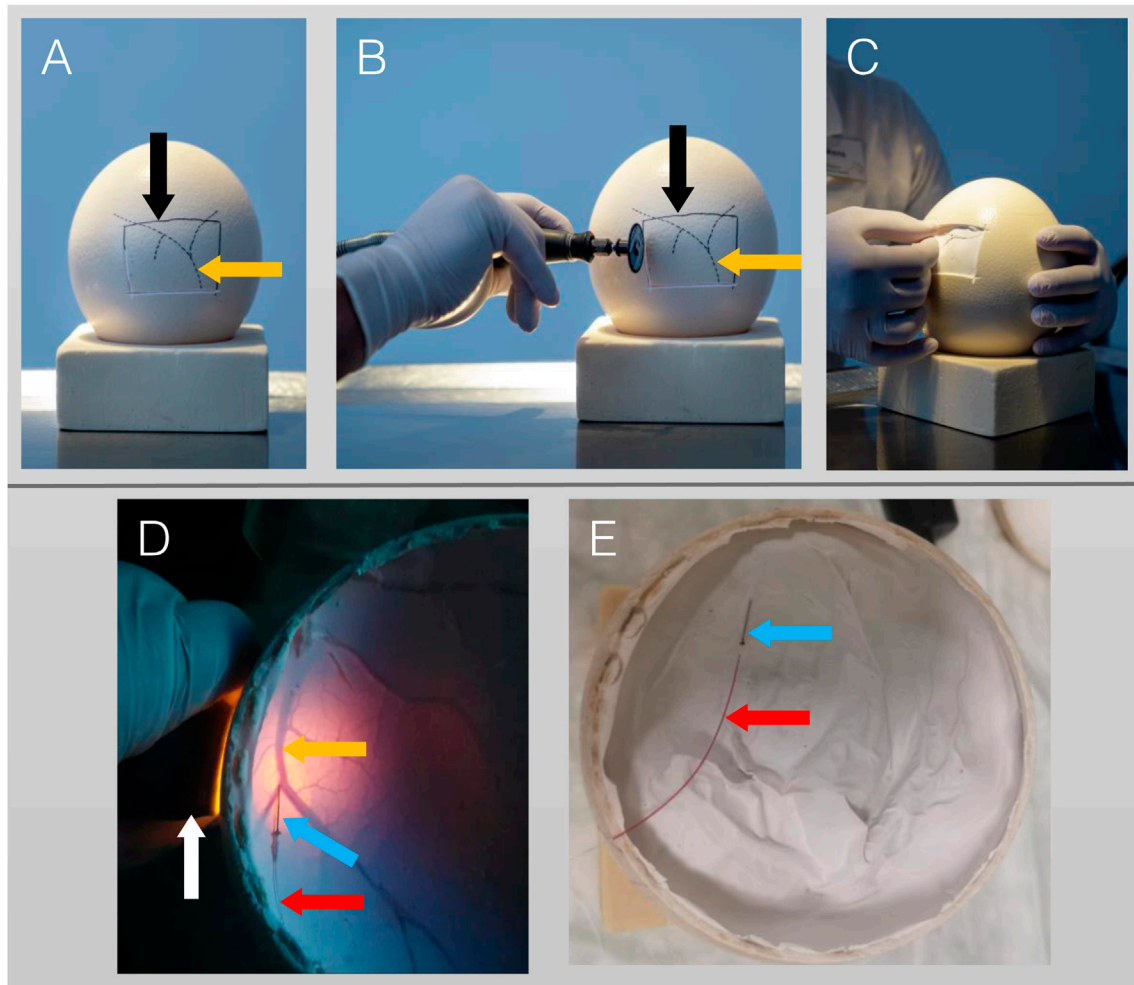
In order to prevent motion artifacts during 60-min list mode dynamic PET/CT scan, a part of the ostrich embryos were exposed to narcotic gas isoflurane (Piramal Healthcare, Mumbai, India) using a standard vaporizer (Vapor 2000 Isofluran, Draeger, Luebeck, Germany) and a fix concentration of 6% which has been described effective for immobilizing ostrich embryos [1, 9]. For 60 min, isoflurane exposure was performed in a gas-tight container prior to PET/CT scan. Ostrich eggs were subsequently transferred to a working bench, preparing for vessel access.

Vessel access

Intravenous application of radiopharmaceuticals requires establishing a vessel access. Candling (diaphanoscopy-like illumination) of ostrich eggs was performed on DD 25 and DD 28, identifying faintly visible vessels of chorioallantois-membrane (CAM) located beneath the eggshell. Subsequently, the vessels' location and course is marked on the eggshell using a pen. During later development stages, identification of CAM vessels is obscured by extended shadowing of the large ostrich embryo. On DD 37, part of the eggshell was removed using a rotating cutter (Dremel, Bosch Powertools B.V., Breda, Niederlande), either by windowing (removing a rectangular part of the eggshell; Figures 1A–C) or by decapitation (removing the whole eggshell at the end of the egg containing the air cell; Figures 1D,E). Subsequently, CAM vessel was punctured using a 30 gauge cannula (Sterican, B. Braun, Melsungen, Germany) (Figures 1D,E), connected to a polyethylene tube with an inner diameter of 0.28 mm (BD Intramedic, Fisher Scientific GmbH, Schwerte, Germany), and flushed with saline.

Radiopharmaceutical

F-18-fluorodeoxyglucose (FDG) was obtained from Life Radiopharma f-con GmbH (Holzhausen an der Haide, Germany). 1-mL syringes were filled with approx. 2–10 MBq F-18-FDG and total volume of <0.5 mL. Pre-injection and post-injection syringe activity was measured using a standard dose

**FIGURE 1**

Procedure of vessel access on DD 37. **(A–C):** Lateral access. **(A):** Lateral view with vessels (orange arrow, dotted lines) which were identified on DD 25 by candling and marked with a pencil. The solid line (black arrow) represents a rectangular area of the eggshell to be removed. **(B):** Cutting of the eggshell using a rotating cutter along the solid line. **(C):** The rectangular area of the eggshell has been removed and cannulation of a small vessel is performed. **(D,E):** Top access/Decapitation. **(D):** After the whole eggshell at top of the egg (containing the air cell) has been removed, a candling light (white arrow) is placed laterally, illuminating the CAM-vessels (orange arrow) beneath the white egg shell membrane. Cannulation is performed using a 30 gauge cannula (blue arrow). **(E):** Successful vessel access indicated by blood backflow into the catheter (red arrow).

calibrator (Isomed 2010, Nuvia Instruments GmbH, Dresden, Germany).

PET/CT data acquisition and reconstruction; image analysis

After establishing a vessel access, PET/CT examination started using a standard scanner for clinical routine examinations in human patients (Biograph mCT 40, Siemens Healthineers, Erlangen, Germany). First, full-dose CT-scan (120 kV, 200 mAs, increment 0.3 mm, slice thickness 0.6 mm, filtered back projection) was acquired for attenuation correction

purposes and anatomic co-registration. List-mode dynamic PET was started immediately after injection of F-18-FDG and data were acquired for 60 min. PET data reconstruction was performed using iterative technique (4 iterations, 12 subsets, matrix 400, Gaussian filter, zoom factor 2 and optimized proprietary reconstruction mode True X (Siemens Healthineers) comprising point spread function and ordered subset expectation maximization (OSEM) algorithms. List-mode data were reconstructed in 120 30-s-timeframes as well as additional 10-s frames during the first 2 minutes. Image analysis and quantification was performed using proprietary software (syngo.via, version VB50BHF02, Siemens Healthineers). In order to quantify activity distribution,

spherical volume-of-interests (VOIs) were drawn and activity was expressed as standardized uptake value (SUV), kBq/mL as well as relative injected activity per mass (IA%/g). For each organ/compartment, two VOIs were drawn and the mean value of both measurements was used for further analysis. IA%/g was chosen for comparison of PET and *ex-vivo* biodistribution data because well counter measurements cannot be expressed as SUV. Regarding dynamic activity distribution correct VOI position was manually verified in each timeframe. Patlak plots were derived from dynamic PET data using a blood-derived input function.

Ex-vivo biodistribution

Quantification of activity distribution of different ostrich organs was verified by *ex-vivo* measurements. After PET/CT examination, ostrich embryos were sacrificed by i.v. injection of 500 mg sodium pentobarbital. Organs (i.e., brain, heart, liver, ventriculus, intestine, kidneys) and fluids (i.e., yolk, blood) were collected and specific activity was measured using a standard well counter (Isomed 2100, Nuvia Instruments).

Statistics

Data analysis and descriptive statistics were performed using Excel (Microsoft Excel 2016, Microsoft Corporation, Redmont, WA, United States). Values were expressed as mean and standard deviation was given, if applicable. Correlation was calculated using Spearman's Rho Correlation Test and p-values < 0.05 were considered significant. Bland-Altman-plots were analyzed in order to exclude bias.

Results

A total of 339 ostrich eggs were obtained from a local ostrich farm. 78/339 (23.0%) showed fully developed ostrich embryos on DD 37 and were prepared for PET/CT imaging. Success of vessel access and reasons for partial or complete failure are shown in Figure 2. In total, 54/339 ostrich embryos were available for dynamic PET/CT imaging (60-min list mode) with different radiopharmaceuticals. Regarding normal distribution of F-18-FDG, twelve ostrich embryos were investigated after exposure to isoflurane. Four different ostrich embryos served as control group and were not exposed to isoflurane before PET/CT examination.

Visual image analysis

Five different time points of dynamic list mode PET/CT are shown in Figure 3, representing activity distribution over time.

Additionally, images of different organs/structures are shown in Figure 4.

Quantification

Dynamic activity distribution over time is shown in Figures 5, 6 Organ activity assessed 55 min p.i. via F-18-FDG-PET/CT and *ex-vivo* activity showed comparable results (Figure 7). Analyses using Bland-Altman plots revealed all data within 1.96-times standard deviation without significant overestimation or underestimation (data not shown). Highest uptake was found in epiphyseal plates (0.36 ± 0.06 IA%/g; range 0.29–0.48 IA%/g).

Effect of isoflurane

Figure 8 shows organ activity in ostrich embryos after exposure to isoflurane (n = 12) and without exposure to narcotic gases (n = 4). No significant differences were observed.

Discussion

This study describes normal biodistribution patterns of F-18-FDG in ostrich embryos 5 days before hatching.

Strengths of in-ovo imaging using ostrich embryos

The idea to use ostrich embryos arose from two specific limitations at the research facility: First, the lack of a small-animal imaging device for biodistribution studies, and second, prolonged time until receiving permission for classic animal testing using rodents. These limitations were addressed by using ostrich embryos which are large enough to be investigated in regular imaging devices used in humans and which do not qualify as animal testing under a legal view. The use of avian eggs, specifically chicken eggs, is widely distributed; however, mostly focusing on well-vascularized CAM as a biomembrane, allowing for tumor cell growth and thus, monitoring anti-neoplastic substances. The embryo itself usually is not in the focus of CAM-experiments. This is an unrealized potential as the embryo offers interesting advantages over rodents: First, avian embryos only need warmth and oxygen for regular development. All other resources (nutrition, water) are inside the eggshell, thus, no feeding is required. Second, during the second half of breeding, all organs are fully developed and thus, the whole body may be investigated. In contrast, CAM only focuses on the properties of the implanted tumor or the CAM vessel reaction to

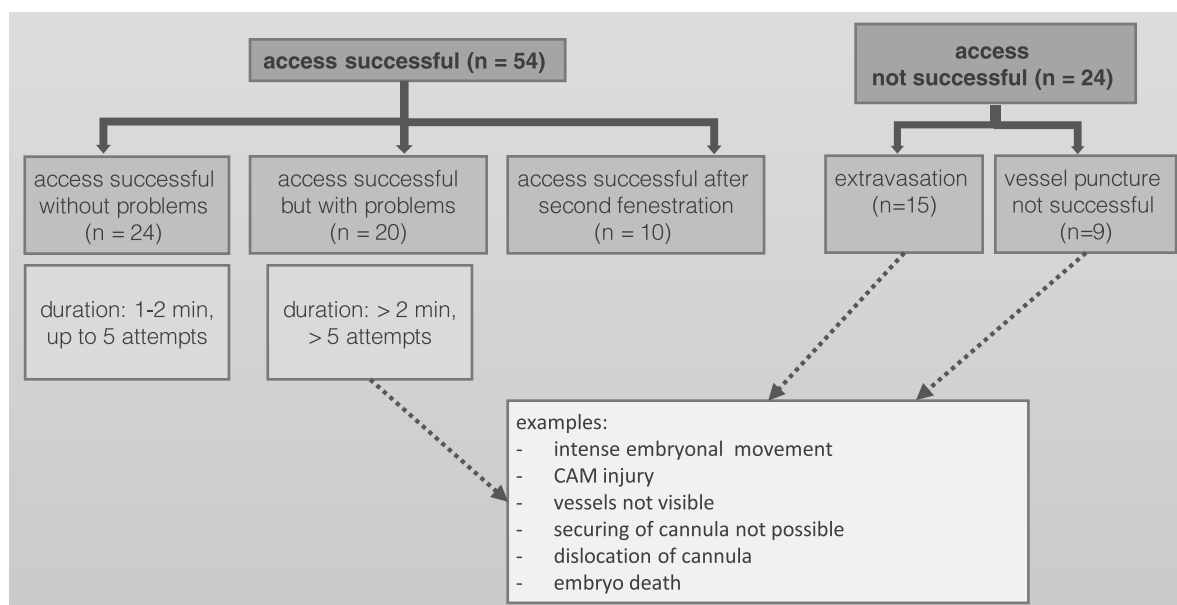


FIGURE 2
Success of vessel access and reasons for partial or complete failure.

the tumor. The limitations of using ostrich embryos are addressed below.

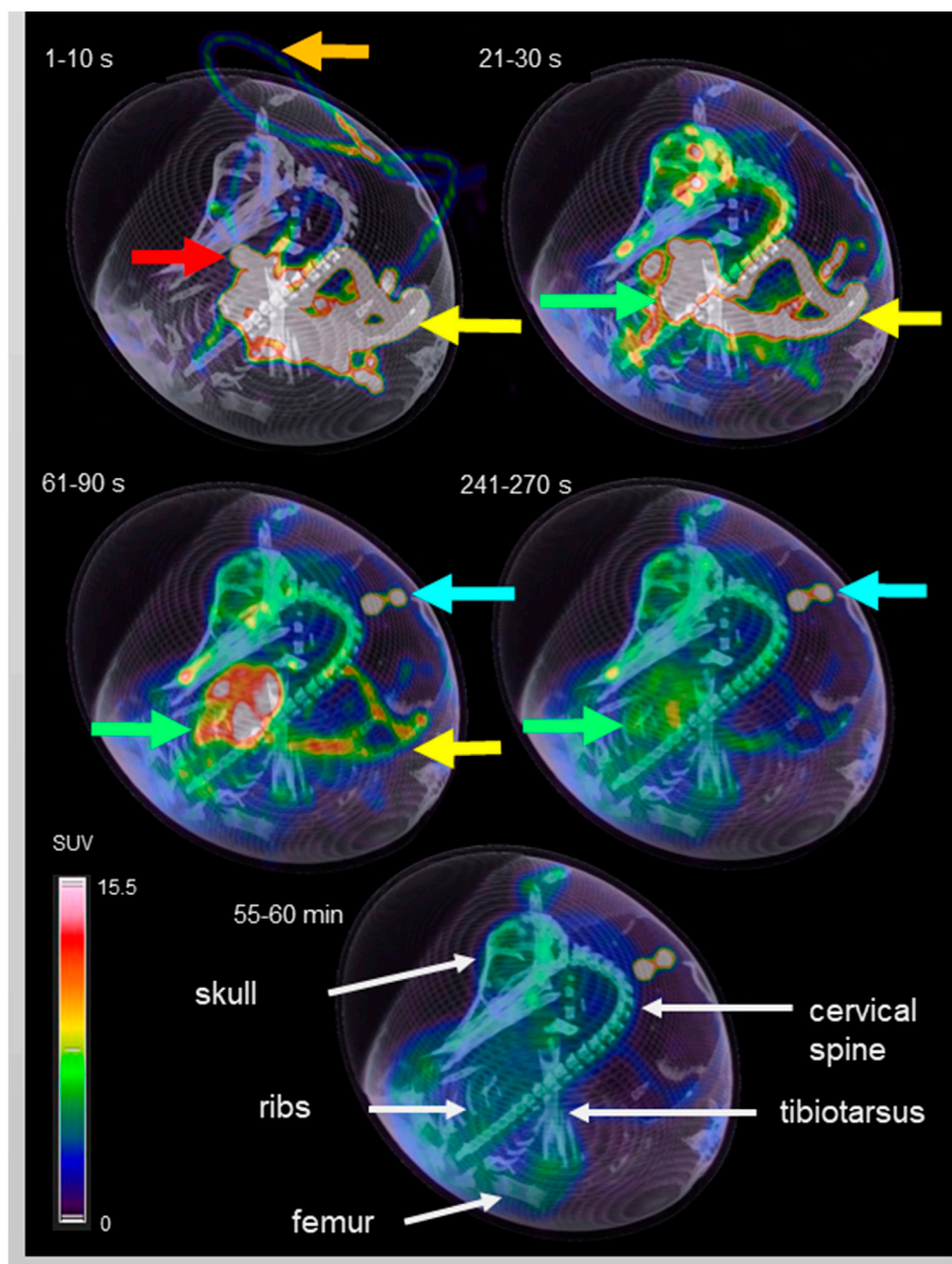
Artificial incubation and vessel access

Several steps are necessary in order to obtain a viable ostrich embryo on DD 37 for PET/CT imaging. First, eggs have to be fertilized which varies according to season, weather conditions and ostrich hens' and rooster's health [12–14]. Fertilized eggs are identified as early as DD 13 by candling and are continuously stored in the incubator while unfertilized eggs are removed and discharged [12, 14]. Second, during the following development steps, death-in-shell (DIS) can occur which also reduces the number of viable ostrich embryos [13]. Third, successful vessel access is required for i.v. injection of radiopharmaceuticals. After these steps, in the current study a total of 16% of initially obtained ostrich eggs contained viable embryos available for PET/CT imaging. Success rates for artificial breeding in ostrich farms vary from 40 to 70% which is higher than in this study [12, 15, 16]. This is attributable to distinct low rate of fertilization in our research facility in 2021 as previous years revealed fertilization in 29, 38 and 62% of ostrich eggs, respectively [14]. As it is difficult to improve fertilization rates *per se*, effectiveness of in-ovo imaging using ostrich eggs could be increased by improving methods of artificial breeding, thus avoiding DIS, and establishing vessel access, latter bearing higher potential with increasing handling experience [17, 18]. Also, ostrich egg supply needs to be considered. For this study, the ostrich eggs were

provided by one farm. A diversification of egg supply could add to improved artificial breeding success in years of low fertilization rates at one farm.

Visual image analysis

In-vivo biodistribution of F-18-FDG in ostrich embryos was found as expected. Image example of one ostrich embryo is shown in Figures 3, 4 with early tracer distribution in cardiovascular system, followed by liver accumulation and subsequent soft-tissue enhancement. At 55 min, epiphyseal plates and brain are the areas of highest tracer accumulation. Notably, soft-tissue clearance over time in ostrich embryos is less than biodistribution pattern described in rodents and humans. This is likely caused by lack of sufficient renal tracer excretion in ostrich embryos which rely on allantoic metabolite deposition instead of urinary excretion in adult animals and humans [19, 20]. Recently, comparable results have been described by Smith et al. for chicken embryos on DD 14 [18]. Earlier publications report on biodistribution of different radiopharmaceuticals, including FDG, in chicken embryos using a small-animal PET/CT system, also showing rather high soft-tissue accumulation of FDG [21]. Missing renal excretion of radiopharmaceuticals is known from patients with chronic kidney failure depending on dialysis. In most cases, the results of F-18-FDG-PET/CT are not significantly hampered and the clinical question is answered as accurately as in patients with normal renal function. Thus, high soft-tissue tracer accumulation

**FIGURE 3**

Dynamic PET/CT scan of an ostrich egg on DD 37. Fusion imaging of maximum intensity projection (MIP, PET) and virtual rendering technique (VRT, CT) was chosen for three-dimensional visualization. Timeframes in the upper left corner of each image represents the time after injection (p.i.) of 10 MBq F-18-FDG. In the first timeframe (1–10 s p.i.) the activity in the plastic tube is visible (orange arrow), caused by the injection. Additionally, the vitelline vein is depicted (yellow arrow) in which the blood flows from the CAM to the embryo. Due to high specific activity within a small volume, the embryo's vessels show an intense signal. Considering later time points, it is possible to identify an area of high uptake in the embryo's thorax during the first timeframe which decreases over time and represents the heart/blood activity (red arrow). The second image (21 – 30 s p.i.) shows accumulation of activity within the whole embryo, mainly in the vessels and starting in soft tissue. Activity in the vitelline vein (yellow arrow) is decreasing and the liver (green arrow) represents the organ with highest activity accumulation. The following two images (61 – 90 s p.i. and 241–270 s p.i.) are characterized by steady decrease of blood and liver activity, and increasing accumulation in soft tissue instead. In general, a more homogeneous activity distribution is observed compared to the early timeframes. The blue arrow marks activity which is located outside of the egg, caused by residual syringe activity placed next to the egg after application of F-18-FDG. The last image gives an overview of the activity distribution 55 – 60 min p.i. using the same thresholds for MIP-imaging. FDG-uptake is visible in the brain and in epiphyseal plates (see also Figure 4). White arrows mark anatomical structures for anatomic co-registration of activity distribution.

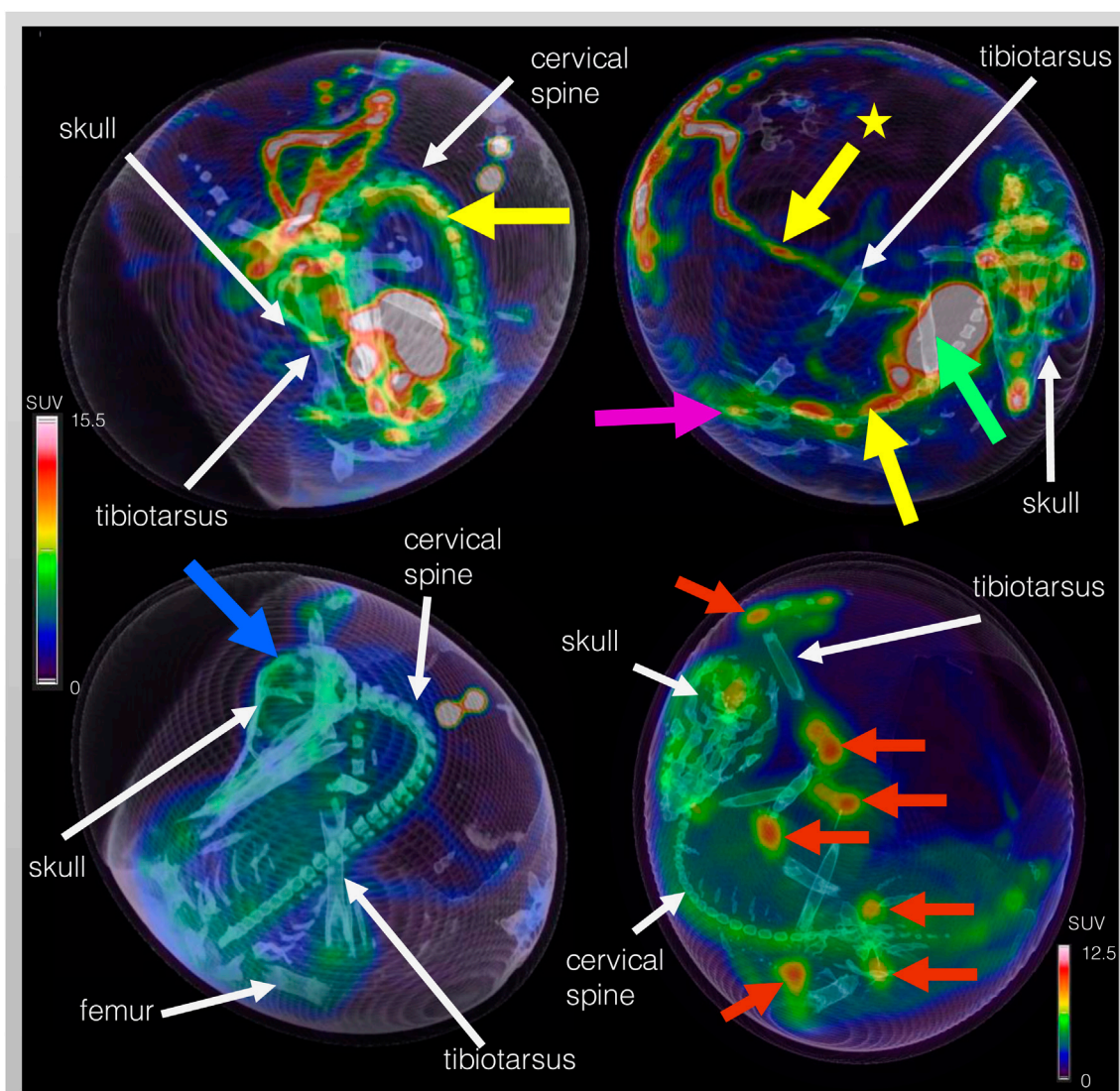


FIGURE 4

Dynamic F-18-FDG PET/CT scan of the same ostrich embryo as depicted in Figure 3 but with focus on representative images of organs and structures. Embryo vessels are shown in the two images of the top row at 31 – 40 s p.i. The yellow arrow marks the long carotid arteries (upper left image) and the abdominal aorta (upper right image) inferior to the liver (green arrow). The yellow arrow with star points at the extraembryonal vitelline vein. In the upper right image, activity within the kidneys is visible (pink arrow). Brain activity is marked with a blue arrow in the lower left image (40 min p.i.). In order to depict activity distribution in the epiphyseal plates (red arrows) of the lower extremity (femur, tibiotalus, tarsometatarsus), scaling was adjusted. White arrows mark anatomical structures for anatomic co-registration of activity distribution.

is not regarded as a significant limitation of in-ovo imaging using ostrich eggs.

Wu et al. described brain FDG uptake in mice over 60 min [22]. The results obtained in the current study suggest that brain uptake in ostrich embryos is less evident than reported for humans and awake mice. This might be attributable to three main factors: First, brain function in ostrich embryos is not yet fully developed before hatching, thus low glucose metabolism can be assumed. Gradually increasing cerebral glucose metabolism has been described for developing rats during pre- and postpartal period [23] which is supported by

analyses that the developing mammalian brain uses different substrates (e.g., ketones, fatty acids) and glucose, whereas the adult brain solely relies on glucose for energy supply [24]. Second, apart from cerebral base rate glucose metabolism, stimuli and sensations are low in a concealed egg shell, thus contributing to low brain activation. The brain of chicken embryos showed variable FDG-uptake in a study performed by Balaban et al. investigating different brain regions and describing active and inactive brain states [25]. Third, avian neurons have been described to consume three times less glucose than mammalian neurons; however, focusing on

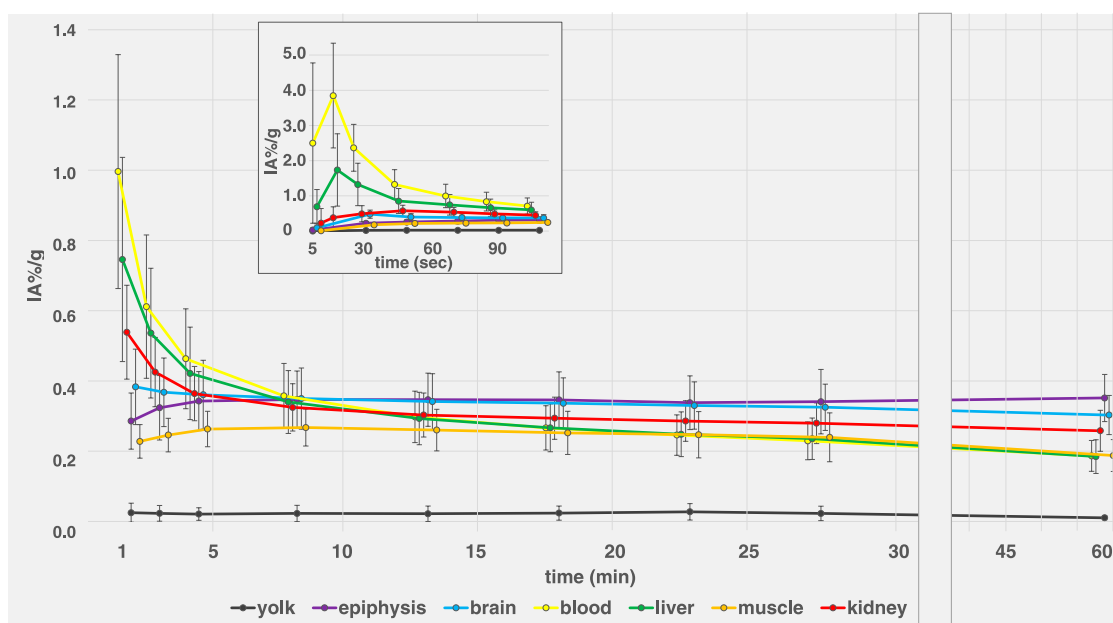


FIGURE 5

F-18-FDG biodistribution of 12 ostrich eggs in different organs and compartments (yolk, epiphyseal plates, brain, blood, liver, muscle, kidney) over 60 min, assessed via VOI measurements on PET/CT. X-axis was adjusted for late time points (>30 min) for better visualization. Insert graph on top shows first 120 s for assessment of early distribution effects, specifically blood curve (yellow). Data are expressed as relative organ activity per injected activity (IA%/g). Whiskers represent standard deviation. For clarity purposes, time points were spread in order to allow for delineation of data point whiskers. At 60 min p.i., epiphyseal plates (purple line) and brain (blue line) show highest uptake. Yolk shows consistently low FDG uptake over time.

adult organisms and thus being comparable only with limitations to embryos development stages [26].

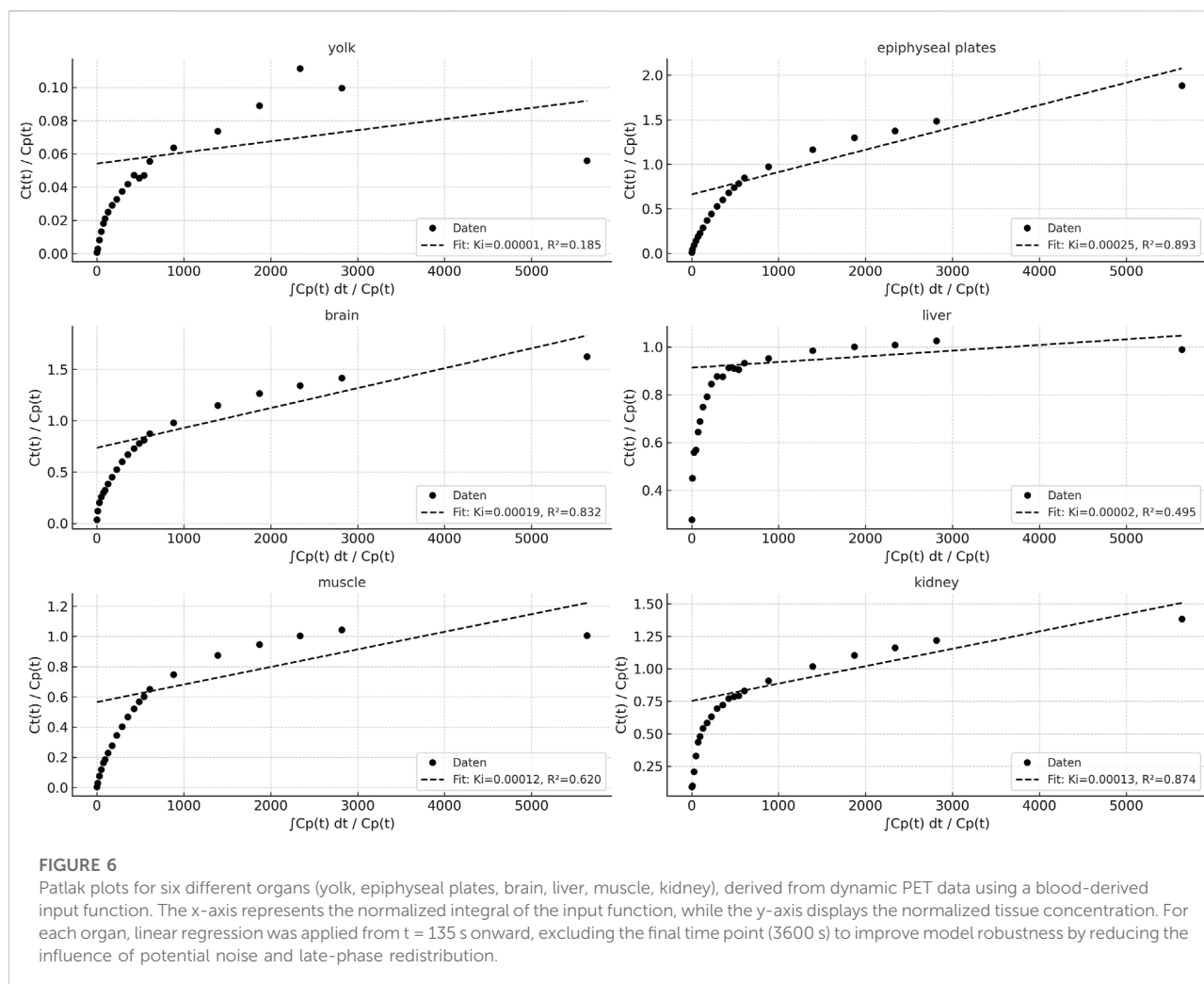
Our data show that glucose metabolism in the liver is lower than in brain, kidneys and epiphyseal plates. In humans, GLUT1 is the main glucose transporter in fetal liver, ensuring insulin-independent glucose uptake via placental circulation [27], suggesting high glucose uptake. After birth and following enteral feeding, GLUT1 is downregulated and GLUT2 expression gradually increases. Furthermore, gluconeogenesis and glycogenolysis mature, stabilizing blood glucose levels [27]. Metabolic analyses of post-hatch chicken show early presence of glycolysis and gluconeogenesis as well as reliance on amino acids and fatty acids which are stored in the yolk, resembling the processes that occur in mammals. After hatching, during a time period of 20 days, metabolism changes in order to effectively utilize fed nutrients [28] and – as in mammals – GLUT2 is also expressed [29]. FDG-PET/CT show similar distribution patterns in chicken embryos compared to the presented data [21]. Regarding ostriches, little is known about the embryonic hepatic glucose metabolism but data derived from chicks and adult ostriches show comparative blood glucose levels, increasing with the individual's age and development [30].

Tracer accumulation of FDG in epiphyseal plates is also known from examinations in children and indicates high glucose metabolism in sites of rapid bone growth with higher SUV-values

for younger age groups [31, 32]. This has also been described for in-ovo imaging using chicken embryos [21, 33].

Regarding PET/CT imaging in humans, recent technological developments feature large scanners with multiple ring detectors creating a long axial field of view (e.g., uEXPLORER, United Imaging Healthcare; Biograph Vision Quadra, Siemens Healthineers). Liu et al. investigated normal biodistribution of FDG in healthy volunteers using scanners of this type [34]. One evident difference between humans and ostrich embryos is predominant tracer distribution within lung tissue during the first 5 minutes, representing physiological blood flow in pulmonary vascular system. Due to embryonic circulation bypassing pulmonary vessels, lung tissue was not identified on FDG-PET studies in ostrich embryos.

Notably, no individual showed myocardium uptake. Human myocardium is known for variable inter- and intraindividual FDG uptake, depending on the main source of energy supply at the moment of FDG administration. As both fatty acids and glucose are suitable as energy substrates for myocardium, both metabolic states can be found in patients [35]. Insulin increases cardiac FDG-uptake in mice [36] and humans [37]. Bencurova et al. reported on biodistribution of FDG in chick embryos on DD 16-18 describing little FDG uptake within the heart, however, without exactly stating whether myocardium uptake or blood-pool-activity was regarded as the source of tracer accumulation



[33]. However, Souza et al. described variable cardiac FDG uptake related to myocardium in a small study investigating adult parrots, indicating variability in avian species [38]. Up to date, there are no comparable cardiac imaging studies using FDG-PET/CT in chicken or ostriches but Kutchai et al. described *ex-vivo* experiments assessing high glucose uptake in chick embryos during early development with decreasing uptake over time [39]. –This is supported by autoradiography experiments by Kostreva who investigated C-14-deoxyglucose chicken heart and stating high glucose dependence of embryonic myocardium of different species [40] More invasive experiments as conducted currently could contribute to the understanding of ostrich embryo myocardium uptake, i.e., co-injection of insulin or glucose.

Quantification

Visual description of FDG biodistribution is supported by quantification using VOI-measurements in PET over time

(Figures 5, 6) as well as *ex-vivo* measurements after organ collection and activity measurement using a well-counter (Figure 7).

Tissue activity curves using the Patlak model provide an approximation for tracer kinetics of various tissues and compartments. High linearity was observed in brain and epiphyseal plates ($R^2 > 0.98$), indicating strong irreversible tracer uptake and model conformity. The influx rate constant K_i reflects organ-specific tracer accumulation rates, with the kidney and liver showing higher K_i values, consistent with their metabolic/excretory roles. The yolk and muscle curves exhibited flatter slopes and lower R^2 values, suggesting limited tracer trapping or predominantly reversible kinetics in these tissues.

Organ time activity curves in humans show comparable values to data obtained in ostrich embryos in this study [41–43]. Two different ways are generally used for describing radiopharmaceutical uptake in PET studies: IA%/g and SUV. While IA%/g is independent from body weight and total volume,

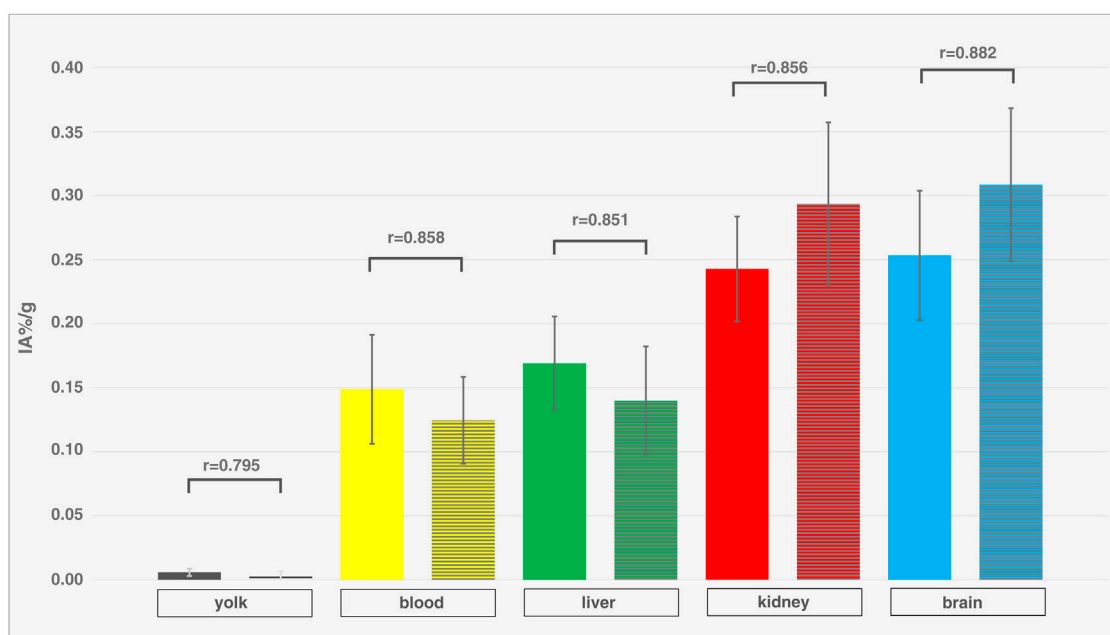


FIGURE 7

Comparison of *in-vivo* and *ex-vivo* measurements. Organ activity of different compartments and organs (yolk, blood, liver, kidney, brain) of different ostrich embryos (isoflurane, $n = 12$), assessed via VOI measurements on PET/CT (left columns, without texture) 55 min p.i. and *ex-vivo* measurements (right columns, with texture). Whiskers represent standard deviation. Data are expressed as relative organ activity per injected activity (IA%/g). R-values were calculated using Spearman's Rho and p-values are < 0.0001 for all compartments and organs. As all R-values are > 0.8 , a very strong correlation is present between PET and *ex-vivo* measurements indicating sufficient reliability of PET quantification.

SUV uses body weight as a factor which allows for comparison of species with different weight. Both methods bear advantages and disadvantages that have to be considered when comparing FDG uptake within different species. In this study, IA%/g was used for data description as it is suitable for both PET and *ex-vivo* well counter measurements, allowing direct comparison of both. Most preclinical studies focus on IA%/g and ID%/g (relative injected dose per mass), respectively [44, 45], and use these parameters for imaging and *ex-vivo* well counter measurements as well. SUV is a parameter commonly used in clinical routine to assess radiopharmaceutical uptake in patients. It offers a sufficiently robust, yet straightforward and reproducible method for quantifying tracer accumulation, for example, in tumor lesions [46, 47].

Rodent and in-ovo PET-imaging have been described to show similar uptake of reference regions using PSMA-ligands [48]. In order to contextualize the FDG-uptake values derived from ostrich embryos and described in this study, Table 1 gives an overview of data published on different species and FDG normal distribution (Table 1). This data also supports visual quantification in terms of soft tissue clearance: In ostrich embryos, levels of F-18-FDG accumulation are similar for liver and muscle tissue, whereas lower glucose metabolism is described for rodent muscle tissue than for rodent liver tissue.

Table 1 also indicates the need for careful interpretation of activity quantification when species are compared because both SUV and IA%/g show substantial differences (Table 1).

As quantification relies on successful intravenous application of radiopharmaceuticals, special attention has to be paid to paravasation which particularly influences PET quantification in dynamic studies [17, 18, 70].

Effect of isoflurane

This study also assessed the effect of isoflurane on various organs and compartments. No significant differences were found for yolk, blood, muscle, liver, kidney, brain and epiphyseal plates. This result was unexpected as isoflurane usually reduces brain glucose metabolism and thus, FDG uptake, which has been reported for mice and other mammals [71] and is also known for PET examinations in humans after sedation [72]. Also, changes in FDG-metabolism of other organs, e.g., liver, kidneys and muscles have been reported after application of isoflurane [54]. Thus, the effect of isoflurane on glucose metabolism of ostrich embryos as well as other anesthetic or muscle relaxing agents needs to be further investigated. The immobilization effect of isoflurane anesthesia on ostrich embryos

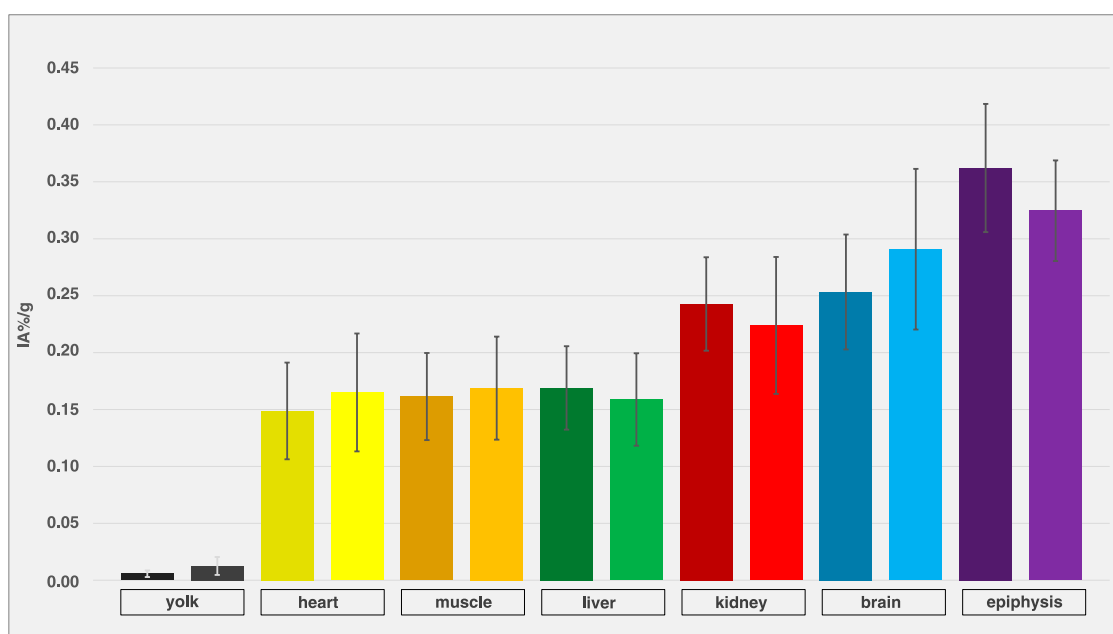


FIGURE 8

Comparison of embryos with and without isoflurane exposure. Organ activity of different compartments and organs of different ostrich embryos after exposure to isoflurane (left columns, dark-colored, $n = 12$) and without exposure to narcotic gases (right columns, light-colored, $n = 4$), assessed via VOI measurements on PET/CT 55 min p.i. Whiskers represent standard deviation. Data are expressed as relative organ activity per injected activity (IA%/g). Using Shapiro-Wilk test and Kruskal-Wallis test, no significant differences were observed.

was not in the scope of this study and has been described elsewhere [9, 14].

Limitations

This study has limitations that need to be considered when interpreting the results. First, the number of ostrich embryos is rather small ($n = 16$) and thus, quantification results are not as reliable, limiting the statistical power of this study. The confidence intervals of biodistribution data (Figures 5, 7) and comparison with a control group (Figure 8) show high variation which could be improved by including more individuals per group. Efforts have to be made in order to increase artificial breeding success by early dismissal of non-fertilized and bacterially infected eggs as well as increasing the number of eggs ordered from the farm. Second, dynamic data was evaluated only using VOI-measurement technique in PET. Invasive arterial input functions were not considered as it has not been established to draw arterial blood in-ovo. Third, regarding reliability of PET-based quantification, signal-to-noise ratio (SNR) was not quantitatively assessed. The spatial resolution of the clinical PET/CT scanner (Biograph mCT 40; FWHM 4.4 mm) used in this study is inherently limited compared to small-animal systems (e.g., Siemens Inveon PET; FWHM

1.2 mm), potentially introducing partial volume effects, especially in small embryonal structures. This may have impacted quantification accuracy in organs difficult to delineate (e.g., kidney). In order to verify correct PET quantification, VOI data were compared to *ex-vivo* measurements, producing concordant results (Figure 7). This leads to the conclusion that PET quantification is sufficiently correct.

Fourth, direct comparison of ostrich embryo and similar-sized established animal models using the same scanner was not performed. This setup would allow for even more detailed comparison of both imaging models. Fourth, although there are numerous ostrich farms in Germany [12], ostriches lay eggs only from April to September, which limits the availability to these seasons. This represents a disadvantage compared to chicken eggs which offer year-round access and has to be considered in experiment planning. The use of eggs of other ratites (e.g., emu, *dromaius novohollandiae*) might possibly overcome this availability gap as they are available from December to March [12, 58].

Future direction and outlook

Despite the aforementioned limitations of this study and the concept of in-ovo imaging using ostrich eggs, this approach has

TABLE 1 Overview of FDG uptake in different organs and different species.

Animal model	body weight	Brain				Liver				Muscle			
		organ weight (g)	SUV	IA%/g	reference	organ weight (g)	SUV	IA%/g	reference	organ weight (g)	SUV	IA%/g	reference
Chicken embryo (in-ovo)	60 g (egg) 20 g (embryo) on DD 18	0.89 g	-	4–8	[18, 21, 33, 49]	0.6 g	-	4–8	[21, 50]	-	-	2.5	[21]
Mouse	20–25 g	0.5 g	1.2	4–10	[41, 51–53]	1.5–3 g	0.5	1.0–4.1	[54–56]	-	1.5	0.6–2.2	[54–56]
Rat	170 – 290 g	1.7–2.0 g	1.4–1.8	0.4	[43, 57, 58]	12–19 g	0.6–1.0	0.31 +/- 0.16	[59, 60]	-	0.3	0.08 +/- 0.02	[61]
Ostrich embryo (in-ovo)	1,200 g (egg) 500 g (embryo) on DD 37	3.7 +/- 0.4	4.3 +/- 1.3	0.29+/- – 0.07	This study	6.1 +/- 1.1 g	2.8 +/- 0.5	0.20 +/- 0.04	This study	-	2.4 +/- 0.4	0.2 +/- 0.04	This study
Rabbit	2.5–5 kg	9 g	1.8	0.01	[62, 63]	80 g	2.5	-	[62, 63]		0.2	-	[62, 63]
Miniature Pig	10–20 kg	100 g	1.1–3.1	0.03	[64, 65]	320 g	1.15	-	[64, 65]		0.3	-	[65]
Human	75 kg	1400 g	5–15	0.001–0.005	[41, 66]	1,500 g	2.0–2.4	-	[67, 68]		0.4–1.4	-	[69]

Abbreviations: DD, development day; SUV, standardized uptake value; IA–injected activity.

the potential to be integrated into the landscape of preclinical research, specifically imaging studies. Of course, the results presented in this article need further investigation and verification (e.g., blocking studies evaluating tracer uptake specificity, sophisticated quantification using invasive arterial input functions) as well as expanding the field of application to other tracers. In order to be used in research projects, the normal biodistribution described in this study is not sufficient; thus, the development of disease models (e.g., tumor models, inflammation models) is crucial. This allows for interventional studies, testing new radiopharmaceuticals (aimed at tumor or inflammation) or anti-tumor (anti-inflammation) treatment agents and visualizing the therapeutic effect by preclinical imaging, i.e., F-18-FDG-PET/CT. In rodents, subcutaneous injection of substances is well established and could be transferred to ostrich embryos as well. These substances comprise tumor cells (either tumor cell lines or patient-derived tumor cells or organoids), inflammation agents (Carrageen, bacteria), and more. Establishing tumor and inflammations models in ostrich embryos requires several steps: First, it is necessary to determine the best way to inject a substance (i.e., tumor cells, inflammation agents) into the embryo without harming vital structures, requiring visual guidance (either via ultrasound or CT) and identification of optimal injection site (i.e., subcutaneous, intraperitoneal, yolk sac). Second, selection of optimal parameters (concentration, incubation time) is crucial to grow tumors and induce inflammation, respectively. Third, experiments are necessary to prove adequate therapy response, e.g., the size of a tumor in response to an established chemotherapy protocol with a control group without antineoplastic treatment. Regarding inflammation, response of a local infection to an established antibiotic regimen should be part of experiment planning. Fourth, appropriate PET radiopharmaceuticals need to be selected for tumor imaging (FDG or Ga-68-FAPI (fibroblast activating protein inhibitor) targeting cancer associated fibroblasts) and inflammation imaging (FDG or Ga-68-Pentixafor targeting chemokine signals (CXCL12/CXCR4 pathway), respectively. This allows for assessing the therapeutic effect via PET imaging.

In addition to utilizing the embryo as an experimental model, CAM assays using chicken eggs is an established alternative for animal testing, growing tumors and inducing inflammation on this highly-vascularized biomembrane [18–20]. Transferring this knowledge from chicken CAM to ostrich CAM has already been reported [10]. Summarizing, once disease models have been developed, preclinical imaging using ostrich embryos might represent a contribution to 3-R-principles reducing the required number of fully developed animals.

Conclusions

This study describes PET imaging using ostrich embryos, representing an alternative imaging model for preclinical imaging. Normal biodistribution of F-18-FDG in ostrich embryos using a standard PET/CT system for humans was mainly found as expected with highest uptake in brain and epiphyseal plates which is comparable to results on rodents and chicken embryos. Isoflurane anesthesia was applied to part of the individuals in order to reduce motion artifacts and revealed no significant differences regarding organ uptake. The results of this normal distribution study allow for interpretation of future disease models (e.g., inflammation, tumor) in ostrich embryos using FDG as radiopharmaceutical.

Author contributions

TW conceived of the study, wrote the manuscript and provided funding. PS and OP performed experiments and conducted data reconstruction/evaluation. CK and JG provided thorough technical support. FN and MP performed experiments. MF conceived of the study and provided funding. All authors contributed to the article and approved the submitted version.

Data availability

The raw data supporting the conclusions of this article will be made available by the authors, without undue reservation.

Ethics statement

Ethical approval was not required for the study involving humans in accordance with the local legislation and institutional requirements. Written informed consent to participate in this study was not required from the participants or the participants' legal guardians/next of kin in accordance with the national legislation and the institutional requirements. The requirement of ethical approval was waived by Office for Consumer Protection of the Thuringia State, registration number 22-2684-04-02-114/16 for the studies involving animals because this study did not qualify as animal research study. The studies were conducted in accordance with the local legislation and institutional requirements.

Funding

The author(s) declare that financial support was received for the research and/or publication of this article. This work was

funded by German Research Society (Deutsche Forschungsgemeinschaft) GZ FR 2724/2-1 and GZ WI 5346/2-1.

Acknowledgments

Anna Christl, Hanna Hermeyer, Wiebke Neuschulz, Gregor Anslinger, Michelle Wallrodt and Veronika Porwoll are acknowledged for assistance in data analysis. PD Dr. Thomas Bartels and Dr. Sabine Bischoff are acknowledged for veterinary support.

References

- Freemeyer M, Hermeyer H, Kuehnelt C, Perkas O, Greiser J, Witte OW, et al. In-ovo imaging using ostrich eggs: biomagnetism for detection of cardiac signals and embryonal motion. *Exp Biol Med (Maywood)* (2022) **247**:996–1004. doi:10.1177/15353702221082046
- Winkens T, Christl A, Kuehnelt C, Ndum F, Seifert P, Greiser J, et al. In-ovo imaging using ostrich eggs-Evaluation of physiological embryonal development on computed tomography. *Acta Zoologica* (2021) **103**:492–502. doi:10.1111/azo.12400
- Winkens T, Kuehnelt C, Freemeyer M. In-ovo imaging using ostrich eggs - replacement of animal studies? *J Nucl Med* (2020) **61**:1122.
- Freemeyer M, Kuehnelt C, Opfermann T, Niksch T, Wiegand S, Stolz R, et al. The use of ostrich eggs for in ovo research: making preclinical imaging research affordable and available. *J Nucl Med* (2018) **59**:1901–6. doi:10.2967/jnumed.118.210310
- Leary S, Anthony R, Cartner S, Grandin T, Greenacre C, Gwaltney-Brant S, et al. *AVMA guidelines for the euthanasia of animals*. 2020 Edition. Schaumburg, IL, USA: American Veterinary Medical Association (2020).
- Epu R. Richtlinie 2010/63/EU zum Schutz der für wissenschaftliche Zwecke verwendeten Tiere. Brüssel. In: *Europäisches Parlament und Rat* (2010).
- BdJuf V. Tierschutzgesetz. In: *Verbraucherschutz* BJ, editor. Bundesministerium der Justiz und für Verbraucherschutz (2016).
- Agriculture USDo. Animal welfare act and animal welfare regulations. (2013).
- Perkas O, Schmidt A, Kuehnelt C, Greiser J, Hermeyer H, Klingner C, et al. Different narcotic gases and concentrations for immobilization of ostrich embryos for in-ovo imaging. *Exp Biol Med (Maywood)* (2024) **249**:10037. doi:10.3389/ebm.2024.10037
- Pomraenke M, Bolney R, Winkens T, Perkas O, Pretzel D, Theis B, et al. A novel breast cancer xenograft model using the ostrich chorioallantoic membrane-A proof of concept. *Vet Sci* (2023) **10**:349. doi:10.3390/vetsci10050349
- Gefen E, Ar A. Morphological description of the developing ostrich embryo: a tool for embryonic age estimation. *Isr J Zool* (2001) **47**:87–97. doi:10.1092/H218-1h2u-81h1-P5xy
- Nussstein C. *Untersuchung der Haltungsbedingungen von Nandus (Rhea americana), Emus (Dromaius novaehollandiae) und Straußen (Struthio camelus) in Süddeutschland*. München: Ludwig-Maximilians-Universität München (2009).
- Brand Z. *Studies on embryonic development and hatchability of ostrich eggs*. Matieland, South Africa: University of Stellenbosch (2012).
- Winkens T. *In-ovo Bildgebung an Straußeneiern – Evaluierung einer Alternative zum klassischen Tierversuch [Habilitation]*. Jena: Friedrich-Schiller Universität (2022).
- Nahm KH. Effects of storage length and weight loss during incubation on the hatchability of ostrich eggs (*Struthio camelus*). *Poult Sci* (2001) **80**:1667–70. doi:10.1093/ps/80.12.1667
- Deeming DC. Factors affecting hatchability during commercial incubation of ostrich (*Struthio camelus*) eggs. *Br Poult Sci* (1995) **36**:51–65. doi:10.1080/00071669508417752
- Kuntner C, Stout D. Quantitative preclinical PET imaging: opportunities and challenges. *Front Phys* (2014) **2**. doi:10.3389/fphy.2014.00012

Conflict of interest

The author(s) declared no potential conflicts of interest with respect to the research, authorship, and/or publication of this article.

Generative AI statement

The author(s) declare that no Generative AI was used in the creation of this manuscript.

- Smith LM, Greenwood HE, Tyrrell WE, Edwards RS, de Santis V, Baark F, et al. The chicken chorioallantoic membrane as a low-cost, high-throughput model for cancer imaging. *npj Imaging* (2023) **1**:1. doi:10.1038/s44303-023-00001-3
- Merckx G, Tay H, Lo Monaco M, van Zandvoort M, De Spiegelaere W, Lambrichts I, et al. Chorioallantoic membrane assay as model for angiogenesis in tissue engineering: focus on stem cells. *Tissue Eng B: Rev* (2020) **26**:519–39. doi:10.1089/ten.teb.2020.0048
- Chen L, Wang S, Feng Y, Zhang J, Du Y, Zhang J, et al. Utilisation of chick embryo chorioallantoic membrane as a model platform for imaging-navigated biomedical research. *Cells* (2021) **10**:463. doi:10.3390/cells10020463
- Gebhardt P, Würbach L, Heidrich A, Heinrich L, Walther M, Opfermann T, et al. Dynamic behaviour of selected PET tracers in embryonated chicken eggs. *Revista española de medicina Nucl e imagen Mol* (2013) **32**:371–7. doi:10.1016/j.rem.2013.07.002
- Wu HM, Sui G, Lee CC, Prins ML, Ladno W, Lin HD, et al. In vivo quantitation of glucose metabolism in mice using small-animal PET and a microfluidic device. *J Nucl Med* (2007) **48**:837–45. doi:10.2967/jnumed.106.038182
- Lewis D, Koba W, Fine E, Amor-Coarasa A. The anomalous metabolism of the developing brain: rat experiments. *J Nucl Med* (2021) **62**:1626.
- McKenna MC, Scafidi S, Robertson CL. Metabolic alterations in developing brain after injury: knowns and unknowns. *Neurochem Res* (2015) **40**:2527–43. doi:10.1007/s11064-015-1600-7
- Balaban E, Desco M, Vaquero JJ. Waking-like brain function in embryos. *Curr Biol* (2012) **22**:852–61. doi:10.1016/j.cub.2012.03.030
- von Eugen K, Endepols H, Drzezga A, Neumaier B, Güntürkün O, Backes H, et al. Avian neurons consume three times less glucose than mammalian neurons. *Curr Biol* (2022) **32**:4306–13.e4. doi:10.1016/j.cub.2022.07.070
- Minamoto R, Abe Y, Kamiya S, Nakane T, Ito R, Kato K, et al. Imaging insights of FDG-PET from neonates to infants. *Japanese J Radiol* (2025). doi:10.1007/s11604-025-01763-z
- Van Every H, Schmidt CJ. Metabolic and morphometric analysis of allometric and total liver growth in Post-Hatch chickens. *Metabolomics* (2025) **21**:52. doi:10.1007/s11306-025-02250-2
- Du P, Wang H, Shi X, Zhang X, Zhu Y, Chen W, et al. A comparative study to determine the effects of breed and feed restriction on glucose metabolism of chickens. *Anim Nutr* (2023) **13**:261–9. doi:10.1016/j.aninu.2023.02.005
- Durgun Z, Keskin E, Çöl R, Atalay B. Selected haematological and biochemical values in ostrich chicks and growers. *Arch Geflügelkd* (2005) **69**:62–6. doi:10.1016/S0003-9098(25)00576-4
- Otani T, Nakamoto Y, Ishimori T. Physiological FDG uptake in growth plate on pediatric PET. *Asia Ocean J Nucl Med Biol* (2021) **9**:15–20. doi:10.22038/aojnm.2020.49638.1339
- Shammas A, Lim R, Charron M. Pediatric FDG PET/CT: physiologic uptake, normal variants, and benign conditions. *Radiographics* (2009) **29**:1467–86. doi:10.1148/rg.295085247
- Benčurová K, Friske J, Anderla M, Mayrhofer M, Wanek T, Nics L, et al. CAM-xenograft model provides preclinical evidence for the applicability of [68Ga] Ga-pentixofor in CRC imaging. *Cancers* (2022) **14**:5549. doi:10.3390/cancers14225549
- Liu G, Xu H, Hu P, Tan H, Zhang Y, Yu H, et al. Kinetic metrics of 18F-FDG in normal human organs identified by systematic dynamic total-body positron

- emission tomography. *Eur J Nucl Med Mol Imaging* (2021) **48**:2363–72. doi:10.1007/s00259-020-05124-y
35. Boellaard R, Delgado-Bolton R, Oyen WJG, Giammarile F, Tatsch K, Eschner W, et al. FDG PET/CT: EANM procedure guidelines for tumour imaging: version 2.0. *Eur J Nucl Med Mol Imaging* (2015) **42**:328–54. doi:10.1007/s00259-014-2961-x
36. Zhao J, Tan C, Imai N, Ukon N, Shimoyama S, Maejima Y, et al. Evaluation of organ glucose metabolism by 18F-FDG accumulation with insulin loading in aged mice compared with young normal mice. *Scientific Rep* (2021) **11**:7421. doi:10.1038/s41598-021-86825-8
37. Gupta K, Jadhav R, Prasad R, Virmani S. Cardiac uptake patterns in routine 18F-FDG PET-CT scans: a pictorial review. *J Nucl Cardiol* (2020) **27**:1296–305. doi:10.1007/s12350-020-02049-9
38. Souza MJ, Wall JS, Stuckey A, Daniel GB. Static and dynamic 18fdg-pet in normal hispaniolan amazon parrots (Amazona ventralis). *Vet Radiol & Ultrasound* (2011) **52**:340–4. doi:10.1111/j.1740-8261.2010.01793.x
39. Kutchai H, King SL, Martin M, Daves ED. Glucose uptake by chicken embryo hearts at various stages of development. *Developmental Biol* (1977) **55**:92–102. doi:10.1016/0012-1606(77)90322-0
40. Diamond A. Developmental time course in human infants and infant monkeys, and the neural bases of, inhibitory control in reaching. *Ann N Y Acad Sci* (1990) **608**:637–69. doi:10.1111/j.1749-6632.1990.tb48913.x
41. Sari H, Mingels C, Alberts I, Hu J, Buesser D, Shah V, et al. First results on kinetic modelling and parametric imaging of dynamic 18F-FDG datasets from a long axial FOV PET scanner in oncological patients. *Eur J Nucl Med Mol Imaging* (2022) **49**:1997–2009. doi:10.1007/s00259-021-05623-6
42. Amirraheshi M, Zaidi H, Ay MR. Towards quantitative small-animal imaging on hybrid PET/CT and PET/MRI systems. *Clin Translational Imaging* (2020) **8**:243–63. doi:10.1007/s40336-020-00376-y
43. Prando S, de Godoi Carneiro C, Robilotto CC, Sapienza MT. Comparison of different quantification methods for 18F-fluorodeoxyglucose-positron emission tomography studies in rat brains. *Clinics (Sao Paulo)* (2019) **74**:e1273. doi:10.6061/clinics/2019/e1273
44. Chen F, Zhang H, Zhan Y, Huang X, He Z, Ma D, et al. Preclinical and clinical evaluation of [64Cu]Cu-PSMA-Q PET/CT for prostate cancer detection and its comparison with [18F]FDG imaging. *Scientific Rep* (2025) **15**:14431. doi:10.1038/s41598-025-98757-8
45. England CG, Ehlerding EB, Hernandez R, Rekoske BT, Graves SA, Sun H, et al. Preclinical pharmacokinetics and biodistribution studies of 89Zr-labeled pembrolizumab. *J Nucl Med* (2017) **58**:162–8. doi:10.2967/jnumed.116.177857
46. Huang S-C. Anatomy of SUV. *Nucl Med Biol* (2000) **27**:643–6. doi:10.1016/S0969-8051(00)00155-4
47. Boellaard R. Need for standardization of 18F-FDG PET/CT for treatment response assessments. *J Nucl Med* (2011) **52**(Suppl. 2):93s–100s. doi:10.2967/jnumed.110.085662
48. Löffler J, Hamp C, Scheidhauer E, Di Carlo D, Solbach C, Abaci A, et al. Comparison of quantification of target-specific accumulation of [18F]F-siPSMA-14 in the HET-CAM model and in mice using PET/MRI. *Cancers* (2021) **13**:4007. doi:10.3390/cancers13164007
49. Kesar AG. Effect of prenatal chronic noise exposure on the growth and development of body and brain of chick embryo. *Int J Appl Basic Med Res* (2014) **4**:3–6. doi:10.4103/2229-516x.125666
50. Morita VS, Boleli IC, Cargnelutti Filho A. Hematological values and body, heart and liver weights of male and female broiler embryos of young and old breeder eggs. *Revista Brasileira de Ciência Avícola* (2009) **11**:7–15. doi:10.1590/s1516-635x2009000100002
51. Deleze S, Waldron A-M, Richardson JC, Schmidt M, Langlois X, Stroobants S, et al. The effects of physiological and methodological determinants on 18F-FDG mouse brain imaging exemplified in a double transgenic alzheimer model. *Mol Imaging* (2016) **15**:1536012115624919. doi:10.1177/1536012115624919
52. Baldensperger T, Eggen M, Kappen J, Winterhalter PR, Pfirrmann T, Glomb MA. Comprehensive analysis of posttranslational protein modifications in aging of subcellular compartments. *Scientific Rep* (2020) **10**:7596. doi:10.1038/s41598-020-64265-0
53. Luan Z, Saito Y, Miyata H, Ohama E, Ninomiya H, Ohno K. Brainstem neuropathology in a mouse model of Niemann–Pick disease type C. *J Neurol Sci* (2008) **268**:108–16. doi:10.1016/j.jns.2007.11.018
54. Fueger BJ, Czernin J, Hildebrandt I, Tran C, Halpern BS, Stout D, et al. Impact of animal handling on the results of 18F-FDG PET studies in mice. *J Nucl Med* (2006) **47**:999–1006.
55. Krueger MA, Calaminus C, Schmitt J, Pichler BJ. Circadian rhythm impacts preclinical FDG-PET quantification in the brain, but not in xenograft tumors. *Scientific Rep* (2020) **10**:5587. doi:10.1038/s41598-020-62532-8
56. Mannheim JG, Mamach M, Reder S, Traxl A, Mucha N, Disselhorst JA, et al. Reproducibility and comparability of preclinical PET imaging data: a multicenter small-animal PET study. *J Nucl Med* (2019) **60**:1483–91. doi:10.2967/jnumed.118.221994
57. Welniak-Kaminska M, Fiedorowicz M, Orzel J, Bogorodzki P, Modlinska K, Stryjek R, et al. Volumes of brain structures in captive wild-type and laboratory rats: 7T magnetic resonance *in vivo* automatic atlas-based study. *PLOS ONE* (2019) **14**:e0215348. doi:10.1371/journal.pone.0215348
58. Azevedo ÍM, Macedo Filho R, Rocha KBF, Oliveira CN, Medeiros AC. Diagnostic accuracy of 18F-FDG-PET in abdominal sepsis in rats. *Acta Cir Bras* (2020) **35**:e202000505. doi:10.1590/s0102-865020200050000005
59. Tsuji AB, Morita M, Li X-K, Sogawa C, Sudo H, Sugyo A, et al. 18F-FDG PET for semiquantitative evaluation of acute allograft rejection and immunosuppressive therapy efficacy in rat models of liver transplantation. *J Nucl Med* (2009) **50**:827–30. doi:10.2967/jnumed.108.058925
60. Zhang Z, Wei T, Hou J, Li G, Yu S, Xin W. Tetramethylpyrazine scavenges superoxide anion and decreases nitric oxide production in human polymorphonuclear leukocytes. *Life Sci* (2003) **72**:2465–72. doi:10.1016/s0024-3205(03)00139-5
61. Skovgaard D, Kjaer M, El-Ali H, Kjaer A. 18F-Fluorodeoxyglucose and PET/CT for noninvasive study of exercise-induced glucose uptake in rat skeletal muscle and tendon. *Eur J Nucl Med Mol Imaging* (2009) **36**:859–68. doi:10.1007/s00259-008-1020-x
62. Brown WH, Pearce L, Van Allen CM. Organ weights of normal rabbits. *J Exp Med* (1925) **42**:69–82. doi:10.1084/jem.42.1.69
63. Wang H, Xie X, Duan Y, Chai L, Li K, Qiu J, et al. Rabbit systemic glucose metabolism map by total-body dynamic PET/CT technology. *Nucl Med Commun* (2023) **44**:1144–50. doi:10.1097/mnm.0000000000001767
64. Fu L, Chen C, Tian Y-G, Guo K-Y, Wu S-J, Wang Y-J. Diagnostic value of [18F]FDG-PET/CT in acute hepatic radiation toxicity: a Tibet minipig model. *Nucl Sci Tech* (2016) **27**:29. doi:10.1007/s41365-016-0030-9
65. Lee YA, Kim JI, Lee JW, Cho YJ, Lee BH, Chung HW, et al. Effects of various anesthetic protocols on 18F-fluorodeoxyglucose uptake into the brains and hearts of normal miniature pigs (*Sus scrofa domestica*). *J Am Assoc Lab Anim Sci* (2012) **51**:246–52.
66. Hartmann P, Ramseier A, Gudat F, Mihatsch MJ, Polasek W, Geisenhoff C. Das Normgewicht des Gehirns beim Erwachsenen in Abhängigkeit von Alter, Geschlecht, Körpergröße und Gewicht. *Der Pathologe* (1994) **15**:165–70. doi:10.1007/s002920050040
67. Zwezerijnen GJC, Eertink JJ, Ferrández MC, Wieggers SE, Burggraaf CN, Lugtenburg PJ, et al. Reproducibility of [18F]FDG PET/CT liver SUV as reference or normalisation factor. *Eur J Nucl Med Mol Imaging* (2023) **50**:486–93. doi:10.1007/s00259-022-05977-5
68. Laffon E, Adhoute X, de Clermont H, Marthan R. Is liver SUV stable over time in 18F-FDG PET imaging? *J Nucl Med Technology* (2011) **39**:258–63. doi:10.2967/jnmt.111.090027
69. Dias AH, Hansen AK, Munk OL, Gormsen LC. Normal values for 18F-FDG uptake in organs and tissues measured by dynamic whole body multiparametric FDG PET in 126 patients. *Ejnmri Res* (2022) **12**:15. doi:10.1186/s13550-022-00884-0
70. Vines DC, Green DE, Kudo G, Keller H. Evaluation of mouse tail-vein injections both qualitatively and quantitatively on small-animal PET tail scans. *J Nucl Med Technology* (2011) **39**:264–70. doi:10.2967/jnmt.111.090951
71. Alstrup A, Smith D. Anaesthesia for positron emission tomography scanning of animal brains. *Lab Anim* (2013) **47**:12–8. doi:10.1258/la.2012.011173
72. Foster NL, VanDerSpek AF, Aldrich MS, Berent S, Hichwa RH, Sackellares JC, et al. The effect of diazepam sedation on cerebral glucose metabolism in Alzheimer's disease as measured using positron emission tomography. *J Cereb Blood Flow Metab* (1987) **7**:415–20. doi:10.1038/jcbfm.1987.84



OPEN ACCESS

*CORRESPONDENCE

Yapan Yang,
✉ zhogzhengfu73@hotmail.com

RECEIVED 24 January 2025

ACCEPTED 28 May 2025

PUBLISHED 17 June 2025

CITATION

Du X, Li X, Yue S, Sun Y, Zhao M, Zhou L, Wang X and Yang Y (2025) Correlation study of CAR, PLR, NLR with the prognosis of cardiogenic cerebral embolism patients.

Exp. Biol. Med. 250:10517.

doi: 10.3389/ebm.2025.10517

COPYRIGHT

© 2025 Du, Li, Yue, Sun, Zhao, Zhou, Wang and Yang. This is an open-access article distributed under the terms of the [Creative Commons Attribution License \(CC BY\)](https://creativecommons.org/licenses/by/4.0/). The use, distribution or reproduction in other forums is permitted, provided the original author(s) and the copyright owner(s) are credited and that the original publication in this journal is cited, in accordance with accepted academic practice. No use, distribution or reproduction is permitted which does not comply with these terms.

Correlation study of CAR, PLR, NLR with the prognosis of cardiogenic cerebral embolism patients

Xiaojing Du¹, Xiaohui Li¹, Sheng Yue¹, Yuzhen Sun¹, Mengzhen Zhao¹, Lingshan Zhou¹, Xingwei Wang¹ and Yapan Yang^{2*}

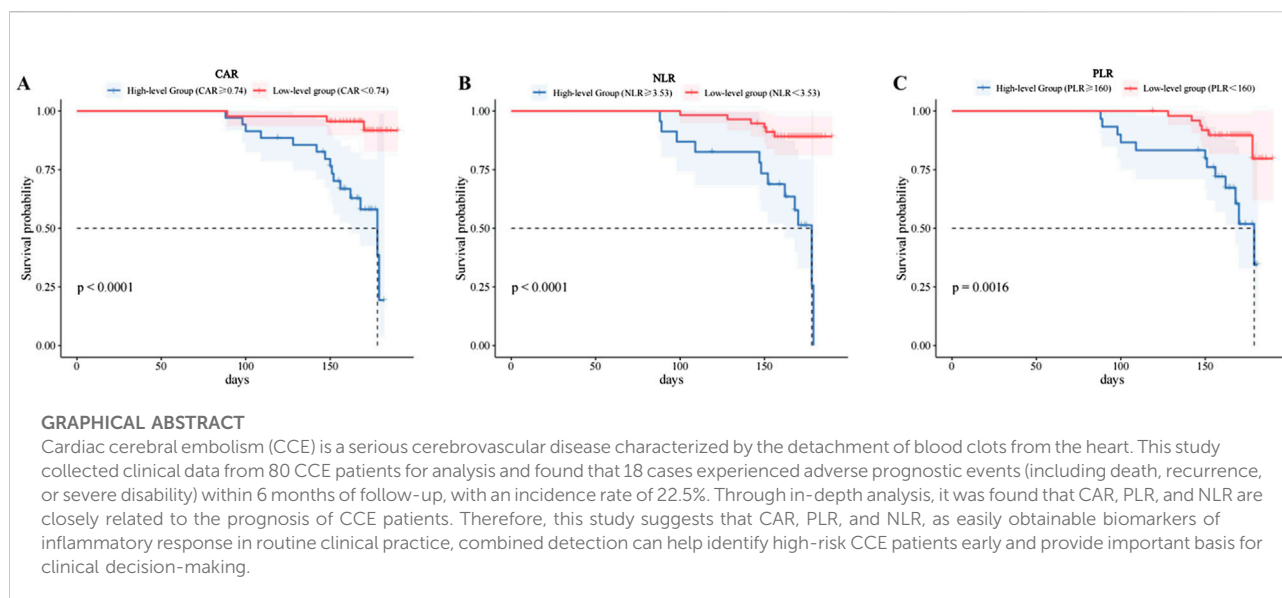
¹Department of Comprehensive Intensive Care Unit, Central China Fuwai Hospital, Fuwai Central China Cardiovascular Hospital, Central China Fuwai Hospital of Zhengzhou University, Heart Center of Henan Provincial People's Hospital, Zhengzhou, Henan, China, ²Department of Cardiology, Central China Fuwai Hospital, Fuwai Central China Cardiovascular Hospital, Central China Fuwai Hospital of Zhengzhou University, Heart Center of Henan Provincial People's Hospital, Zhengzhou, Henan, China

Abstract

This study explored the association between inflammatory biomarkers—C-reactive protein to albumin ratio (CAR), platelet to lymphocyte ratio (PLR), and neutrophil to lymphocyte ratio (NLR)—and the prognosis of patients with cardiogenic cerebral embolism (CCE). We retrospectively analyzed data from 80 CCE patients diagnosed between June 2020 and June 2024, categorizing them into favorable and unfavorable prognosis groups based on outcomes such as death, recurrence, and disability. The CAR, PLR, and NLR values were calculated from routine blood tests, and statistical analyses, including Spearman correlation, multivariate logistic regression, and ROC curve analysis, were performed to examine their prognostic significance. Results showed that the unfavorable prognosis group had significantly higher CAR, PLR, and NLR values compared to the favorable group ($P < 0.05$). Spearman correlation analysis revealed positive associations between these biomarkers and prognosis ($r = 0.319$ for CAR, 0.238 for PLR, 0.251 for NLR, all $P < 0.05$). Multivariate analysis identified CAR and NLR as independent risk factors for unfavorable prognosis (OR = 1.034 for CAR, OR = 3.887 for NLR). ROC analysis determined optimal cutoff values for CAR (>0.74), PLR (>160.00), and NLR (>3.53) to predict unfavorable prognosis with AUCs of 0.796, 0.694, and 0.705, respectively. The combined biomarker test yielded an AUC of 0.899. Kaplan-Meier survival analysis indicated significantly lower survival rates for patients with higher levels of CAR, PLR, and NLR ($P < 0.05$). In conclusion, elevated CAR, PLR, and NLR are reliable indicators of a poor prognosis in CCE patients.

KEYWORDS

cardiogenic cerebral embolism, prognosis, CAR, PLR, NLR



Impact statement

In recent years, inflammatory biomarkers such as the C-reactive protein to albumin ratio (CAR), platelet to lymphocyte ratio (PLR), and neutrophil to lymphocyte ratio (NLR) have been utilized in the prognostic assessment of various diseases. This study aimed to examine the correlation between CAR, PLR, and NLR, and the prognosis of patients with cardiogenic cerebral embolism (CCE), as well as to evaluate their potential as prognostic predictors.

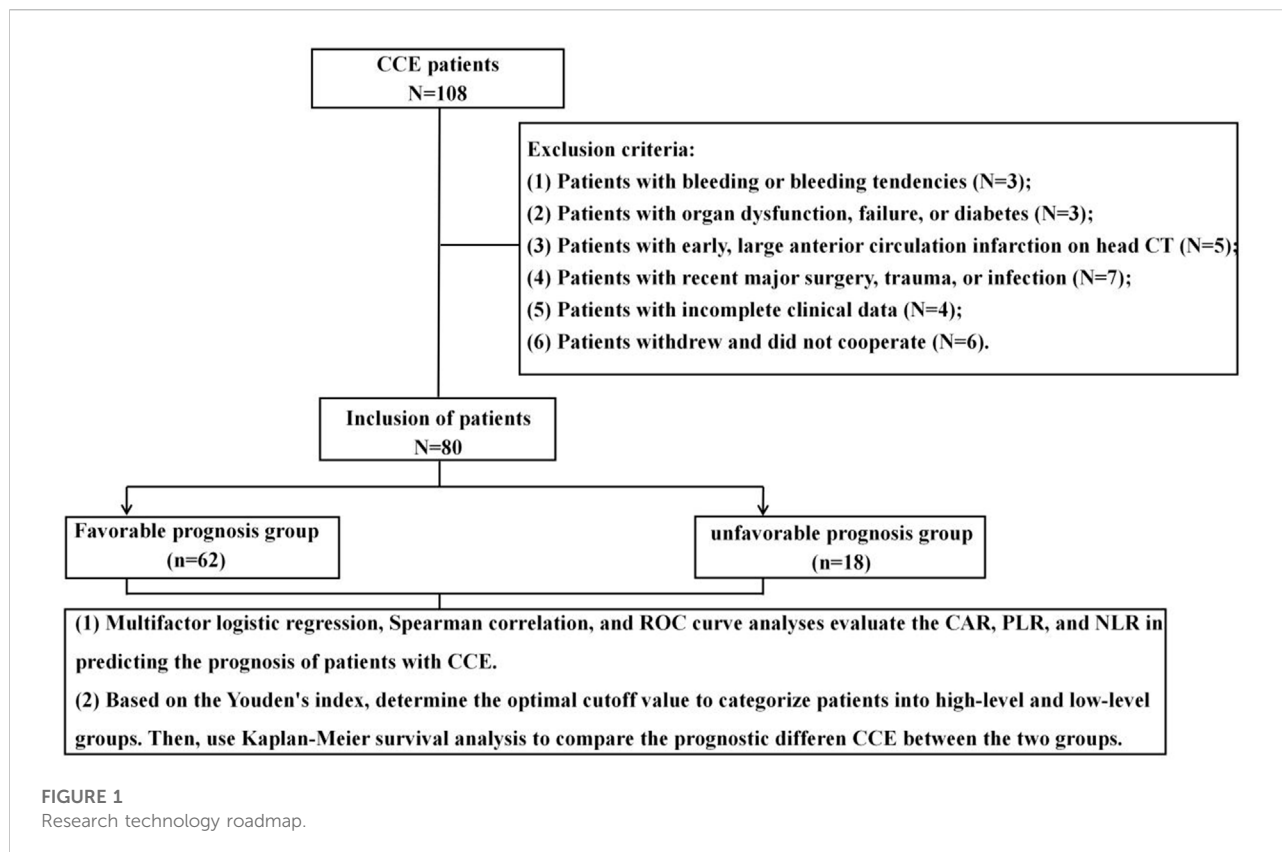
Introduction

Cardiac cerebral embolism (CCE) is a significant cerebrovascular condition characterized by the dislodgment of thrombus from the heart. This thrombus can enter the brain via the bloodstream, leading to the obstruction of cerebral blood vessels, which subsequently results in neurological dysfunction, including symptoms such as limb weakness and slurred speech. In severe cases, this condition may lead to permanent neurological impairment [1]. Globally, CCE account for approximately 15%–30% of ischemic strokes and are typically associated with higher morbidity, disability, and mortality rates, posing a significant threat to the lives and health of patients [2]. Consequently, the early identification of high-risk factors for CCE and timely intervention hold critical clinical importance for enhancing patient prognosis.

Brain natriuretic peptide (BNP) and D-dimer are widely utilized biomarkers for diagnosing and monitoring treatment responses in patients with CCE. These biomarkers have been endorsed by authoritative organizations, including the European Society of Cardiology and the American Society

of Hematology [3, 4]. However, the high costs associated with BNP and D-dimer testing, coupled with limited availability in some primary medical institutions, underscore the necessity of identifying more economical and straightforward predictive indicators. In recent years, an increasing number of studies have focused on the potential role of inflammatory markers in CCE. Specifically, the C-reactive protein to albumin ratio (CAR), platelet to lymphocyte ratio (PLR), and neutrophil to lymphocyte ratio (NLR) are gaining recognition as promising new biomarkers.

The CAR serves as a comprehensive indicator of both inflammation and nutritional status. An elevation in CAR reflects the body's inflammatory response and malnutrition, and is associated with poor prognoses in various diseases, including cardiovascular disorders and tumors [5, 6]. In cases of CCE, elevated CAR may indicate more severe cerebrovascular injury and a heightened inflammatory response, both of which are closely linked to poor outcomes. The platelet-to-lymphocyte ratio (PLR) and neutrophil-to-lymphocyte ratio (NLR) are additional indicators that reflect the body's inflammatory and immune status; their variations may also be significantly related to the occurrence and progression of CCE. An increase in PLR suggests that the body is experiencing inflammation [7], while an increase in NLR indicates an enhanced inflammatory response mediated by neutrophils, coupled with a diminished immune response mediated by lymphocytes [8]. This state of immune imbalance may facilitate the formation and shedding of thrombi, thereby elevating the risk of CCE. Therefore, the purpose of this study is to explore the correlation between the levels of the three inflammatory markers, CAR, PLR, and NLR, and the prognosis in patients with CCE. It is hoped that this research can provide new reference criteria for early warning, condition assessment, and prognostic judgment of CCE.



Materials and methods

Study method and object

A total of 108 CCE patients treated at our hospital from June 2020 to June 2024 were considered for this study, from which 80 patients were selected as research subjects based on predefined inclusion and exclusion criteria. The research flow chart is presented in Figure 1. Subsequently, patients were categorized into two groups based on the occurrence of adverse prognostic events (such as death, recurrence, or severe disability) during hospitalization and within a 6-month follow-up period post-discharge: a favorable prognosis group and a unfavorable prognosis group. Among them, severe disability is defined as; Major body organ defects, obvious organ deformities, moderate body organ dysfunction, serious complications, etc. The favorable prognosis group consisted of patients who did not experience any of the aforementioned adverse events during hospitalization or within the 6-month follow-up period; conversely, the unfavorable prognosis group included patients who experienced any adverse prognostic events during this timeframe. All enrolled patients provided informed consent, and this study received approval from Fuwai Central China Cardiovascular Hospital Ethics Committee. (No. 2020-05).

Inclusion criteria: (1) The patient meets the diagnostic criteria for CCE [9]; (2) The patient is diagnosed with CCE through

examinations such as head CT, magnetic resonance imaging (MRI), echocardiography, etc; (3) The patient's baseline National Institutes of Health Stroke Scale (NIHSS) score is ≥ 6 points; (4) Patients must have complete clinical data and follow-up data.

Exclusion criteria: (1) Patients with active bleeding or known bleeding tendencies; (2) Patients with significant organ dysfunction or failure, or severe diabetes; (3) Patients whose head CT indicates early and extensive infarction in the anterior circulation, specifically those exceeding one-third of the middle cerebral artery blood supply area; (4) Patients with a history of major surgery, trauma, or infection within the past 2 months; (5) Patients who refuse to participate in this study or who are unable to complete follow-up assessments.

Methods

The general clinical data of all patients were retrospectively collected, encompassing age, gender, height, history of hypertension, diabetes, hyperlipidemia, smoking history, drinking history, the presence of congestive heart failure (CHF), and the NIHSS score recorded upon admission. Additionally, 5 mL of fasting venous blood was collected from each patient within 24 h of admission, which was then centrifuged at 4°C at 3,000 rpm for 30 min to obtain serum samples. These samples were subsequently

sent to our hospital's laboratory department for routine blood count and blood cell calculation. All patients received standardized treatments, including intravenous thrombolysis, anticoagulation, anti-platelet aggregation, lipid regulation and plaque stabilization, as well as management of blood pressure and blood sugar levels, neuronutrition, and symptomatic supportive care. Clinical outcomes were assessed through telephone follow-up or outpatient review within 3 months post-discharge, focusing on adverse prognostic events such as death, recurrence, or severe disability.

Routine blood test

Utilizing an automatic biochemical analyzer (model GS480Plus, manufactured by Shenzhen Jinrui Biotechnologies Co., Ltd., registration number 20162220670), we analyzed the levels of uric acid (UA), homocysteine (HCY), creatinine (Cr), triglyceride (TG), low-density lipoprotein (LDL-C), and high-density lipoprotein (HDL-C). Furthermore, the concentrations of serum albumin (ALB) and C-reactive protein (CRP) were assessed via immunoturbidimetry. Subsequently, the CAR was computed based on these measurements.

Blood cell count

Using an automatic blood cell analyzer (manufacturer: Shenzhen Pukang Electronics Co., Ltd.; model: PE-7000; registration number: 20182220948), we determined the counts of neutrophils, lymphocytes, and platelets. Additionally, we calculated the NLR and the PLR based on these counts.

Statistical treatment

Data analysis was performed using SPSS 26.0 software. Normality tests were conducted on continuous variables. Normally distributed continuous data were presented as mean \pm standard deviation, and t-tests were used for intergroup comparisons. Categorical data were expressed as counts and percentages, and χ^2 tests were applied for intergroup comparisons. Multivariate logistic regression analysis was utilized to identify factors influencing the prognosis of CCE patients, with significant variables serving as independent variables and patient prognosis as the dependent variable, to evaluate the predictive power of these factors for prognosis. Moreover, Spearman's rank correlation analysis was conducted to assess the correlation between each variable and patient prognosis. Receiver operating characteristic (ROC) curves were generated, and the area under the curve (AUC) and Youden's index were calculated to further validate the predictive performance of CAR, PLR, and NLR, both individually and in combination, for the prognosis of CCE patients. Optimal cut-off values were determined based on Youden's index, and patients were categorized into high-level and low-level groups. Kaplan-Meier survival analysis was subsequently employed to compare the prognostic differences between these groups. A *P*-value of less than 0.05 was deemed to indicate statistical significance.

Results

Patient characteristics

A total of 80 CCE patients were included in the study, of whom 18 experienced adverse prognostic events (including death, recurrence, or severe disability) within 6 months of follow-up and were classified as the unfavorable prognosis group. The remaining 62 patients were classified as the favorable prognosis group. The baseline characteristics of the two patient groups are detailed in [Table 1](#). In the unfavorable prognosis group, the average age of patients and the NIHSS score were higher, and the proportion of patients with hypertension and congestive heart failure was also greater than that in the favorable prognosis group, with these differences reaching statistical significance ($P > 0.05$).

Laboratory indicators

Further analysis of the laboratory indicators for the two patient groups revealed that the values of CAR, PLR, and NLR in the unfavorable prognosis group were significantly higher than those in the favorable prognosis group, with the differences being statistically significant ($P < 0.05$), as shown in [Table 2](#).

Correlation analysis of adverse prognosis in patients with CCE

Pearson's correlation analysis revealed that age, NIHSS score, hypertension, congestive heart failure, CAR, PLR, and NLR were significantly associated with unfavorable prognosis in patients. Specifically, age, NIHSS score, and increases in CAR, PLR, and NLR demonstrated strong correlations with unfavorable prognosis, with correlation coefficients of $r = 0.304, 0.274, 0.319, 0.238,$ and 0.251 , respectively ($P < 0.05$). Additionally, patients with both hypertension and congestive heart failure exhibited a significantly elevated risk of adverse prognosis, with correlation coefficients of $r = 0.283$ and 0.306 ($P < 0.05$), as shown in [Table 3](#).

Multivariate logistic regression analysis of factors affecting adverse prognosis in patients with CCE

In order to pinpoint the independent risk factors for unfavorable outcomes in patients with CCE, a multivariate logistic regression analysis was performed. Variables that exhibited significant differences in the univariate analysis, including age, NIHSS score, hypertension, congestive heart failure, CAR, PLR, and NLR, were incorporated into the multivariate logistic regression model. The analysis revealed that

TABLE 1 Comparison of baseline characteristics between the two patient groups.

Characteristics	Type	Favorable prognosis group (n = 18)	Unfavorable prognosis group (n = 62)	P
Age		52.00 ± 8.20	45.76 ± 8.29	0.006
Sex	Man	11 (61.11)	48 (77.42)	0.166
	Woman	7 (38.89)	14 (22.58)	
Hypertension	Yes	8 (44.44)	10 (16.13)	0.011
	Deny	10 (55.56)	52 (83.87)	
Diabetes mellitus	Yes	4 (22.22)	7 (11.29)	0.236
	Deny	14 (77.78)	55 (88.71)	
Hyperlipemia	Yes	5 (27.78)	15 (24.19)	0.757
	Deny	13 (72.22)	47 (75.81)	
History of smoking	Yes	6 (33.33)	16 (25.81)	0.529
	Deny	12 (66.67)	46 (74.19)	
History of drinking	Yes	5 (27.78)	25 (40.32)	0.333
	Deny	13 (72.22)	37 (59.68)	
CHF	Yes	8 (44.44)	9 (14.52)	0.006
	Deny	10 (55.56)	53 (85.48)	
NIHSS score at admission		15.83 ± 3.82	13.42 ± 3.50	0.014

Note: Measurement data in normal distribution in $\bar{x} \pm s$, t-test for comparison between groups; count data in n and% for χ^2 checkout. CHF, Congestive heart failure; NIHSS, national institutes of health stroke scale.

TABLE 2 Comparison of the experimental indicators between the two patient groups.

Characteristics	Favorable prognosis group (n = 18)	Unfavorable prognosis group (n = 62)	P
Neutrophil count ($10^9/L$)	7.18 ± 0.97	6.74 ± 0.92	0.077
Lymphocyte count ($10^9/L$)	1.41 ± 0.32	1.68 ± 0.56	0.050
Platelet count ($10^9/L$)	227.94 ± 16.54	216.84 ± 21.98	0.051
C-reactive protein (mg/L)	22.32 ± 6.76	25.95 ± 6.87	0.051
ALB (g/L)	38.07 ± 7.62	33.88 ± 8.34	0.059
CAR	0.80 ± 0.26	0.60 ± 0.21	0.004
PLR	170.02 ± 38.00	143.21 ± 48.32	0.034
NLR	4.62 (3.78, 5.84)	3.09 (2.38, 5.23)	0.008
UA ($\mu\text{mol/L}$)	305.34 ± 24.09	314.35 ± 26.31	0.197
HCY($\mu\text{mol/L}$)	13.58 ± 3.15	13.08 ± 2.98	0.534
Cr ($\mu\text{mol/L}$)	65.66 ± 4.81	66.42 ± 5.04	0.570
TG (mmol/L)	1.48 ± 0.38	1.48 ± 0.38	0.960
LDL (mmol/L)	2.88 ± 0.76	2.67 ± 0.60	0.234
HDL (mmol/L)	1.10 ± 0.25	1.17 ± 0.30	0.347

Note: Measurement data conform to normal distribution are expressed as $\bar{x} \pm s$, t-test for comparison between groups; measurement data are not normally distributed as [M (P_{25} , P_{75})], non-parametric rank sum test; count data are presented as n and%, χ^2 checkout. CAR, C-reactive protein to albumin ratio; NLR, neutrophil-to-lymphocyte ratio; PLR, platelet-to-lymphocyte ratio; UA, uric acid; HCY, Homocysteine; Cr, Creatinine; TG, Triglyceride; LDL, low-density lipoprotein; HDL, high-density lipoprotein.

TABLE 3 Association with unfavorable prognosis in patients with CES.

Project	Statistical value	Age	NIHSS grade	Hypertension	CHF	CAR	PLR	NLR
prognosis	<i>r</i>	0.304	0.274	0.283	0.306	0.319	0.238	0.251
	<i>P</i>	0.006	0.014	0.011	0.006	0.004	0.034	0.024

Note: NIHSS, national institutes of health stroke scale; CHF, Congestive heart failure; CAR, C-reactive protein to albumin ratio; NLR, neutrophil-to-lymphocyte ratio; PLR, platelet-to-lymphocyte ratio.

TABLE 4 Multifactor logistic analysis of adverse prognosis in patients with CCE.

Variable	β	SE	Wald χ^2	<i>P</i>	OR (95%CI)
Age	0.091	0.035	6.640	0.010	1.095 (1.022–1.173)
NIHSS score at admission	0.279	0.136	4.209	0.040	1.321 (1.013–1.725)
Hypertension	1.455	0.955	2.321	0.128	4.283 (0.659–27.827)
CHF	0.489	1.028	0.226	0.634	1.631 (0.218–12.221)
CAR	0.033	0.016	4.338	0.037	1.034 (1.002–1.067)
PLR	0.016	0.009	2.959	0.085	1.016 (0.998–1.034)
NLR	1.358	0.616	4.861	0.027	3.887 (1.163–12.993)

Note: NIHSS, national institutes of health stroke scale; CHF, Congestive heart failure; CAR, C-reactive protein to albumin ratio; NLR, neutrophil-to-lymphocyte ratio; PLR, platelet-to-lymphocyte ratio.

age (OR = 1.095, 95% CI: 1.022–1.173, *P* = 0.010), NIHSS score (OR = 1.321, 95% CI: 1.013–1.725, *P* = 0.040), CAR (OR = 1.034, 95% CI: 1.002–1.067, *P* = 0.037), and NLR (OR = 3.887, 95% CI: 1.163–12.993, *P* = 0.027), are independent predictors of adverse outcomes in CCE patients. For more detailed information, refer to [Table 4](#).

ROC curve analysis of factors affecting unfavorable prognosis in patients with CCE

To further evaluate the predictive power of the aforementioned variables for the prognosis of CCE patients, a ROC curve analysis was conducted. The results indicated that age, NIHSS score at admission, CAR, PLR, and NLR possess significant predictive capabilities for adverse outcomes in CCE patients, as detailed in [Table 5](#) (*P* < 0.05). Specifically, the AUC values for age, NIHSS score at admission, CAR, PLR, and NLR were 0.707, 0.737, 0.796, 0.694, and 0.705, respectively, each demonstrating notable predictive value, as illustrated in [Figure 2](#). Notably, CAR exhibited the highest AUC, signifying its superior predictive efficacy for adverse outcomes in CCE patients. Further analysis revealed that the combined use of CAR, PLR, and NLR resulted in an elevated AUC value of 0.889 (95% CI: 0.792–0.986, *P* < 0.05), accompanied by relatively high sensitivity and specificity of 93.5% and 77.8%, respectively. This finding underscores that the joint predictive application of CAR, PLR, and NLR can significantly enhance the precision of prognostic predictions for CCE patients.

Kaplan-Meier survival analysis of CAR, PLR, and NLR levels on the prognosis of CCE patients

According to the Youden index, the optimal cutoff values for CAR, PLR, and NLR are 0.74, 160.00, and 3.53, respectively. The CAR, PLR, and NLR levels were categorized into two groups: high-level and low-level. Kaplan-Meier survival analysis was employed to compare the prognostic differences between these two patient groups. The results indicated that the survival rates of patients in the high-level CAR group (≥ 0.74), high-level PLR group (≥ 160.00), and high-level NLR group (≥ 3.53) were significantly lower than those in the low-level group, with the differences between the two groups being statistically significant (*P* < 0.05), as shown in [Figure 3](#).

Discussion

CCE is characterized by inadequate cerebral blood perfusion due to cardiogenic factors, including atrial fibrillation, myocardial infarction, and valvular heart disease. These factors can lead to brain tissue damage resulting from ischemia, hypoxia, and, in severe cases, necrosis. The disease is marked by sudden onset and rapid progression, making early diagnosis and intervention essential to minimize disability and mortality rates among patients [10]. Furthermore, inflammation plays a significant role in the onset and progression of CCE. Inflammatory mediators, such as cytokines, chemokines, and

TABLE 5 ROC curve analysis of factors affecting adverse prognosis in patients with CCE.

Variable	AUC	SE	P	95% CI	Sensitivity (%)	Specificity (%)	Youden's index
Age	0.707	0.076	0.008	0.559–0.855	50.0	87.1	0.371
NIHSS score at admission	0.737	0.070	0.002	0.599–0.875	88.7	50.0	0.387
hypertension	0.642	0.079	0.069	0.486–0.797	83.9	44.4	0.283
CHF	0.650	0.079	0.054	0.494–0.805	85.5	44.4	0.299
CAR	0.796	0.053	<0.001	0.692–0.899	71.0	83.3	0.543
PLR	0.694	0.064	0.013	0.569–0.819	66.7	71.0	0.377
NLR	0.705	0.085	0.008	0.538–0.871	82.3	66.7	0.490
CAR + PLR + NLR	0.889	0.050	<0.001	0.792–0.986	93.5	77.8	0.713

Note: NIHSS, national institutes of health stroke scale; CHF, Congestive heart failure; CAR, C-reactive protein to albumin ratio; NLR, neutrophil-to-lymphocyte ratio; PLR, platelet-to-lymphocyte ratio.

adhesion molecules, can damage vascular endothelial cells, thereby promoting thrombosis [11]. The inflammatory response may also activate platelets and the coagulation system, increasing blood coagulability and exacerbating the ischemic and hypoxic conditions of brain tissue [12]. Consequently, in clinical practice, the condition and prognosis of CCE patients can be assessed by monitoring changes in inflammatory indicators. This study focuses on easily accessible and straightforward experimental indicators, such as the CAR, PLR, and NLR, to investigate the correlation between these inflammatory markers and the prognosis of CCE patients.

The results of this study showed that of the 80 patients with CES, 18 experienced adverse outcome events (including death, recurrence or severe disability) within 6 months of follow-up, and the incidence of adverse outcome events was 22.5%. Studies show that the in-hospital mortality rate in patients with CES is 27.3% [13]. This data closely aligns with the incidence of adverse prognostic events observed in this study, thereby reinforcing the high-risk nature of CES patients. The clinical data and experimental indicators of patients categorized into unfavorable and favorable prognosis groups were analyzed in depth. The analysis revealed that the mean age, NIHSS score at admission, and the proportion of patients with combined hypertension and congestive heart failure were significantly higher in the unfavorable prognosis group compared to those in the favorable prognosis group. Notably, among patients with acute ischemic stroke (AIS), the mean age in the unfavorable prognosis group was 74.00 years, whereas it was only 66.00 years in the favorable prognosis group [14]. Elderly patients often experience physiological decline and a reduction in metabolic rate, among other factors, which contribute to their relatively weak resistance to diseases and diminished rehabilitation capabilities. Consequently, this increases the likelihood of unfavorable prognoses. Additionally, the NIHSS score upon admission serves as a

crucial indicator for assessing patient outcomes. A higher NIHSS score signifies more severe neurological deficits, which are typically associated with poorer prognoses [15]. In addition, patients with hypertension or congestive heart failure experience a significant decline in heart function, which elevates the risk of developing heart disease and associated complications, such as coronary artery disease and diabetes, thereby increasing the likelihood of adverse outcomes. In the experimental indicators, the values of CAR, PLR, and NLR in the unfavorable prognosis group were significantly higher than those in the favorable prognosis group, demonstrating a notable positive correlation with unfavorable prognosis ($r = 0.006, 0.004$, and 0.034). These findings align with previous studies [16], suggesting that these inflammatory indicators possess substantial predictive value concerning the prognosis of CES.

CAR is the ratio of CRP to ALB, which reflects, to some extent, the balance between the body's inflammatory response and nutritional status. CRP, an acute-phase response protein, typically exhibits elevated levels during an inflammatory response in the body [17]. While ALB acts as a negative acute phase reactant, its reduced levels may reflect protein loss due to the poor nutritional status of the organism or the presence of an inflammatory response [18]. Consequently, an increase in CAR levels may signify an exacerbation of the inflammatory response and suggest a deterioration in the patient's nutritional status. Relevant studies suggest that CAR is more effective in indicating inflammatory status than CRP or albumin alone [19]. Yu et al. [20] found that in patients with acute ischemic cerebral infarction (AIS), the CAR is associated with adverse clinical manifestations of AIS, with patients exhibiting high CAR values experiencing higher mortality rates. This finding is consistent with the results of the current study. Furthermore, this study confirmed that CAR is a significant factor influencing the poor prognosis of patients with CCE through multifactorial logistic regression

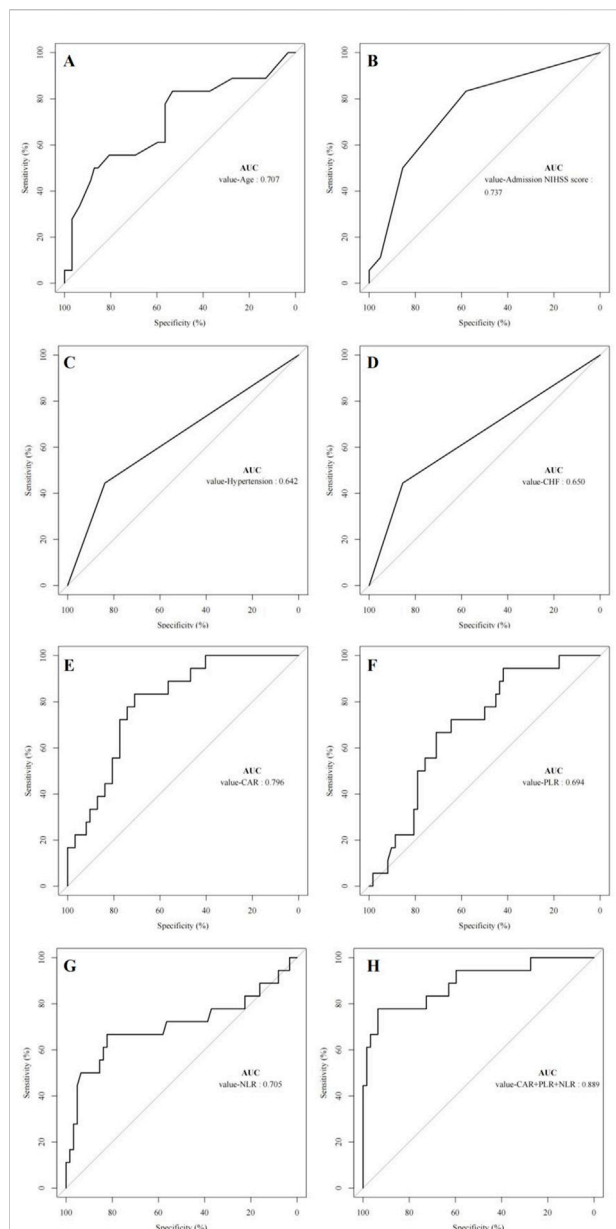


FIGURE 2

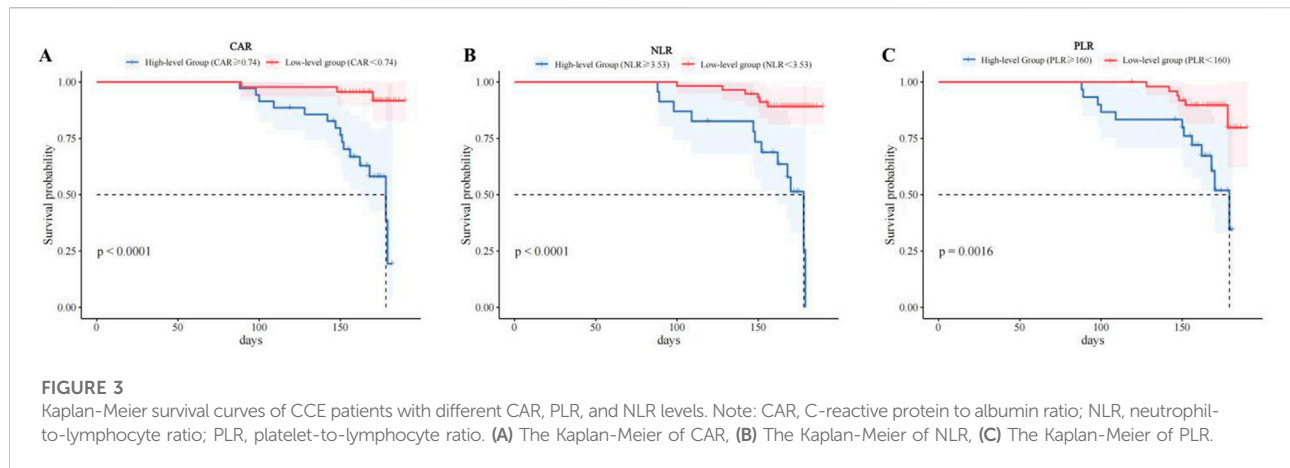
ROC curve analysis affecting the prognosis of CCE patients. Note: NIHSS, national institutes of health stroke scale; CHF, Congestive heart failure; CAR, C-reactive protein to albumin ratio; NLR, neutrophil-to-lymphocyte ratio; PLR, platelet-to-lymphocyte ratio. (A) The AUC of age, (B) The AUC of NIHSS, (C) The AUC of hypertension, (D) The AUC of CHF, (E) The AUC of CAR, (F) The AUC of PLR, (G) The AUC of NLR, (H) The AUC of CAR+PLR+NLR.

analysis and ROC curve analysis. Specifically, the odds ratio (OR) for CAR was 1.034 (95% CI: 1.002–1.067), and the AUC reached 0.796, indicating that CAR possesses a high predictive value in CCE. Additionally, Kaplan-Meier survival analysis demonstrated that the survival time of patients with a CAR value greater than 0.74 was significantly shorter than that of

patients with lower CAR values, further underscoring the importance of CAR in assessing the prognosis of CCE patients.

Similarly, elevated NLR and PLR values are recognized as independent risk factors for poor prognosis in various cardiovascular diseases [21]. PLR, which reflects the ratio of platelets to lymphocytes, serves as a comprehensive indicator of platelet activation and immune status. The activation of platelets plays a crucial role in thrombosis, while lymphocytes are integral to the body's immune response [22, 23]. An elevated PLR may indicate that the body is experiencing an inflammatory response or is in an environment conducive to thrombosis. In the multivariate logistic regression analysis conducted in this study, the OR for PLR was found to be 1.016 (95% CI: 0.998–1.034), although this did not achieve statistical significance. This finding aligns with the results reported by Vakhshoori et al. [24]. While Zhai et al [25] posited that the platelet-to-lymphocyte ratio (PLR) serves as an independent predictor of in-hospital mortality among patients in the cardiac intensive care unit (CICU). An increase in PLR is significantly associated with higher in-hospital mortality rates, as well as prolonged lengths of stay in both the CICU and the hospital. Subsequent ROC curve analysis yielded an AUC value of 0.694, suggesting that PLR possesses a moderate predictive capability regarding poor prognosis in patients with CCE, albeit slightly inferior to that of the CAR. This discrepancy may be attributed to the intricate pathophysiological mechanisms underlying CCE, including factors such as the nature, size, and location of emboli, as well as the patient's underlying conditions and immune status. Furthermore, patients with CCE frequently present with multiple comorbidities, such as hypertension and diabetes, which could influence PLR levels and thereby confound its direct association with mortality risk. Consequently, future research should involve larger sample sizes, extended follow-up durations, and more stringent statistical methodologies to further investigate the prognostic value of PLR in CCE. Additionally, integrating other inflammatory markers (e.g., CAR, NLR) and clinical indicators may enhance the accuracy of prognostic assessments.

NLR serves as a biomarker for inflammatory status. Following the occurrence of CCE, neutrophils are rapidly recruited to the ischemic injury site to participate in the inflammatory response, resulting in a significant increase in their numbers. Concurrently, the number of lymphocytes may decrease due to factors such as the stress response, leading to an elevated NLR and an increased risk of poor prognosis [26]. This result is consistent with previous studies [24, 27], which all confirmed the important value of NLR in the prognosis evaluation of cardiovascular diseases. The normal NLR range is typically 1 to 2. Values above 3.0 or below 0.7 may indicate pathology. Previous studies have confirmed the prognostic significance of NLR in cardiovascular disease [28]. Quan et al. [29] included 590 patients with acute ischemic stroke and



found that an elevated NLR of 3.872 serves as a predictive indicator for malignant hemorrhagic transformation, poor functional outcomes, and short-term mortality. In our study, a similar finding was observed, with an increased mortality rate among CCE patients when NLR exceeded 3.5. This finding corroborates the reliability of NLR as a prognostic tool for CCE patients. Moreover, our study revealed that the combined detection of CAR, PLR, and NLR may further enhance the predictive accuracy for the prognosis of CCE patients. Although each individual marker has demonstrated certain predictive efficacy, the integration of multiple indicators allows for a comprehensive assessment of the body's inflammatory response, coagulation status, and immune condition, thereby providing a more holistic evaluation of patient prognosis. Therefore, in future clinical practice, we propose considering the combined detection of CAR, PLR, and NLR as an important means of prognostic assessment for CCE patients. This approach is expected to further improve treatment outcomes and quality of life for these patients.

In summary, the CAR, PLR, and NLR are biomarkers of inflammatory response that can be easily obtained in routine clinical practice. When used in combination, their detection can facilitate the early identification of high-risk patients with CCE and provide a crucial basis for clinical decision-making. Although this study yielded meaningful findings, several limitations must be acknowledged. First, the study was retrospective, conducted at a single center, and involved a small sample size, which may introduce selection bias and reporting bias. Secondly, the follow-up period was relatively short and may not adequately reflect the long-term prognosis of the patients. Finally, due to the limitations of retrospective studies, the influencing factors that can be collected in this study are limited, and there is a lack of analysis on factors such as treatment changes, admission time, or stroke severity beyond NIHSS scores. Therefore, future research should involve larger-scale, multi-center, prospective studies to further validate the

prognostic value of these inflammatory markers in CCE. Additionally, it is essential to explore other factors that may influence prognosis in order to provide patients with a more comprehensive and accurate assessment and treatment strategy.

Author contributions

XL, SY, YS, and MZ conducted the experiments, LZ and YY supplied critical reagents, XW and XD wrote the manuscript. All authors contributed to the article and approved the submitted version.

Data availability

The original contributions presented in the study are included in the article/supplementary material, further inquiries can be directed to the corresponding author.

Ethics statement

The studies involving humans were approved by Fuwai Central China Cardiovascular Hospital Ethics Committee (No. 2020-05). The studies were conducted in accordance with the local legislation and institutional requirements. Written informed consent for participation in this study was provided by the participants' legal guardians/next of kin.

Funding

The author(s) declare that financial support was received for the research and/or publication of this article. Curative effect of percutaneous coronary intervention for ischemic heart failure. (No. LHGJ20210098).

Conflict of interest

The author(s) declared no potential conflicts of interest with respect to the research, authorship, and/or publication of this article.

References

1. Yu MY, Caprio FZ, Bernstein RA. Cardioembolic stroke. *Neurol Clin* (2024) 42(3):651–61. doi:10.1016/j.ncl.2024.03.002
2. Celeste F, Muratori M, Mapelli M, Pepi M. The evolving role and use of echocardiography in the evaluation of cardiac source of embolism. *J Cardiovasc Echography* (2017) 27(2):33–44. doi:10.4103/jcecho.jcecho_1_17
3. Collet J, Thiele H, Barbato E, Barthélémy O, Bauersachs J, Bhatt DL, et al. 2020 ESC Guidelines for the management of acute coronary syndromes in patients presenting without persistent ST-segment elevation. *Eur Heart J* (2021) 42(14):1289–367. doi:10.1093/eurheartj/ehaa575
4. Ortel TL, Neumann I, Ageno W, Beyth R, Clark NP, Cuker A, et al. American Society of Hematology 2020 guidelines for management of venous thromboembolism: treatment of deep vein thrombosis and pulmonary embolism. *Blood Adv* (2020) 4(19):4693–738. doi:10.1182/bloodadvances.2020001830
5. Nomoto N, Tate S, Arai M, Iizaka S, Mori C, Sakurai K. Pretreatment nutritional status in combination with inflammation affects chemotherapy interruption in women with ovarian, fallopian tube, and peritoneal cancer. *Nutrients*. (2022) 14(23):5183. doi:10.3390/nu14235183
6. Yang J, Li C, Zheng Y, Gao J, Liu YP, Wang J, et al. The association between high-sensitivity C-reactive protein/albumin ratio and cardiovascular prognosis in patients undergoing percutaneous coronary intervention. *Angiology* (2022) 73(9):818–26. doi:10.1177/00033197221110715
7. Sarkar S, Kannan S, Khanna P, Singh AK. Role of platelet-to-lymphocyte count ratio (PLR), as a prognostic indicator in COVID-19: a systematic review and meta-analysis. *J Med Virol* (2022) 94(1):211–21. doi:10.1002/jmv.27297
8. Quiros-Roldan E, Raffetti E, Donato F, Magoni M, Pezzoli C, Ferraresi A, et al. Neutrophil to lymphocyte ratio and cardiovascular disease incidence in HIV-infected patients: a population-based cohort study. *Plos One* (2016) 11(5):e0154900. doi:10.1371/journal.pone.0154900
9. Doufekias E, Segal AZ, Kizer JR. Cardiogenic and aortogenic brain embolism. *J Am Coll Cardiol* (2008) 51(11):1049–59. doi:10.1016/j.jacc.2007.11.053
10. Morino Y, Nakajima Y. Structural heart intervention for prevention of embolic and hemorrhagic stroke: the new field of neurocardiology. *J Cardiol* (2020) 76(3):227–35. doi:10.1016/j.jcc.2020.04.007
11. Najem MY, Couturaud F, Lemarié CA. Cytokine and chemokine regulation of venous thromboembolism. *J Thromb Haemost* (2020) 18(5):1009–19. doi:10.1111/jth.14759
12. Ding J, Song B, Xie X, Li X, Chen Z, Wang Z, et al. Inflammation in cerebral venous thrombosis. *Front Immunol* (2022) 13:833490. doi:10.3389/fimmu.2022.833490
13. Sodiol EAG. *Cardio embolic stroke: a study of its incidence, etiology, clinical presentation and outcom*. Rajiv Gandhi University of Health Sciences (2017). (India). doi:10.18410/jebmh/2018/584
14. Yang D, Hu J, Zhang M, Chen Y, Xie H, Jin Y, et al. Prediction of trends in unfavorable prognosis in patients with acute ischemic stroke according to low left ventricular ejection fraction levels. *J Cereb Blood Flow and Metab* (2024) 44:1816–26. doi:10.1177/0271678x241247020
15. Lattanzi S, Pulcini A, Corradetti T, Rinaldi C, Zedde ML, Ciliberti G, et al. Prediction of outcome in embolic strokes of undetermined source. *J stroke*

Generative AI statement

The author(s) declare that no Generative AI was used in the creation of this manuscript.

16. Powrozek T, Skwarek-Dzieskanowska A, Sobieszek G, Małacka-Massalska T. Correlation between neutrophil-to-lymphocyte ratio, platelets-to-lymphocyte ratio, C-reactive protein-to-albumin ratio and clinical picture of elderly chronic heart failure patients. *J Clin Med* (2024) 13(2):433. doi:10.3390/jcm13020433
17. Zhou HH, Tang YL, Xu TH, Cheng B. C-reactive protein: structure, function, regulation, and role in clinical diseases. *Front Immunol* (2024) 15:1425168. doi:10.3389/fimmu.2024.1425168
18. Gremese E, Bruno D, Varriano V, Perniola S, Petricca L, Ferraccioli G. Serum albumin levels: a biomarker to be repurposed in different disease settings in clinical practice. *J Clin Med* (2023) 12(18):6017. doi:10.3390/jcm12186017
19. Karabağ Y, Çağdaş M, Rencuzogullari I, Karakoyun S, Artaç İ, İliş D, et al. Relationship between C-reactive protein/albumin ratio and coronary artery disease severity in patients with stable angina pectoris. *J Clin Lab Anal* (2018) 32(7):e22457. doi:10.1002/jcla.22457
20. Yu D, Guo G, Wan F, Hu B. The association between C-reactive protein to albumin ratio and adverse outcomes in acute ischemic stroke patients: a study in the Korean population. *Heliyon* (2024) 10(20):e39212. doi:10.1016/j.heliyon.2024.e39212
21. Li W, Wang Z, Gao M, Wang Y, Ke Y. A study on the relationship between neutrophil-to-lymphocyte ratio (NLR) and platelet-to-lymphocyte ratio (PLR) in neurosurgery and the occurrence and prognosis of progressive hemorrhagic brain injury (PHI) in patients with traumatic brain injury. *Bmc Neurol* (2024) 24(1):484. doi:10.1186/s12883-024-03986-5
22. Chapman NM, Chi H. Metabolic adaptation of lymphocytes in immunity and disease. *Immunity* (2022) 55(1):14–30. doi:10.1016/j.immuni.2021.12.012
23. Martinez Bravo G, Annarapu G, Carmona E, Nawarskas J, Clark R, Novelli E, et al. Platelets in thrombosis and atherosclerosis: a double-edged sword. *Am J Pathol* (2024) 194(9):1608–21. doi:10.1016/j.ajpath.2024.05.010
24. Vakhshoori M, Bondariyan N, Sabouhi S, Kiani K, Alaei Faradonbeh N, Emami SA, et al. The impact of platelet-to-lymphocyte ratio on clinical outcomes in heart failure: a systematic review and meta-analysis. *Ther Adv Cardiovasc Dis* (2024) 18:17539447241227287. doi:10.1177/17539447241227287
25. Zhai G, Wang J, Liu Y, Zhou Y. Platelet-lymphocyte ratio as a new predictor of in-hospital mortality in cardiac intensive care unit patients. *Scientific Rep* (2021) 11(1):23578. doi:10.1038/s41598-021-02686-1
26. Meisinger C, Freuer D, Schmitz T, Ertl M, Zickler P, Naumann M, et al. Inflammation biomarkers in acute ischemic stroke according to different etiologies. *Eur J Neurol* (2024) 31(1):e16006. doi:10.1111/ene.16006
27. Giede-Jeppe A, Madžar D, Sembill JA, Sprügel MI, Atay S, Hoelter P, et al. Increased neutrophil-to-lymphocyte ratio is associated with unfavorable functional outcome in acute ischemic stroke. *Neurocrit Care* (2020) 33:97–104. doi:10.1007/s12028-019-00859-5
28. Zahorec R. Neutrophil-to-lymphocyte ratio, past, present and future perspectives. *Bratislava Med J* (2021) 122(7):474–88. doi:10.4149/bll_2021_078
29. Quan K, Wang A, Zhang X, Meng X, Chen P, Li H, et al. Neutrophil to lymphocyte ratio and adverse clinical outcomes in patients with ischemic stroke. *Ann Translational Med* (2021) 9(13):1047. doi:10.21037/atm-21-710



OPEN ACCESS

*CORRESPONDENCE

Xin Ma,
✉ maxin@xwh.ccmu.edu.cn
Yanning Cai,
✉ caiyanning@xwh.ccmu.edu.cn

†PRESENT ADDRESSES

Yi Yang,
Department of Neurology, Affiliated
Hospital of Jiangsu University,
Zhenjiang, Jiangsu, China

RECEIVED 09 April 2025

ACCEPTED 28 May 2025

PUBLISHED 01 July 2025

CITATION

Zhao X, Yang Y, Du X, Li L, Hou C, Cai Y
and Ma X (2025) Dependence of
mitochondrial dysfunction in peripheral
blood mononuclear cells on
cervicocephalic atherosclerotic burden
in acute ischemic stroke.
Exp. Biol. Med. 250:10624.
doi: 10.3389/ebm.2025.10624

COPYRIGHT

© 2025 Zhao, Yang, Du, Li, Hou, Cai and
Ma. This is an open-access article
distributed under the terms of the
[Creative Commons Attribution License](https://creativecommons.org/licenses/by/4.0/)
(CC BY). The use, distribution or
reproduction in other forums is
permitted, provided the original
author(s) and the copyright owner(s) are
credited and that the original
publication in this journal is cited, in
accordance with accepted academic
practice. No use, distribution or
reproduction is permitted which does
not comply with these terms.

Dependence of mitochondrial dysfunction in peripheral blood mononuclear cells on cervicocephalic atherosclerotic burden in acute ischemic stroke

Xiaoxi Zhao^{1,2}, Yi Yang^{1,2†}, Xiangying Du³, Luguang Li^{1,2},
Chengbei Hou⁴, Yanning Cai^{5,6*} and Xin Ma^{1,2*}

¹Department of Neurology, Xuanwu Hospital, Capital Medical University, Beijing, China, ²National Clinical Research Center for Geriatric Disorders, Beijing, China, ³Department of Radiology, Xuanwu Hospital, Capital Medical University, Beijing, China, ⁴Center for Evidence-Based Medicine, Xuanwu Hospital, Capital Medical University, Beijing, China, ⁵Department of Neurobiology, Xuanwu Hospital, Capital Medical University, Beijing, China, ⁶Department of Clinical Biobank, Xuanwu Hospital, Capital Medical University, Beijing, China

Abstract

As an inflammatory disease, atherosclerosis is associated with acute ischemic stroke (AIS), but its early identification and intervention efficacy remain suboptimal. A new research direction may be to explore peripheral atherosclerotic biomarkers from the perspective of mitochondrial dysfunction, which can induce inflammatory cell activation. Moreover, the degree of overall cervicocephalic atherosclerosis (namely, atherosclerotic burden) is more closely related to AIS prognosis than local atherosclerotic lesions. Therefore, this study investigated the relationship between mitochondrial dysfunction in peripheral blood mononuclear cells (PBMCs), including monocytes and lymphocytes, and overall cervicocephalic atherosclerotic burden and AIS outcome. Patients with AIS and cervicocephalic atherosclerosis were enrolled and followed up for 90 days. The reactive oxygen species (ROS) and the mitochondrial deoxyribonucleic acid copy number (mtDNA-CN) in PBMCs were measured respectively through a fluorescence probe and a droplet digital polymerase chain reaction to evaluate mitochondrial function. The overall intracranial and cervical atherosclerotic burden (ICAB) was quantified by summing up the atherosclerosis degree points in each arterial segment as assessed by computed tomography angiography. A modified Rankin Scale (mRS) score >2 was considered a 90-day unfavorable functional outcome. Five (4.9%) of the 103 patients with AIS were lost to follow-up. mtDNA-CN [adjusted β = -0.099, 95% confidence intervals (CIs) = -0.153 ~ -0.044, p < 0.001] and ROS content (adjusted β = 1.275, 95%CI = 0.885 ~ 1.665, p < 0.001) were correlated with ICAB. The risk of a 90-day unfavorable functional outcome increased with higher ROS content [adjusted odds ratio (OR) = 1.523, 95%CI = 1.172 ~ 1.981, p = 0.002] and decreased with higher mtDNA-CN (adjusted OR = 0.911, 95%CI = 0.850 ~ 0.976, p = 0.008). PBMC mitochondrial dysfunction was found to be independently associated with

extensive and severe cervicocephalic atherosclerosis and a 90-day unfavorable functional outcome in patients with AIS, which may provide a novel approach to improving the early identification and risk stratification of cervicocephalic atherosclerosis, along with the prediction of the outcome of atherosclerotic AIS.

KEYWORDS

atherosclerosis, mitochondrial deoxyribonucleic acid copy number, reactive oxygen species, peripheral blood mononuclear cells, acute ischemic stroke

Impact statement

As a chronic progressive inflammatory disease, atherosclerosis is a primary etiology of acute ischemic stroke (AIS), but its early identification and intervention efficacy remain suboptimal. It may be a breakthrough to explore peripheral atherosclerotic biomarkers from the perspective of inflammatory cells mitochondrial dysfunction. Moreover, the overall cervicocephalic atherosclerosis degree is more closely related to AIS prognosis than the presence of local atherosclerotic lesion. Thus, we investigated the relationship between peripheral blood mononuclear cells (PBMC) mitochondrial dysfunction (mitochondrial deoxyribonucleic acid copy number reduction and reactive oxygen species overexpression) and intracranial and cervical atherosclerotic burden (ICAB). PBMC mitochondrial dysfunction was found to be independently associated with extensive and severe cervicocephalic atherosclerosis (high ICAB) and poor short-term functional outcome in AIS patients with cervicocephalic atherosclerosis. These findings may provide a feasible new approach to improve the identification and risk stratification of total cervicocephalic atherosclerosis degree and functional prognosis prediction of atherosclerotic AIS patients.

Introduction

Atherosclerosis is the primary cause of acute ischemic stroke (AIS) [1] and is closely correlated with AIS prognosis [2, 3], necessitating the early identification of the atherosclerosis degree for timely and appropriate prevention and treatment. Despite the existence of various risk factors and biomarkers, the efficacy of early identification and intervention of atherosclerosis has not been optimal [4]. This highlights the clinical need to explore specific and easily accessible biomarkers associated with atherosclerosis from a novel perspective, to improve risk stratification and facilitate early prevention and treatment.

The initiation and progression of atherosclerosis are associated with cell death, oxidative metabolism, inflammatory cell activation state, and mitochondrial dysfunction [5–8]. Mitochondrial dysfunction is commonly reflected by a reduction in mitochondrial deoxyribonucleic acid copy

number (mtDNA-CN) and an overexpression of reactive oxygen species (ROS) in clinical research [9–16]. It has been reported that there is less mtDNA-CN and more ROS content in aortic and carotid atherosclerotic plaques compared to normal artery walls [17, 18]. However, assessing mitochondrial function in plaque is difficult in clinical settings because of the invasive nature of obtaining plaque by endarterectomy. Monocytes and lymphocytes, collectively referred to as peripheral blood mononuclear cells (PBMCs), are the major inflammatory cells involved in atherosclerosis [1], and they can be easily isolated from peripheral blood. A previous study suggested that mitochondrial dysfunction in peripheral blood inflammatory cells may correspond to that in atherosclerotic plaques [19]. However, there is still a lack of studies on the correlation between PBMC mitochondrial dysfunction and cervicocephalic atherosclerosis. Moreover, because of the systemic nature of atherosclerosis, local atherosclerotic plaque or single-artery stenosis does not accurately reflect the overall degree of atherosclerosis. Thus, further investigation is needed to explore the relationship between PBMC mitochondrial dysfunction and the overall degree of cervicocephalic atherosclerosis. In addition, previous studies have shown that lower mtDNA-CN is associated with a poor prognosis for stroke patients (including those with ischemic and hemorrhagic stroke) [15], but there are currently no related studies on mtDNA-CN or ROS content in PBMCs and functional outcomes in ischemic stroke patients, especially those with cervicocephalic atherosclerosis.

In previous studies, real-time quantitative polymerase chain reaction (qPCR) was used to detect mtDNA-CN [20–22]. Droplet digital polymerase chain reaction (ddPCR) is a new method developed in recent years that has the characteristics of absolute quantification and accurate analysis [23], and is superior to previous methods. In this study, ddPCR was used for the first time to measure mtDNA-CN in PBMCs and investigate its relationship with cervicocephalic atherosclerosis. ROS content is usually determined using a fluorescent probe. In addition, intracranial and cervical atherosclerotic burden (ICAB), as a new atherosclerosis assessment index, can quantify the degree and extent of cervicocephalic atherosclerosis as a whole. Our recent study showed that this indicator has a stronger vascular risk stratification value than regional atherosclerosis assessment [24]. In this study, mtDNA-CN, ROS content, ICAB and a modified Rankin Scale (mRS) were used to investigate the correlation between

PBMC mitochondrial dysfunction and the overall degree of cervicocephalic atherosclerosis, along with the poor short-term functional prognosis of patients with AIS, in order to provide a new way for improving the early identification and risk stratification of cervicocephalic atherosclerosis in addition to the functional prognosis prediction of patients with AIS with cervicocephalic atherosclerosis.

Materials and methods

Study population

This single-center, prospective cohort study was performed in accordance with the Declaration of Helsinki, and was approved by the Ethics Committee of Xuanwu Hospital, Capital Medical University (Beijing, China) [approval number (2022)008, 26 January 2022]. All patients gave their informed consent before inclusion. Patients admitted to the cerebral vascular disease unit of the Department of Neurology at Xuanwu Hospital, Capital Medical University from 01 February 2022 to 30 April 2022 were consecutively enrolled.

The inclusion criteria were as follows: (1) at least 18 years old; (2) first-ever AIS confirmed by computed tomography or magnetic resonance imaging; (3) within 7 days after onset of symptoms; (4) undertook computed tomography angiography (CTA) successfully; and (5) AIS subtypes of large-artery atherosclerosis (LAA) and small-artery occlusion (SAO) with cervicocephalic atherosclerosis [25].

The exclusion criteria included: (1) a history of hemorrhagic stroke or subarachnoid hemorrhage; (2) symptomatic atherosclerotic coronary artery disease; (3) infection or chronic inflammatory disease (temperature $\geq 37.3^{\circ}\text{C}$, number of leukocytes $>12 \times 10^9/\text{L}$ or $<4 \times 10^9/\text{L}$, use of anti-inflammatory drugs or antibiotics); (4) immunodeficiency or use of immunosuppressants; (5) mitochondrial myopathy or mitochondrial encephalomyopathy; (6) poor organ function; (7) hematological system diseases; and (8) malignant tumors.

General characteristics

The patients' age, sex, history of hypertension, diabetes mellitus, hyperlipidemia history, smoking history, and alcohol consumption were collected through interviews. Smoking was defined as having smoked within the last 12 months. Neurological deficit severity was estimated according to the National Institutes of Health Stroke Scale (NIHSS) upon admission [26]. Blood samples from all the enrolled patients were subjected to complete blood counts, biochemical tests, and coagulation function assays. Medical treatment during hospitalization was in accordance with AIS management and secondary prevention guidelines [27].

Measurement of ROS content by fluorescence spectroscopy

In total, 10 mL of fasting venous blood was collected from each patient within 24 h after admission. PBMCs were isolated by density gradient centrifugation using Ficoll-Paque PLUS (17144002, Cytiva, Marlborough, MA, United States) within 2 hours of the blood sample being taken. The ROS content was then measured within 4 h by fluorescence spectroscopy. The PBMCs of each patient were resuspended in 500 μL of D-PBM buffer (201050, PBM, Tianjin, China) and then divided into a background tube and a stained tube. There were approximately 1×10^6 PBMCs per tube. CellROX Green (C10444, Invitrogen, Carlsbad, CA, United States) was added to the stained tube to reach a final concentration of 5 μM . The two tubes were then incubated in a water bath at 37°C for 30 min, and the twice-washed PBMCs were placed in a 96-microwell plate (137101, Thermo Scientific, Waltham, MA, United States). The wells were defined as follows: negative well (100 μL D-PBS buffer), background well (100 μL unstained cell suspension), and stained well (100 μL stained cell suspension), respectively. Finally, a microplate reader (Varioskan Flash Multimode Reader, Thermo Scientific, Waltham, MA, United States) and SkanIt Software 2.4.5 were used to detect fluorescence intensity (FI) by fluorometry (excitation/emission: 485/520 nm), and the ROS content was then calculated using Equation 1:

$$\text{ROS content} = \left(\text{FI}_{\text{stained}} - \text{FI}_{\text{background}} \right) / \text{FI}_{\text{negative}} \quad (1)$$

Determination of mtDNA-CN by ddPCR

After isolating the PBMCs, an animal mtDNA column extraction kit (BTN80803, Beijing BioRab Technology, Beijing, China) was used to isolate the mtDNA. The mitochondrially encoded NADH dehydrogenase 1 (ND1) gene is located in the mitochondrial membrane, and the ribonuclease P/MRP 30 kDa subunit (RPP30) gene is a cellular housekeeping gene of the nucleus. ddPCR was used in separate reactions to measure the copy number of the mitochondrial ND1 gene (ND1-CN) and the nuclear RPP30 gene copy number (RPP30-CN). The mtDNA-CN quantification was calculated using Equation 2:

$$\text{mtDNA-CN} = \text{ND1-CN/RPP30-CN} \quad (2)$$

Amplification of the target DNA was performed in a 20 μL reaction mixture sample containing a ddPCR premixture (10 μL), mtDNA (1 μL), the restriction enzyme Hind III (0.3 μL), nuclease-free water (6.65 μL), a forward primer (0.9 μL), a reverse primer (0.9 μL), and a probe (0.25 μL). The sample was loaded into droplet generator (MicroDrop-100A, Forevergen, Guangzhou, Guangdong, China) to convert it into a water-in-oil droplet emulsion. The thermal cycling conditions consisted of a 10 min pre-denaturation at 95°C followed by 45 cycles of a 30 s denaturation

at 95°C, a 1 min annealing-extension at 58°C for the ND1 reaction and at 61°C for the RPP30 reaction, a 10 min inactivation at 98°C, and a 4°C holding period. Finally, the amplified sample was analyzed using biochip analyzer (MicroDrop-100B, Forevergen, Guangzhou, Guangdong, China). The ND1-CN and RPP30-CN values were calculated using the QuantDrop system. The results were considered reliable when the number of droplets was >40,000.

The ND1 primers and probe used in this work were as follows:

forward primer, 5'-CCCTAAAACCCGCCACATCT-3';
reverse primer, 5'-GAGCGATGGTGAGAGCTAAGGT-3';
probe, 5'-VIC/CCATCACCTCTACATCACCGCCC/DBQ1-3'.

The following RPP30 primers and probe were considered:

forward primer, 5'-AGATTGGACCTGCGAGCG-3';
reverse primer, 5'-GAGCGGCTGTCTCCACAAGT-3';
probe, 5'-FAM/TTCTGACCTGAAGGCTCTGCGCG/BHQ1-3'.

Quantification of the overall degree of atherosclerosis in cervicocephalic arteries using CTA

The CTA scan mode and the segments of cervicocephalic arteries described in our previous study were adopted in the present work [24]. Images of the cervicocephalic arteries were reconstructed and reviewed independently by two experienced radiologists who were unaware of the patients' demographic and clinical information. Any discrepancies were discussed until a consensus was reached.

The degree of stenosis in the cervical arteries was evaluated based on the North American Symptomatic Carotid Endarterectomy Trial [28], and that in the intracranial arteries was evaluated based on the Warfarin-Aspirin Symptomatic Intracranial Disease Study [29]. The cervicocephalic arteries were divided into 19 segments as follows: 18 segments (9 bilateral arteries, including the subclavian, common carotid, extracranial carotid, extracranial vertebral, intracranial carotid, intracranial vertebral, posterior cerebral, middle cerebral and anterior cerebral arteries), plus one single segment (the basilar artery) [30]. We scored the most severe atherosclerotic lesion in each segment as follows: 0 points (no atherosclerotic lesion), 1 point (<50% stenosis or atherosclerotic plaque with no stenosis), 2 points (50%–69% stenosis), 3 points (70%–99% stenosis), and 4 points (occlusion), respectively [24]. ICAB was calculated by summing the points of each segment.

Follow-up

All patients were followed up at 90 days after the onset of AIS via telephone interview with the patients or their long-term caregivers by an experienced physician who was blinded to

the baseline data. The mRS was used to evaluate the post-stroke disability [31].

Grouping of study subjects

ROS content, ICAB, and mtDNA-CN were divided into low, median, and high groups based on tertiles. In addition, ROS content was also classified as low or high according to the median. An unfavorable functional outcome was defined as an mRS >2, while a favorable functional outcome was defined as an mRS ≤2.

Statistical analysis

The experimental data are presented as the mean ± standard deviation for normally distributed continuous variables, as the median (interquartile range) for non-normally distributed continuous variables, and as the count (%) for categorical variables. Continuous variables were compared using a Student's t-test or a Mann-Whitney U test between two groups as appropriate, and using a one-way analysis of variance or a Kruskal-Wallis test with Bonferroni's correction between three groups. Categorical variables were compared using a Chi-squared test or Fisher's exact test.

Spearman's correlation analysis was used to evaluate the correlation of mtDNA-CN and ROS content with ICAB, as well as that of mtDNA-CN with ROS content. For further exploration, the correlation of mtDNA-CN and ROS content with ICAB was assessed by multivariable linear regression analysis. The relationships between mitochondrial function (mtDNA-CN and ROS content) and ICAB were evaluated using Spearman's correlation and multivariable linear regression. The relationship between mtDNA-CN and ROS content was assessed using Spearman's correlation and multivariable logistic regression. Additionally, multivariable logistic regression was also used to examine the associations of mitochondrial function (mtDNA-CN and ROS content) and ICAB with 90-day unfavorable functional outcome (mRS >2). All tests were two-sided, and $p < 0.05$ was considered statistically significant. The statistical analyses were performed using SPSS Statistics (version 25.0; IBM, Armonk, NY, United States), and GraphPad Prism (version 8.0) was used for the preparation of figures.

Results

Of the 115 participants with AIS without symptomatic atherosclerotic coronary artery disease, the following patients were excluded: those who refused to participate ($n = 3$), those with incomplete CTA ($n = 4$), those with Moyamoya disease ($n =$

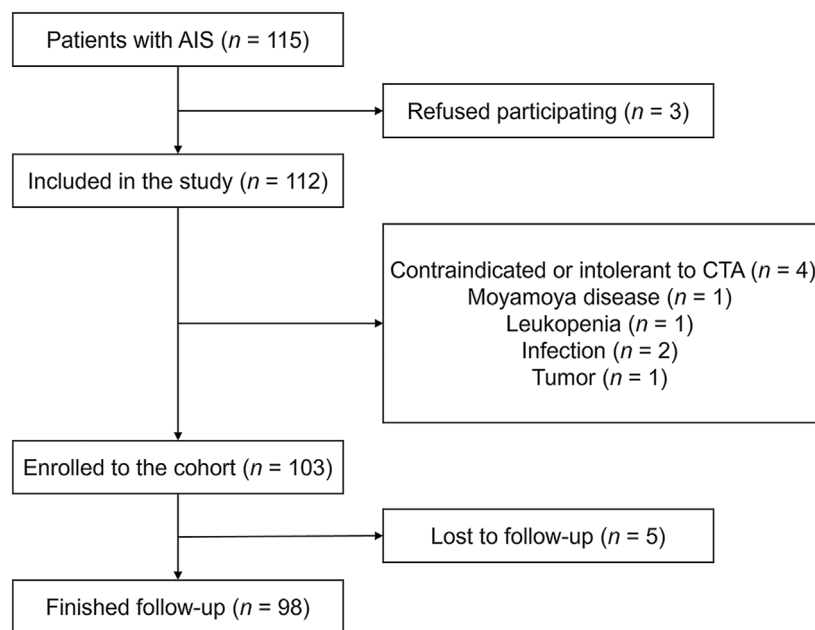


FIGURE 1

Flowchart of patients' enrollment and follow-up. Abbreviations: AIS, acute ischemic stroke; CTA, computed tomography angiography.

1), those with leukopenia ($n = 1$), those with infection ($n = 2$), and those with a tumor ($n = 1$). Thus, there was a total of 103 patients enrolled in our cohort. Among them, 5 (4.9%) patients were lost to follow-up, and the study finished with 98 patients with complete information on mRS 90 days after ischemic stroke (Figure 1).

Baseline characteristics and 90-day functional outcomes

Among the 98 patients who completed the 90-day follow-up, the mean age was 60.8 ± 11.5 years, and 67 patients (68.4%) were men. The median ICAB was 14 (range 7–20) points, and the median baseline mRS was 1 (range 0–3) point. The PBMC mitochondrial function was indicated by a median mtDNA-CN of 24.32 (range 13.27–37.97) $\times 10^2$ and a median ROS content of 5.71 (range 3.88–8.50) in the 98 patients, with no differences compared to patients lost to follow-up ($p = 0.256$, $p = 0.914$) (Supplementary Table S1). Patients in the high ICAB group (ICAB >18 points) had lower mtDNA-CN ($p < 0.05$) and higher ROS content ($p < 0.05$) than those in the low ICAB group (ICAB <10 points) (Table 1). At the end of the 90-day follow-up period, 24 patients (24.5%) had an unfavorable functional outcome (mRS >2) (Supplementary Table S2).

The kappa value for inter-rater reliability in ICAB was 0.929 ($p < 0.001$).

Relationship between PBMC mitochondrial dysfunction and ICAB

It is clear from Figure 2 that ICAB was found to be higher in each group with severe PBMC mitochondrial dysfunction (low mtDNA-CN $<18.08 \times 10^2$, high ROS content >7.85). Spearman's correlation analysis showed a negative correlation between mtDNA-CN and ICAB ($r = -0.39$, $p < 0.001$) (Figure 3A), and a positive correlation between ROS content and ICAB ($r = 0.58$, $p < 0.001$) (Figure 3B). After adjusting for age, sex, PBMC count, and the parameters with $p < 0.1$ in univariable analysis (Supplementary Table S3), mtDNA-CN was found to be independently and negatively associated with ICAB (adjusted $\beta = -0.099$, 95%CI = $-0.153 \sim -0.044$, $p < 0.001$), and ROS content was also positively associated independently with ICAB (adjusted $\beta = 1.275$, 95%CI = $0.885 \sim 1.665$, $p < 0.001$) in multivariable linear regression analysis (Table 2).

Relationship between mtDNA-CN and ROS content

Figure 4 shows the significant negative correlation between mtDNA-CN and ROS content in PBMCs in a Spearman's correlation analysis ($r = -0.38$, $p < 0.001$). After adjusting for age, sex, diabetes history, and alcohol consumption in

TABLE 1 Comparison of baseline characteristics of patients in low, median, and high ICAB groups.

Variables	Low ICAB (<i>n</i> = 34)	Median ICAB (<i>n</i> = 32)	High ICAB (<i>n</i> = 32)	<i>p</i> value
Demographics				
Age (years)	58.2 ± 13.5	64.8 ± 11.0	59.6 ± 8.58	0.050
Male patients (<i>n</i>)	20 (58.8) ^a	19 (59.4) ^a	28 (87.5)	0.018 ^b
Clinical characteristics				
NIHSS (points)	1 (0–2)	1 (0–3)	3 (1–5)	0.028 ^b
mRS (points)	1 (0–2) ^a	0 (0–3) ^a	3 (1–3)	0.013 ^b
ICAB (points)	4 (1–7) ^{a, c}	15 (11–16) ^a	23 (20–25)	<0.001 ^b
BMI (kg/m ²)	26.01 ± 4.89	26.28 ± 3.61	26.05 ± 4.02	0.961
SBP (mmHg)	139.4 ± 22.1	138.2 ± 21.6	144.7 ± 18.6	0.421
DBP (mmHg)	87.8 ± 13.1	82.0 ± 11.1	89.0 ± 12.5	0.052
HbA1c (%)	5.60 (5.30–5.95) ^a	5.90 (5.40–7.48)	6.25 (5.50–7.88)	0.044 ^b
FBG (mmol/L)	4.87 (4.24–5.36) ^a	5.26 (4.46–6.83)	5.92 (5.09–7.60)	0.001 ^b
TC (mmol/L)	4.04 ± 1.05	4.21 ± 1.56	4.31 ± 1.26	0.363
TG (mmol/L)	1.23 (0.86–1.89)	1.42 (1.18–1.69)	1.52 (1.24–2.13)	0.067
LDL-C (mmol/L)	1.98 (1.76–2.96)	2.21 (1.42–2.90)	2.53 (1.69–3.35)	0.438
HDL-C (mmol/L)	1.17 ± 0.28 ^a	1.12 ± 0.28 ^a	0.96 ± 0.25	0.007 ^b
Hcy (μmol/L)	16.94 (11.08–18.38)	16.29 (13.18–18.23)	14.95 (11.05–17.31)	0.394
UA (mmol/L)	316.41 ± 96.86	300.47 ± 87.54	322.66 ± 88.93	0.606
hs-CRP (mg/L)	1.50 (0.68–4.38)	1.37 (0.57–5.07)	3.68 (0.75–5.13)	0.462
FIB (g/L)	3.02 ± 0.78	3.12 ± 1.02	3.54 ± 0.98	0.690
D-Dimer (mmol/L)	0.26 (0.20–0.49)	0.26 (0.21–0.36)	0.25 (0.14–0.34)	0.547
Risk factors				
History of hypertension (<i>n</i>)	20 (58.8)	23 (71.9)	26 (81.3)	0.133
History of diabetes (<i>n</i>)	4 (11.8)	10 (31.3)	11 (34.4)	0.072
History of hyperlipidemia (<i>n</i>)	15 (44.1)	12 (37.5)	15 (46.9)	0.738
Smoking history (<i>n</i>)	10 (29.4)	11 (34.4)	18 (56.3)	0.063
Alcohol consumption (<i>n</i>)	8 (23.5)	11 (34.4)	16 (50.0)	0.079
PBMC characteristics				
PBMC count (×10 ⁹ /L)	2.29 ± 0.96	2.48 ± 0.66	2.37 ± 0.98	0.334
mtDNA-CN (×10 ²)	32.61 (23.33–50.94) ^a	28.28 (14.28–40.89) ^a	12.61 (6.02–21.65)	<0.001 ^b
ROS content	4.09 (2.75–5.10) ^{a, c}	7.16 (4.94–8.14)	8.75 (5.06–12.18)	<0.001 ^b

Data presented as mean ± standard deviation, median (interquartile range), or *n* (%). ICAB was grouped by tertile: low ICAB <10 points, median ICAB = 10 ~ 18 points, and high ICAB >18 points.

Abbreviations: ICAB, intracranial and cervical atherosclerotic burden; NIHSS, national institute of health stroke scale; mRS, modified Rankin Scale; BMI, body mass index; SBP, systolic blood pressure; DBP, diastolic blood pressure; HbA1c, glycated hemoglobin; FBG, fasting blood glucose; TC, total cholesterol; TG, triglyceride; LDL-C, low-density lipoprotein cholesterol; HDL-C, high-density lipoprotein cholesterol; Hcy, homocysteine; UA, serum uric acid; hs-CRP, hypersensitive C-reactive protein; FIB, fibrinogen; PBMC, peripheral blood mononuclear cells; mtDNA-CN, mitochondrial deoxyribonucleic acid copy number; ROS, reactive oxygen species.

^a*p* < 0.05 compared with the high ICAB group.

^bStatistically significant differences (*p* value < 0.05).

^c*p* < 0.05 compared with the median ICAB group.

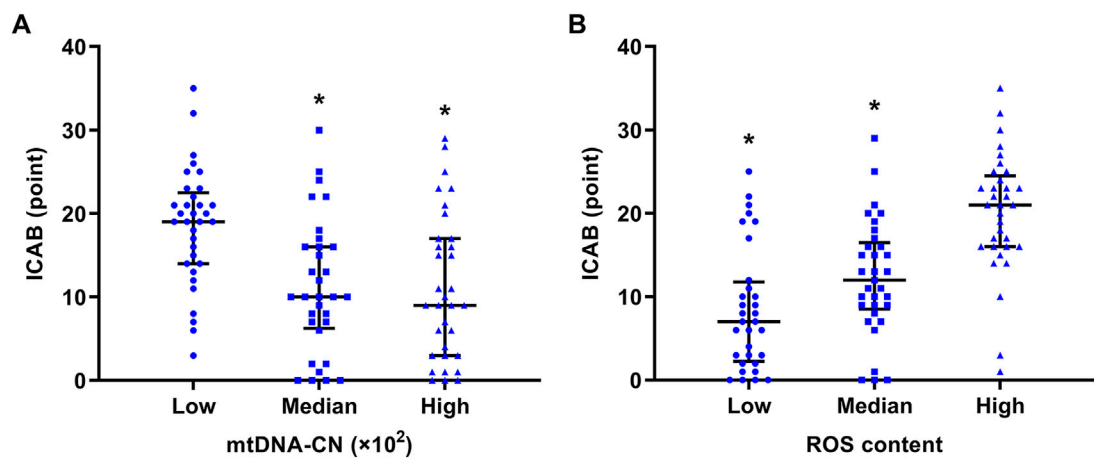


FIGURE 2 Comparison of ICAB between different groups of mtDNA-CN and ROS content. **(A)** ICAB of the low mtDNA-CN group was significantly higher than that of the median and high mtDNA-CN groups. The mtDNA-CN was grouped by tertile: low mtDNA-CN < 18.08 ×10², median mtDNA-CN = (18.08 ~ 32.83) ×10², high mtDNA-CN >32.83 ×10². **p* < 0.001 vs. the low mtDNA-CN group. **(B)** ICAB of the high ROS content group was significantly higher than that of the low and median ROS content groups. ROS content was grouped by tertile: low ROS content <4.64, median ROS content = 4.64 ~ 7.85, high ROS content >7.85. **p* < 0.001 vs. the high ROS content group. ICAB is represented as the median (interquartile range). Abbreviations: ICAB, intracranial and cervical atherosclerotic burden; mtDNA-CN, mitochondrial deoxyribonucleic acid copy number; ROS, reactive oxygen species.

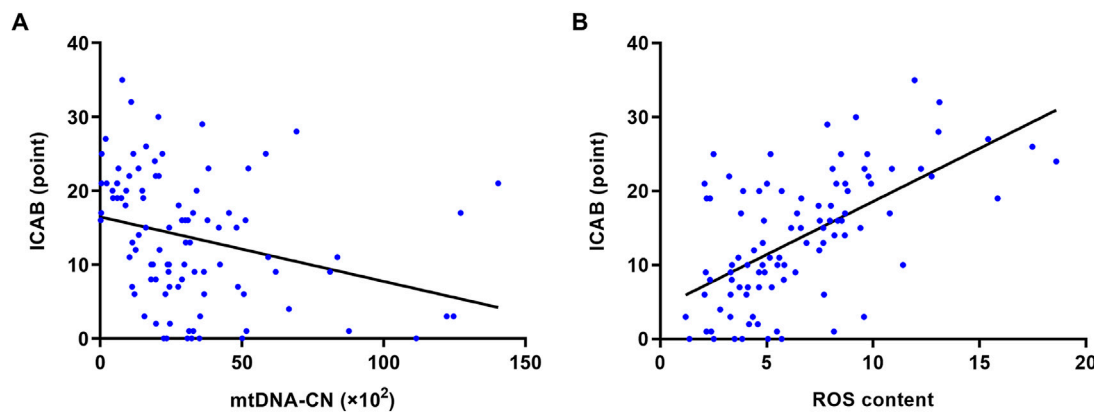


FIGURE 3 Spearman's correlation analysis of mtDNA-CN, ROS content and ICAB. **(A)** Correlation between mtDNA-CN and ICAB (*r* = −0.39, *p* < 0.001). **(B)** Correlation between ROS content and ICAB (*r* = 0.58, *p* < 0.001). Abbreviations: ICAB, intracranial and cervical atherosclerotic burden; mtDNA-CN, mitochondrial deoxyribonucleic acid copy number; ROS, reactive oxygen species.

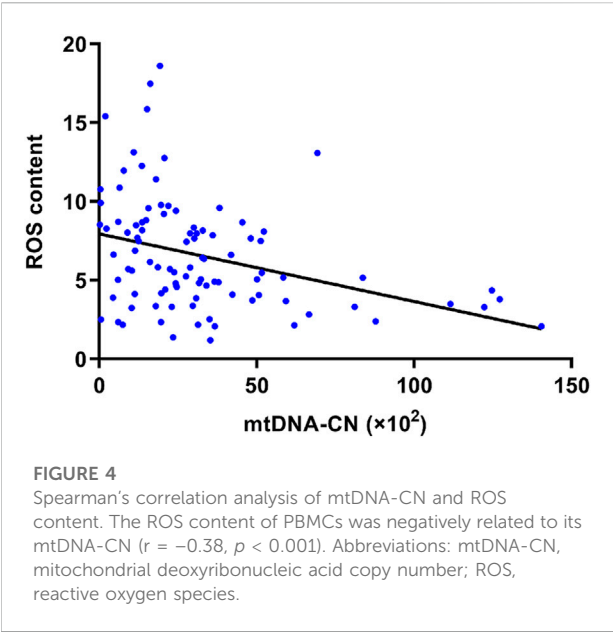
TABLE 2 Multivariable linear regression of mtDNA-CN, ROS content and ICAB.

PBMC mitochondrial function	ICAB		
	β (95%CI) ^a	<i>p</i> value	R ²
mtDNA-CN	−0.099 (−0.153 ~ −0.044)	<0.001 ^b	0.413
ROS content	1.275 (0.885–1.665)	<0.001 ^b	0.549

^aAdjusted for age, sex, history of hypertension, history of diabetes, alcohol consumption, glycated hemoglobin, fasting blood glucose, triglyceride, high-density lipoprotein cholesterol, fibrinogen, and PBMC count.

Abbreviations: ICAB, intracranial and cervical atherosclerotic burden; mtDNA-CN, mitochondrial deoxyribonucleic acid copy number; ROS, reactive oxygen species; CI, confidence interval.

^bStatistically significant differences (*p* value < 0.05).



multivariable logistic regression, the risk of high ROS content decreased with elevated mtDNA-CN (adjusted OR = 0.959, 95% CI = 0.933–0.986, $p = 0.003$) (Table 3; Supplementary Table S4).

Relationship between ICAB and a 90-day functional outcome of AIS

Compared to patients with a favorable functional outcome, those with an unfavorable functional outcome (90-day mRS >2) had higher levels of low-density lipoprotein cholesterol ($p = 0.033$), NIHSS ($p < 0.001$), ICAB ($p < 0.001$), and ROS content ($p = 0.010$), but lower levels of mtDNA-CN ($p = 0.001$) (Supplementary Table S2). Multivariable logistic regression analysis revealed that ICAB was independently related to a 90-day unfavorable functional outcome after adjusting for age, sex, PBMC count, total cholesterol, low-density lipoprotein cholesterol, and NIHSS (adjusted OR = 1.127, 95%CI = 1.021–1.244, $p = 0.018$) (Table 4; Supplementary Table S5).

Relationship between PBMC mitochondrial dysfunction and a 90-day functional outcome of AIS

Multivariable logistic regression analysis showed that after adjusting for age, sex, PBMC count, total cholesterol, low-density lipoprotein cholesterol, and NIHSS, patients with higher mtDNA-CN had a decreased risk of a 90-day unfavorable functional outcome (adjusted OR = 0.911, 95%CI = 0.850–0.976, $p = 0.008$), while patients with higher ROS content had an increased risk of 90-day unfavorable functional outcome (adjusted OR = 1.523, 95%CI = 1.172 ~ 1.981, $p = 0.002$) (Table 4; Supplementary Table S5).

Discussion

In this study, we found that mtDNA-CN and ROS content of PBMCs were negatively and positively correlated with ICAB, respectively. With the increase of the mtDNA-CN level, the ROS content and the risk of mRS >2 decreased significantly. To our knowledge, this is the first study to suggest that severe PBMC mitochondrial dysfunction is associated with extensive and severe cervicocephalic atherosclerosis, in addition to increased risk of short-term unfavorable functional outcomes in patients with AIS.

Mitochondrial dysfunction may be involved in atherogenesis and has been found in local carotid plaque [18, 32]. Another study of 11 participants revealed decreased mtDNA-CN in coronary artery plaques and a reduction in peripheral blood leukocytes [19], indicating that mitochondrial dysfunction in peripheral blood inflammatory cells could correspond to that in atherosclerotic plaques. mtDNA damage in PBMC has also been reported to be more significant in patients with atherosclerotic cardiovascular disease than in controls without atherosclerosis [33]. Similarly, our study confirmed that the mtDNA-CN of PBMCs was closely related to cervicocephalic atherosclerosis. Thus, it is possible to speculate that similar to the mitochondrial dysfunction observed in plaques, mitochondrial dysfunction in peripheral blood inflammatory cells may also correlate with atherosclerosis. It is also worth noting that mice with mtDNA damage or greater oxidative stress in peripheral blood inflammatory cells were

TABLE 3 Logistic regression analysis of mtDNA-CN and high ROS content.

Variable	High ROS content			
	Univariable analysis		Multivariable analysis	
	OR (95%CI)	<i>p</i> value	Adjusted OR (95%CI) ^a	<i>p</i> value
mtDNA-CN (per 1 × 10 ² increased)	0.961 (0.939–0.984)	0.001 ^b	0.959 (0.933–0.986)	0.003 ^b

^aAdjusted for age, sex, history of diabetes, and alcohol consumption.
ROS content was grouped by the median, with high ROS content ≥5.71.
Abbreviations: mtDNA-CN, mitochondrial deoxyribonucleic acid copy number; ROS, reactive oxygen species; OR, odds ratio; CI, confidence interval.
^bStatistically significant differences (p value < 0.05).

TABLE 4 Logistic regression analysis of ICAB, mtDNA-CN, ROS content, and 90-day unfavorable functional outcome.

Variables	90-day unfavorable functional outcome			
	Univariable analysis		Multivariable analysis	
	Or (95%CI)	p value	Adjusted OR (95%CI) ^a	p value
ICAB (per point increased)	1.115 (1.045 ~ 1.190)	0.001 ^b	1.127 (1.021 ~ 1.244)	0.018 ^b
mtDNA-CN (per 1 × 10 ² increased)	0.953 (0.921 ~ 0.987)	0.006 ^b	0.911 (0.850 ~ 0.976)	0.008 ^b
ROS content (per level increased)	1.265 (1.097 ~ 1.459)	0.001 ^b	1.523 (1.172 ~ 1.981)	0.002 ^b

^aAdjusted for age, sex, PBMC, count, total cholesterol, low-density lipoprotein cholesterol, and NIHSS.
A 90-day unfavorable functional outcome was defined as mRS >2 points.
Abbreviations: ICAB, intracranial and cervical atherosclerotic burden; mtDNA-CN, mitochondrial deoxyribonucleic acid copy number; ROS, reactive oxygen species; OR, odds ratio; CI, confidence interval.
^bStatistically significant differences (*p* value < 0.05).

reported to have larger aortic atherosclerotic plaques than those without [32, 34], showing the aggravating role of mitochondrial dysfunction in the progression of local atherosclerosis. However local atherosclerosis may not accurately reflect the overall degree of atherosclerosis. The impact of mitochondrial dysfunction on overall atherosclerosis needs to be further explored. The relationship between mtDNA-CN in peripheral blood cells and the total degree of atherosclerosis has only been observed in coronary arteries, with inconsistent results and without ROS content assessment [20, 21]. Furthermore, compared to coronary arteries and aortic arteries, cervicocephalic arteries provide a wider range of blood supply with a longer arterial course. Thus, the association, especially between mitochondrial dysfunction in peripheral blood inflammatory cells and the overall degree of cervicocephalic atherosclerosis (ICAB) warrants further investigation. Our findings demonstrated that patients with AIS with severe PBMC mitochondrial dysfunction (lower mtDNA-CN and higher ROS content) are at a higher risk for an extensive and severe degree of overall cervicocephalic atherosclerosis (higher ICAB) (Table 2). Therefore, assessing PBMC mitochondrial dysfunction has potential value in risk stratification for cervicocephalic atherosclerosis in clinical work.

The mitochondrial dysfunction of PBMCs in patients with AIS was evaluated in our study from the perspectives of gene expression and oxidative metabolism, as indicated by mtDNA-CN and ROS content. We found that ROS content gradually increased as mtDNA-CN in PBMCs decreased (Figure 4), suggesting that mtDNA damage and oxidative metabolic injury may not be independent of each other in the presence of atherosclerosis. It should be emphasized that mtDNA lacks histone protection and effective mtDNA repair, and is close to the electron transport chain where ROS are generated [35]. As a result, mtDNA is easy to be damaged by ROS and oxidative stress. Increased ROS content in inflammatory cells may also lead to a decrease in mtDNA-CN, which in turn may lead to a decline in respiratory chain function, an imbalance in cellular oxidative metabolism, and the promotion of further ROS production, thus forming a vicious cycle [36].

Therefore, the decrease in mtDNA-CN and the increase in ROS content in PBMCs are likely to promote each other and may aggravate atherosclerosis. This finding provides some clues for further exploration of the possible mechanisms underlying PBMC mitochondrial dysfunction in patients with AIS with cervicocephalic atherosclerosis.

Previous studies have shown that lower mtDNA-CN in peripheral blood leukocytes can predict poorer outcomes in stroke patients [15]. We conducted this study especially with patients with AIS with LAA and SAO subtypes, so as to better observe the relationship between mitochondrial dysfunction and the prognosis of patients with AIS with cervicocephalic atherosclerosis. Our results showed that both the decrease of mtDNA-CN and the increase of ROS content in PBMCs were independently associated with a 90-day unfavorable functional outcome after AIS (Table 4). Except for the poor outcomes caused by severe atherosclerosis in the cervicocephalic arteries [2, 3, 24], the association between PBMC mitochondrial dysfunction and the functional outcomes of AIS may also involve other possible mechanisms unrelated to atherosclerosis. The mtDNA-CN of peripheral blood leukocytes and other types of cells, such as neurons and endothelial cells may exhibit similar trends of change, and adequate mtDNA-CN in these cells could enhance the repair ability of neurons and the blood-brain barrier after stroke [15]. In addition, low mtDNA-CN may increase the proportion of pro-inflammatory macrophages [9], resulting in the release of more inflammatory factors that exacerbate neuronal damage [37]. Moreover, the increased ROS content could promote endothelial cell injury and apoptosis, in addition to glucose metabolism dysfunction [7, 38–40]. These cellular and tissue damages might affect the functional recovery of patients with AIS, and these potential mechanisms need further exploration.

Finally, it must be mentioned that our study has certain limitations. (i) As a single-center study with a relatively small sample size, the results of this study should be generalized to other populations with caution. (ii) The majority of patients with AIS in this study exhibited mild neurological deficits, and further

research should include patients with different degrees of neurological impairment for a more comprehensive analysis. (iii) While PBMC mitochondrial function and the majority of the clinical characteristics did not differ between patients with and without a completed follow-up, the lower ICAB scores observed in the latter group may indicate the potential bias. Further studies with a larger sample size are needed to reduce this bias. (iv) In addition to functional outcomes, we will continue to follow up on further cardio-cerebral vascular events in patients with AIS to comprehensively investigate the correlation between PBMC mitochondrial dysfunction and poor AIS outcomes. (v) To explore the mechanism by which PBMC mitochondrial dysfunction drives the development of the degree of atherosclerosis, interventional experiments such as oxidative stress inhibition assays should also be conducted.

Conclusion

In summary, this study demonstrated that PBMC mitochondrial dysfunction may play an important role in indicating the extensive and severe overall cervicocephalic atherosclerotic burden and a poor short-term functional outcome of patients with AIS. Given the advantages of the convenient and non-invasive approach to measuring PBMC mitochondrial dysfunction, this study may provide a novel and feasible way to optimize the early identification and risk stratification of cervicocephalic atherosclerosis and functional prognosis prediction of patients with AIS with cervicocephalic atherosclerosis. Further investigation is needed to understand the complex mechanisms between mitochondrial dysfunction in peripheral blood inflammatory cells and atherosclerosis.

Author contributions

XZ: Investigation, Data curation, Formal analysis, Visualization, Writing – original draft preparation. YY: Investigation, Data curation, Writing – original draft preparation. XD: Validation, Resources, Writing – review and editing. LL: Investigation, Writing – original draft preparation. CH: Formal analysis, Writing – review and editing. YC: Methodology, Supervision, Validation, Resources, Writing – review and editing. XM: Conceptualization, Methodology, Supervision, Project administration, Funding acquisition, Writing – review and editing. All authors contributed to the article and approved the submitted version.

References

1. Libby P, Buring JE, Badimon L, Hansson GK, Deanfield J, Bittencourt MS, et al. Atherosclerosis. *Nat Rev Dis Primers* (2019) 5:56. doi:10.1038/s41572-019-0106-z

Data availability

The original contributions presented in the study are included in the article/[Supplementary Material](#), further inquiries can be directed to the corresponding authors.

Ethics statement

The studies involving humans were approved by the Ethics Committee of Xuanwu Hospital of Capital Medical University. The studies were conducted in accordance with the local legislation and institutional requirements. The participants provided their written informed consent to participate in this study.

Funding

The author(s) declare that financial support was received for the research and/or publication of this article. This work was supported by the Natural Science Foundation of Beijing Municipality (grant number 7212049).

Acknowledgments

The authors thank the staff and the participants of the study for their valuable contributions.

Conflict of interest

The author(s) declared no potential conflicts of interest with respect to the research, authorship, and/or publication of this article.

Generative AI statement

The author(s) declare that no Generative AI was used in the creation of this manuscript.

Supplementary material

The Supplementary Material for this article can be found online at: <https://www.ebm-journal.org/articles/10.3389/ebm.2025.10624/full#supplementary-material>

2. Lau AY, Wong KS, Lev M, Furie K, Smith W, Kim AS. Burden of intracranial steno-occlusive lesions on initial computed tomography angiography predicts poor

outcome in patients with acute stroke. *Stroke* (2013) **44**:1310–6. doi:10.1161/strokeaha.111.672741

3. Lei C, Wu B, Liu M, Chen Y. Risk factors and clinical outcomes associated with intracranial and extracranial atherosclerotic stenosis acute ischemic stroke. *J Stroke Cerebrovasc Dis* (2014) **23**:1112–7. doi:10.1016/j.jstrokecerebrovasdis.2013.09.024

4. Feigin VL, Abate MD, Abate YH, Abd ElHafeez S, Abd-Allah F, Abdelalim A, et al. Global, regional, and national burden of stroke and its risk factors, 1990–2021: a systematic analysis for the global burden of disease study 2021. *The Lancet Neurol* (2024) **23**:973–1003. doi:10.1016/s1474-4422(24)00369-7

5. Yu EP, Bennett MR. Mitochondrial DNA damage and atherosclerosis. *Trends Endocrinol & Metab* (2014) **25**:481–7. doi:10.1016/j.tem.2014.06.008

6. Stöger JL, Gijbels MJ, van der Velden S, Manca M, van der Loos CM, Biessen EA, et al. Distribution of macrophage polarization markers in human atherosclerosis. *Atherosclerosis* (2012) **225**:461–8. doi:10.1016/j.atherosclerosis.2012.09.013

7. Chen Y, Yang M, Huang W, Chen W, Zhao Y, Schulte ML, et al. Mitochondrial metabolic reprogramming by cd36 signaling drives macrophage inflammatory responses. *Circ Res* (2019) **125**:1087–102. doi:10.1161/circresaha.119.315833

8. Chiu YC, Chu PW, Lin HC, Chen SK. Accumulation of cholesterol suppresses oxidative phosphorylation and altered responses to inflammatory stimuli of macrophages. *Biochem Biophys Rep* (2021) **28**:101166. doi:10.1016/j.bbrep.2021.101166

9. Castellani CA, Longchamps RJ, Sun J, Guallar E, Arking DE. Thinking outside the nucleus: mitochondrial DNA copy number in health and disease. *Mitochondrion* (2020) **53**:214–23. doi:10.1016/j.mito.2020.06.004

10. Piotrowska-Nowak A, Elson JL, Sobczyk-Kopciol A, Piwonska A, Puch-Walczak A, Drygas W, et al. New mtDNA association model, mutpred variant load, suggests individuals with multiple mildly deleterious mtDNA variants are more likely to suffer from atherosclerosis. *Front Genet* (2018) **9**:702. doi:10.3389/fgene.2018.00702

11. Uchikado Y, Ikeda Y, Sasaki Y, Iwabayashi M, Akasaki Y, Ohishi M. Association of lectin-like oxidized low-density lipoprotein receptor-1 with angiotensin II type 1 receptor impacts mitochondrial quality control, offering promise for the treatment of vascular senescence. *Front Cardiovasc Med* (2021) **8**:788655. doi:10.3389/fcvm.2021.788655

12. Mills EL, Kelly B, Logan A, Costa ASH, Varma M, Bryant CE, et al. Succinate dehydrogenase supports metabolic repurposing of mitochondria to drive inflammatory macrophages. *Cell* (2016) **167**:457–70.e13. doi:10.1016/j.cell.2016.08.064

13. Hubens WHG, Vallbona-Garcia A, de Coe IFM, van Tienen FHJ, Webers CAB, Smeets HJM, et al. Blood biomarkers for assessment of mitochondrial dysfunction: an expert review. *Mitochondrion* (2022) **62**:187–204. doi:10.1016/j.mito.2021.10.008

14. Liu CS, Tsai CS, Kuo CL, Chen HW, Lii CK, Ma YS, et al. Oxidative stress-related alteration of the copy number of mitochondrial DNA in human leukocytes. *Free Radic Res* (2003) **37**:1307–17. doi:10.1080/10715760310001621342

15. Chong MR, Narula S, Morton R, Judge C, Akhbar L, Cawte N, et al. Mitochondrial DNA copy number as a marker and mediator of stroke prognosis: observational and mendelian randomization analyses. *Neurology* (2022) **98**:e470–e482. doi:10.1212/wnl.00000000000013165

16. Jiang Y, Cheng S, Shi Y, Xu Z, Wang H, Li Y, et al. Subtype-specific association of mitochondrial DNA copy number with poststroke/TIA outcomes in 10 241 patients in China. *Stroke* (2024) **55**:1261–70. doi:10.1161/strokeaha.123.045069

17. Ballinger SW, Patterson C, Knight-Lozano CA, Burow DL, Conklin CA, Hu Z, et al. Mitochondrial integrity and function in atherogenesis. *Circulation* (2002) **106**:544–9. doi:10.1161/01.cir.0000023921.93743.89

18. Yu EPK, Reinhold J, Yu H, Starks L, Uryga AK, Foote K, et al. Mitochondrial respiration is reduced in atherosclerosis, promoting necrotic core formation and reducing relative fibrous cap thickness. *Arteriosclerosis, Thromb Vasc Biol* (2017) **37**:2322–32. doi:10.1161/atvbaha.117.310042

19. Chen S, Xie X, Wang Y, Gao Y, Xie X, Yang J, et al. Association between leukocyte mitochondrial DNA content and risk of coronary heart disease: a case-control study. *Atherosclerosis* (2014) **237**:220–6. doi:10.1016/j.atherosclerosis.2014.08.051

20. Liu LP, Cheng K, Ning MA, Li HH, Wang HC, Li F, et al. Association between peripheral blood cells mitochondrial DNA content and severity of coronary heart disease. *Atherosclerosis* (2017) **261**:105–10. doi:10.1016/j.atherosclerosis.2017.02.013

21. Wang XB, Cui NH, Zhang S, Liu ZJ, Ma JF, Ming L. Leukocyte telomere length, mitochondrial DNA copy number, and coronary artery disease risk and

severity: a two-stage case-control study of 3064 Chinese subjects. *Atherosclerosis* (2019) **284**:165–72. doi:10.1016/j.atherosclerosis.2019.03.010

22. Chien MC, Huang WT, Wang PW, Liou CW, Lin TK, Hsieh CJ, et al. Role of mitochondrial DNA variants and copy number in diabetic atherogenesis. *Genet Mol Res* (2012) **11**:3339–48. doi:10.4238/2012.September.17.4

23. Hindson BJ, Ness KD, Masquelier DA, Belgrader P, Heredia NJ, Makarewicz AJ, et al. High-throughput droplet digital PCR system for absolute quantitation of DNA copy number. *Anal Chem* (2011) **83**:8604–10. doi:10.1021/ac202028g

24. Yang Y, Kong Q, Ma X, Wang C, Xue S, Du X. A whole-scope evaluation of cervicocephalic atherosclerotic burden is essential to predict 90-day functional outcome in large-artery atherosclerotic stroke. *J Atheroscler Thromb* (2022) **29**:1522–33. doi:10.5551/jat.63226

25. Adams HP, Jr, Bendixen BH, Kappelle LJ, Biller J, Love BB, Gordon DL, et al. Classification of subtype of acute ischemic stroke. Definitions for use in a multicenter clinical trial. Toast. Trial of org 10172 in acute stroke treatment. *Stroke* (1993) **24**:35–41. doi:10.1161/01.str.24.1.35

26. DeGraba TJ, Hallenbeck JM, Pettigrew KD, Dutka AJ, Kelly BJ. Progression in acute stroke: value of the initial NIH stroke scale score on patient stratification in future trials. *Stroke* (1999) **30**:1208–12. doi:10.1161/01.str.30.6.1208

27. Kleindorfer DO, Towfighi A, Chaturvedi S, Cockroft KM, Gutierrez J, Lombardi-Hill D, et al. 2021 guideline for the prevention of stroke in patients with stroke and transient ischemic attack: a guideline from the American heart association/American stroke association. *Stroke* (2021) **52**:e364–e467. doi:10.1161/str.0000000000000375

28. Barnett HJM, Taylor DW, Haynes RB, Sackett DL, Peerless SJ, Ferguson GG, et al. Beneficial effect of carotid endarterectomy in symptomatic patients with high-grade carotid stenosis. *N Engl J Med* (1991) **325**:445–53. doi:10.1056/nejm199108153250701

29. Chimowitz MI, Kokkinos J, Strong J, Brown MB, Levine SR, Silliman S, et al. The warfarin-aspirin symptomatic intracranial disease study. *Neurology* (1995) **45**:1488–93. doi:10.1212/wnl.45.8.1488

30. Kong Q, Ma X, Wang C, Du X, Ren Y, Wan Y. Total atherosclerosis burden of baroreceptor-resident arteries independently predicts blood pressure dipping in patients with ischemic stroke. *Hypertension* (2020) **75**:1505–12. doi:10.1161/hypertensionaha.120.15036

31. van Swieten JC, Koudstaal PJ, Visser MC, Schouten HJ, van Gijn J. Interobserver agreement for the assessment of handicap in stroke patients. *Stroke* (1988) **19**:604–7. doi:10.1161/01.str.19.5.604

32. Yu E, Calvert PA, Mercer JR, Harrison J, Baker L, Figg NL, et al. Mitochondrial DNA damage can promote atherosclerosis independently of reactive oxygen species through effects on smooth muscle cells and monocytes and correlates with higher-risk plaques in humans. *Circulation* (2013) **128**:702–12. doi:10.1161/circulationaha.113.002271

33. Fetterman JL, Holbrook M, Westbrook DG, Brown JA, Feeley KP, Bretón-Romero R, et al. Mitochondrial DNA damage and vascular function in patients with diabetes mellitus and atherosclerotic cardiovascular disease. *Cardiovasc Diabetol* (2016) **15**:53. doi:10.1186/s12933-016-0372-y

34. Wang Y, Wang GZ, Rabinovitch PS, Tabas I. Macrophage mitochondrial oxidative stress promotes atherosclerosis and nuclear factor- κ B-mediated inflammation in macrophages. *Circ Res* (2014) **114**:421–33. doi:10.1161/circresaha.114.302153

35. Peng W, Cai G, Xia Y, Chen J, Wu P, Wang Z, et al. Mitochondrial dysfunction in atherosclerosis. *DNA Cell Biol* (2019) **38**:597–606. doi:10.1089/dna.2018.4552

36. Shemiakova T, Ivanova E, Grechko AV, Gerasimova EV, Sobenin IA, Orekhov AN. Mitochondrial dysfunction and DNA damage in the context of pathogenesis of atherosclerosis. *Biomedicines* (2020) **8**:166. doi:10.3390/biomedicines8060166

37. Kaito M, Araya S, Gondo Y, Fujita M, Minato N, Nakanishi M, et al. Relevance of distinct monocyte subsets to clinical course of ischemic stroke patients. *PLoS One* (2013) **8**:e69409. doi:10.1371/journal.pone.0069409

38. Virag L. Structure and function of poly(adp-ribose) polymerase-1: role in oxidative stress-related pathologies. *Curr Vasc Pharmacol* (2005) **3**:209–14. doi:10.2174/1570161054368625

39. Jacinto TA, Meireles GS, Dias AT, Aires R, Porto ML, Gava AL, et al. Increased ROS production and DNA damage in monocytes are biomarkers of aging and atherosclerosis. *Biol Res* (2018) **51**:33. doi:10.1186/s40659-018-0182-7

40. Masi S, Orlandi M, Parkar M, Bhowruth D, Kingston I, O'Rourke C, et al. Mitochondrial oxidative stress, endothelial function and metabolic control in patients with type II diabetes and periodontitis: a randomised controlled clinical trial. *Int J Cardiol* (2018) **271**:263–8. doi:10.1016/j.ijcard.2018.05.019



OPEN ACCESS

*CORRESPONDENCE

Samuel Dagogo-Jack,
✉ sdj@uthsc.edu

RECEIVED 21 February 2025

ACCEPTED 05 June 2025

PUBLISHED 24 June 2025


CITATION

Asuzu P, Feto NA, Wan J, Stentz F, Mandal N and Dagogo-Jack S (2025) Selective association of plasma sphingolipid species with insulin sensitivity and secretion in normoglycemic Black and White American adults. *Exp. Biol. Med.* 250:10538. doi: 10.3389/ebm.2025.10538

COPYRIGHT

© 2025 Asuzu, Feto, Wan, Stentz, Mandal and Dagogo-Jack. This is an open-access article distributed under the terms of the [Creative Commons Attribution License \(CC BY\)](https://creativecommons.org/licenses/by/4.0/). The use, distribution or reproduction in other forums is permitted, provided the original author(s) and the copyright owner(s) are credited and that the original publication in this journal is cited, in accordance with accepted academic practice. No use, distribution or reproduction is permitted which does not comply with these terms.

Selective association of plasma sphingolipid species with insulin sensitivity and secretion in normoglycemic Black and White American adults

Peace Asuzu¹, Naser Aliye Feto², Jim Wan³, Frankie Stentz¹, Nawajes Mandal² and Samuel Dagogo-Jack ^{1*}

¹Department of Medicine, Division of Endocrinology, Diabetes and Metabolism, University of Tennessee Health Science Center, Memphis, TN, United States, ²Department of Ophthalmology, University of Tennessee Health Science Center, Memphis, TN, United States, ³Department of Preventive Medicine, University of Tennessee Health Science Center, Memphis, TN, United States

Abstract

Ceramides and other sphingolipids are associated with diabetes risk. Here, we examined the association of plasma sphingolipids with insulin sensitivity and secretion in people without diabetes. We enrolled adults without diabetes based on 75-g oral glucose tolerance test. Assessments included clinical examination, insulin sensitivity (hyperinsulinemic euglycemic clamp), and insulin secretion (intravenous glucose tolerance test). Plasma levels of 58 sphingolipid species (including ceramides, monohexosylceramides, sphingomyelins, and sphingosine) were assayed using liquid chromatography tandem mass spectrometry. The study participants (N = 240; 129 Black, 111 White) had a mean age of 43.1 ± 12.0 y, body mass index (BMI) 29.4 ± 6.23 kg/m², fasting plasma glucose 91.4 ± 6.91 mg/dL, and 2-h plasma glucose 123 ± 26.3 mg/dL. Several of the 58 SPLs species assayed showed variable associations with insulin sensitivity ($r = 0.17-0.35$, $P = 0.039 - <0.0001$) and secretion ($r = 0.14-0.27$; $P = 0.038 - <0.0001$). After correction for multiple testing, plasma levels of very-long-chain (VLC) monohexosylceramide C34:0 ($r = 0.31 - 0.43$, $P < 0.0001$) and VLC sphingomyelins C28-C34 ($r = 0.31-0.35$, $P = 0.0004 - <0.0001$) were significantly associated with insulin sensitivity. Plasma VLC sphingomyelin level were inversely associated with insulin secretion, plasma glucose, BMI, and waist circumference. We conclude that circulating VLC sphingomyelins are associated positively with insulin action and inversely with insulin secretion and adiposity in normoglycemic adults, indicating a possible link to glucoregulation that precedes the development of dysglycemia.

KEYWORDS

adiposity, beta-cell function, ceramide, insulin resistance, sphingomyelin

Impact statement

Accumulation of ceramides and other sphingolipids results in lipotoxicity, insulin resistance, and increased diabetes risk. We assessed the relationship between circulating levels of selected sphingolipids and glucoregulatory physiology in adults without diabetes. Our findings demonstrate heterogeneity among plasma sphingolipid species regarding their association with sensitivity and secretion. Long-chain ceramides and sphingomyelins associate inversely with insulin sensitivity and positively with insulin secretion; very-long-chain sphingolipids species associate positively with insulin sensitivity and inversely with insulin secretion. Very-long-chain sphingolipids also were inversely associated with adiposity and glycemia, indicating a beneficial glucoregulatory and metabolic profile. These findings suggest a physiological link between metabolism of certain sphingolipids and glucose regulation long before the development of dysglycemia.

Introduction

Sphingolipids are specialized lipids in mammalian cells that have a structure characterized by the presence of an amino dihydroxy alkane, a sphingoid base, an N-bound fatty acid, and a variable head group [1–3]. The major classes of sphingolipids include ceramides, monohexosylceramides, sphingomyelins, and sphingosines, among others. Variability in carbon length, saturation, and hydroxylation within structural components of sphingolipids has generated several thousand individual species of sphingolipids [1–3]. The spectrum of biological roles of sphingolipids includes cell membrane integrity and modulation of inflammation, signaling, differentiation, growth, senescence, and cell death [4–7].

Tissue accumulation of ceramides impairs insulin signaling and induces pancreatic beta-cell apoptosis, with consequent glucose dysregulation [7–9]. Furthermore, the roles of specific sphingolipids in the pathophysiology of diverse endocrine and metabolic conditions, including mitochondrial dysfunction, thyroid eye disease, autoimmune disorders, metabolic dysfunction-associated fatty liver disease, brain insulin resistance and neurodegenerative disorders, and glucose dysregulation are being increasingly recognized (reviewed recently by Li et al. [7]).

Modern lipidomic technology has enabled precise quantitation of individual sphingolipid species in human plasma, and alterations in circulating levels of certain sphingolipid species have been associated with obesity, diabetes, and prediabetes [10–15]. Furthermore, plasma levels of specific ceramides and other sphingolipid species have been reported to be significantly associated with measures of insulin sensitivity and insulin secretion in studies that included individuals with obesity or type 2 diabetes [9, 16–18].

Hyperglycemia is known to increase *de novo* synthesis of ceramides and alter the abundance of other sphingolipid species through modulation of specific enzymes involved in the sphingolipid metabolism, including serine palmitoyltransferase and sphingomyelinases [19–21].

The aim of the present report was to determine the association of a broad range of circulating sphingolipid species with measures of insulin sensitivity and insulin secretion in individuals without diabetes. By studying such individuals, we hoped to avoid any metabolic effects of dysglycemia *per se* on lipid metabolism [19–21]. The development of insulin resistance precedes the occurrence of type 2 diabetes by several years; similarly, the loss of first-phase insulin secretory response to glucose challenge represents early evidence of pancreatic beta-cell defect that precedes the diagnosis of diabetes by several years [22, 23]. Thus, we reasoned that the reports linking sphingolipids to diabetes probably represent a distal relationship that might be discernible proximally, prior to the occurrence of dysglycemia. The aim of the present study was to assess the association of plasma levels of 58 selected sphingolipid species with insulin sensitivity and insulin secretion in adults without diabetes.

Materials and methods

Study subjects

Study participants were selected from the Pathobiology of Prediabetes in a Biracial Cohort (POP-ABC) [24, 25]. Participants were eligible for the POP-ABC study if they were 18–65 years, self-reported as non-Hispanic Black (African American) or non-Hispanic White (European American) and had biological parent(s) with type 2 diabetes. Additional participants were included from the POP-ABC normative cohort comprising African American European American adults without a family history of diabetes. All participants underwent a screening 75-gram oral glucose tolerance test (OGTT) to document normal fasting plasma glucose (FPG; <100 mg/dL [5.6 mmol/L]) and/or normal glucose tolerance (2-h plasma glucose [2hPG] <140 mg/dL [7.8 mmol/L]) [17, 18]. Intercurrent illness, hyperglycemia, a history of diabetes, or exposure to medications known to alter glucose metabolism were among the exclusion criteria [24, 25]. A written informed consent was obtained from all participants before enrollment in the POP-ABC study [24, 25].

For the present report, we selected African American participants (N = 129) and European American participants (N = 111), matched in age (within 5 years) and sex, who had completed assessment of insulin sensitivity and insulin secretion at enrollment [20, 21]. Plasma specimens obtained from the participants at enrollment were analyzed for sphingolipid levels

in the ongoing Ceramides and Sphingolipids as Predictors of Incident Dysglycemia (CASPID) study. The CASPID study protocol (IRB Approval #21-07936-FB) was approved by the University of Tennessee Health Science Center (UTHSC) Institutional Review Board and carried out at the UTHSC General Clinical Research Center (GCRC).

Assessments

Participants arrived at the GCRC after fasting overnight for baseline assessments. These included a structured medical interview and general physical examination, measurement of height, weight, waist circumference, and OGTT. The body mass index (BMI) was calculated as weight in kilograms divided by the height in meters squared. Additional assessments included measurement of insulin sensitivity and insulin secretion.

Oral glucose tolerance test

Ahead of the baseline visit, participants received written instructions to continue with their normal diet, refrain from strenuous exercise and alcohol consumption for a day prior, and to avoid smoking the morning of the OGTT. After an overnight fast, venous blood specimens were sampled from participants before (0 min) and at 30 and 120 min after drinking 75 g of flavored glucose solution (Trutol 75; Custom Laboratories, Baltimore, MD) [24, 25].

Insulin sensitivity

Whole body insulin sensitivity was assessed using the hyperinsulinemic euglycemic clamp method of DeFronzo et al. [26]. In brief, participants were fasted overnight for approximately 12 h before undergoing the clamp studies at the GCRC. A primed, continuous intravenous infusion of regular insulin (2 mU/kg/min; 12 pmol/kg/min) was administered for 180 min through intravenous cannulas in both arms, while maintaining blood glucose level at ~100 mg/dL (5.6 mmol/L) with a variable rate dextrose (20%) infusion. Glucose and insulin measurements were carried out on arterialized blood samples obtained every 10 min during the procedure. During the final 60 min of insulin infusion (steady state), the total insulin-stimulated glucose disposal rate (M) was calculated and corrected for the steady-state plasma insulin levels to derive the final insulin sensitivity index (Si-clamp), as previously described [24–26]. Fasting glucose and insulin levels were used to calculate the homeostasis model assessment of insulin resistance (HOMA-IR) (HOMA2 calculator. <https://homa-calculator.informer.com/2.2/>) based on Matthews et al. [27].

Insulin secretion

Acute insulin secretory response to glucose (AIRg) was assessed using the frequently sampled intravenous glucose tolerance test (FSIGT), as previously described [24, 25]. In brief, after an overnight fast, participants arrived at the GCRC for the FSIGT. An intravenous dextrose bolus (25g) was administered, with arterialized blood sampling for the measurement of glucose and insulin levels at –30, 0, 2, 3, 4, 5, 7, and 10 min relative to dextrose bolus. The AIRg was computed as the mean incremental insulin concentration from 3 to 5 min after the dextrose bolus [23, 25, 28]. Fasting glucose and insulin levels were used to calculate the homeostasis model assessment of beta cells (HOMA-B) (HOMA2 calculator. <https://homa-calculator.informer.com/2.2/>) based on Matthews et al. [27]. The disposition index, a measure of the insulin secretion corrected for ambient insulin sensitivity, was calculated as AIRg x Si-clamp [29].

Biochemical assays

Plasma glucose levels during OGTT and hyperinsulinemic euglycemic clamp were measured at the bedside using the YSI glucose analyzer (Yellow Spring Instruments Co., Inc., Yellow Spring, OH). Plasma insulin levels were measured in our Endocrine Research Laboratory with a solid phase, two-site sequential chemiluminescent immunometric assays on the Siemens Immulite analyzer (Siemens Healthcare Diagnostics Products, Ltd., Camberley, Surrey, UK). The within-batch variation coefficient for the insulin assay was <5%.

Lipidomic analysis

Targeted lipidomic analysis was performed in baseline plasma specimens obtained at enrolment in the POP-ABC study. The plasma specimens preserved in EDTA were stored at –80°C until the lipidomic analysis. A total of 58 selected sphingolipids of various classes (ceramides, monohexosylceramides, sphingomyelins, sphingosine and dihydro-sphingosine-1-phosphate) were assayed using liquid chromatography-tandem mass spectrometry (LC-MS/MS). The measurements were carried out at the Lipidomics Core at Virginia Commonwealth University, Richmond, Virginia, using established protocols [19, 20]. The individual sphingolipid species were validated and quantified using a Shimadzu LC-20 AD binary pump system coupled to a SIL-20AC autoinjector, and a DGU20A3 degasser coupled to an ABI 4000 quadrupole/linear ion trap (QTrap) (Applied Biosystems), operating in triple quadrupole mode. Using the retention times and m/z ratio, the 58 SPL species were identified and quantified

TABLE 1 Baseline characteristics of study participants.

Characteristics	All	African American	European American	P-value
Number	240	129	111	
Male/Female	90/150	48/81	42/69	
Age (yr)	43.1 ± 12.0	42.0 ± 11.6	44.4 ± 12.4	0.12
BMI (kg/m ²)	29.4 ± 6.23	30.9 ± 6.52	27.7 ± 5.40	<0.0001
Female	30.2 ± 6.49	32.0 ± 6.31	28.1 ± 6.08	0.0002
Male	28.2 ± 5.59	29.2 ± 6.55	27.1 ± 4.02	0.075
Waist circum. (cm)	93.4 ± 15.0	96.2 ± 15.5	90.1 ± 13.8	0.0017
Female	92.0 ± 15.1	95.8 ± 14.8	87.5 ± 14.3	0.0007
Male	95.7 ± 14.6	96.9 ± 16.6	94.4 ± 11.7	0.42
FPG (mg/dL)	91.4 ± 6.91	90.3 ± 7.12	92.5 ± 6.50	0.013
2hrPG (mg/dL)	123 ± 26.3	123 ± 25.9	123 ± 26.9	0.93
Total sphingolipids (nmol/mL)	96.0 ± 25.7	96.3 ± 26.0	95.7 ± 25.4	0.85
Total ceramides (nmol/mL)	3.36 ± 1.48	3.22 ± 1.42	3.53 ± 1.54	0.11
Monohexosyl ceramides (nmol/mL)	4.62 ± 2.73	4.45 ± 2.78	4.82 ± 2.66	0.28
Total sphingomyelins (nmol/mL)	87.4 ± 23.7	88.0 ± 23.9	86.8 ± 23.7	0.68
Sphingosine (pmol/mL)	121 ± 54.8	126 ± 54.3	116 ± 55.1	0.18

FPG, fasting plasma glucose; 2hrPG, two-hour plasma glucose. To convert plasma glucose from mg/dL to mmol/L, multiply by 0.056.

by comparing the target lipid ion of interest with the normalization of quantitated ion abundances [30, 31].

Statistical analysis

Data were reported as means ± SD. The significance of differences between defined groups was analyzed using t-test for continuous variables and chi squared test for categorical variables. Linear regression models were used to assess the relationship between individual sphingolipid species and measures of adiposity, insulin secretion, and insulin sensitivity. Significance level was generally set as $P < 0.05$ (two-tailed). For analysis of the association of 58 individual sphingolipid species with insulin sensitivity or insulin secretion, a Bonferroni-corrected significant P value of <0.0009 was adopted, to minimize false discovery from multiple comparisons. The analyses were performed using SAS 9.4 (SAS Institute Inc., Cary, NC).

Results

Cohort description

The study population ($N = 240$; 150 women, 90 men) comprised 129 African American (non-Hispanic Black) and

111 European American (non-Hispanic White) participants. Table 1 shows their baseline characteristics. The mean age was 43.1 ± 12.0 y, BMI 29.4 ± 6.23 kg/m², fasting plasma glucose 91.4 ± 6.91 mg/dL, and 2-hr plasma glucose 123 ± 26.3 mg/dL (Table 1). The mean fasting plasma glucose was lower, and the BMI and waist circumference were higher, in African American vs. European American participants. However, there were no ethnic differences in 2-hr plasma glucose or total plasma levels of sphingolipids, ceramides, monohexosyl ceramides, sphingomyelins, and sphingosine (Table 1).

Association of selected plasma sphingolipids with insulin sensitivity

Nominally significant associations were observed between several sphingolipid species and whole-body insulin sensitivity (Si-clamp) (Supplementary Table S1). Plasma levels of long-chain ceramide C18:1 ($r = -0.22$, $P = 0.0062$) and long-chain sphingomyelin C18:1 ($r = -0.23$, $P = 0.0046$) were inversely associated with insulin sensitivity (Supplementary Table S1). In contrast, plasma levels very-long-chain ceramide C26:0 ($r = 0.20$, $P = 0.014$), monohexosylceramide C34:0 ($r = 0.30$, $P = 0.0002$) and sphingomyelin C28 – C34 species were positively associated with insulin sensitivity (Supplementary Table S1). No other circulating sphingolipid species (including ceramides,

TABLE 2 Plasma sphingolipid species significantly associated with insulin sensitivity or insulin secretion.

Insulin sensitivity				
Sphingolipids (pmol/mL)	Mean ± SD	r	P Value	Adjusted P value ^a
MHC C34:0	0.28 ± 0.28	0.30	0.0002	0.0047
SM C28:1	18.5 ± 8.07	0.34	<0.0001	0.0003
SM C28:0	39.3 ± 20.7	0.31	0.0001	0.0003
SM C30:1	10.1 ± 4.39	0.29	0.0004	0.0026
SM C30:0	8.35 ± 3.89	0.32	<0.0001	0.0003
SM C32:0	2.74 ± 1.49	0.35	<0.0001	0.0002
SM C34:0	1.22 ± 0.61	0.31	0.0001	0.0023
Total VLC	82.5 ± 36.2	0.35	<0.0001	<0.0001
Insulin secretion				
Sphingolipids (pmol/mL)	Mean ± SD	r	P Value	Adjusted P value
SM C28:0	39.3 ± 20.7	−0.25	0.0003	0.0012
SM C30:1	8.35 ± 3.89	−0.27	<0.0001	0.0007

^aAdjusted for age, sex, race/ethnicity and BMI.

monohexosylceramides, sphingomyelins or sphingosines) reached even nominally significant association with insulin sensitivity in our study population.

After correction for multiple testing, plasma levels of very-long-chain monohexosylceramides C34:0 ($r = 0.30$, $P = 0.0002$), very-long-chain sphingomyelins C28:1, C28:0, C30:1, C30:0, C32:0, and C34:0 ($r = 0.31$ – 0.35 , $P = 0.0004$ - <0.0001) were positively associated with insulin sensitivity (Table 2; Supplementary Table S1). Notably, there was no significant association between plasma levels of total ceramides, total monohexosylceramides, sphingosine, or total sphingolipids and insulin sensitivity (Supplementary Table S1). In contrast, plasma levels of total very-long-chain sphingomyelins were significantly associated with insulin sensitivity ($r = 0.35$, $P < 0.0001$) (Supplementary Table S1).

Association of selected plasma sphingolipids with insulin secretion

Compared to insulin sensitivity, fewer individual sphingolipid species showed nominally significant associations with insulin secretion (Supplementary Table S2). Inverse associations with AIRg were observed for the very-long-chain sphingomyelins C28:0 ($r = -0.25$, $P = 0.0003$), C30:1 ($r = -0.27$, $P < 0.0001$), and C30:0 ($r = -0.20$, $P = 0.0044$) ($r = -0.16$, $P = 0.024$) that had showed positive associations with insulin sensitivity (Supplementary Tables S1, S2). Weaker inverse

associations with AIRg were observed for some very-long-chain ceramide species ($r = -0.14$ to -0.16 , $P = 0.05$ - <0.018) and very-long-chain monohexosylceramide C28:1 ($r = -0.16$, $P = 0.024$) (Supplementary Table S2). In contrast, positive associations with AIRg were observed for plasma levels of the long-chain sphingomyelins C18:1 ($r = 0.23$, $P = 0.0009$) and C18:0 ($r = 0.22$, $P = 0.0012$) that were inversely associated with insulin sensitivity (Supplementary Tables S1, S2).

Unlike the findings regarding insulin sensitivity, most of the associations between individual sphingolipid species and AIRg lost statistical significance after Bonferroni correction for multiple testing, except for the association with very-long-chain sphingomyelins C28:0 and C30:1 (Table 2; Supplementary Table S2). Plasma levels of total very-long-chain sphingomyelins were significantly associated with AIRg ($r = -0.27$, $P < 0.0002$). In contrast, total plasma levels of sphingolipids and major species (ceramides, monohexosylceramides, sphingosine) were not significantly associated with insulin secretion (Supplementary Table S2).

Plasma levels of very-long-chain sphingomyelins C28:0, C28:1, C30:1 showed concurrent associations with insulin sensitivity ($r = 0.31$ – 0.34 ; $P = 0.0004$ - <0.0001) and AIRg ($r = -0.20$ to -0.27 ; $P = 0.004$ - <0.0001) (Figure 1; Supplementary Tables S1, S2).

Plasma levels of sphingomyelin C16:0 showed nominal associations with HOMA-IR ($r = 0.18$, $P = 0.038$) and HOMA-B ($r = 0.23$, $P = 0.009$), as did sphingomyelin C34:0 with HOMA-B ($r = 0.18$, $P = 0.036$). However, the

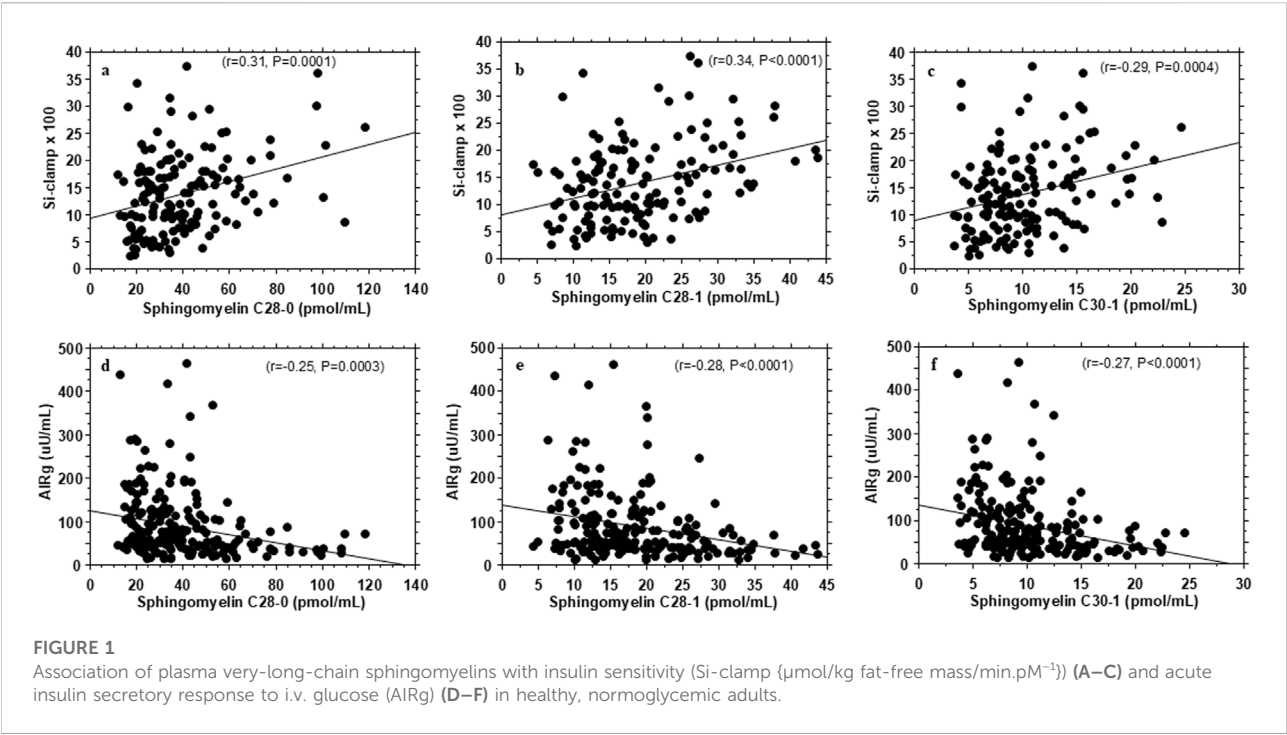


TABLE 3 Correlation of adiposity and glycemic measures with sphingolipid species significantly associated with insulin sensitivity or insulin secretion.

Sphingolipid species	BMI		Waist circumference		FPG		2hrPG		HbA1c	
	r	P	r	P	r	P	r	P	r	P
MHC C34:0	−0.17	0.0075	−0.14	0.026	−0.14	0.028	−0.14	0.026	−0.19	0.0043
SM C28:1	−0.18	0.0062	−0.21	0.0015	0.06	0.38	−0.08	0.21	−0.03	0.66
SM C28:0	−0.14	0.030	−0.14	0.032	0.02	0.74	−0.16	0.017	−0.02	0.77
SM C30:1	−0.18	0.0042	−0.19	0.0030	0.05	0.45	−0.11	0.090	−0.04	0.57
SM C30:0	−0.17	0.010	−0.21	0.0012	−0.09	0.19	−0.23	0.0003	−0.11	0.11
SM C32:0	−0.16	0.011	−0.23	0.0004	−0.13	0.041	−0.13	0.048	−0.17	0.0084
SM C34:0	−0.13	0.046	−0.14	0.038	−0.03	0.66	−0.17	0.010	−0.05	0.44
VLC SM	−0.17	0.0080	−0.19	0.0039	0.01	0.83	−0.16	0.015	−0.04	0.50

FPG, fasting plasma glucose; 2hrPG, two-hour plasma glucose; MHC, monohexosylceramides; SM, sphingomyelin; VLC, very long chain.

associations were not significant after correction for multiple testing. The other sphingolipid species assessed in the present study showed no association with HOMA-IR or HOMA-B.

There were no significant differences by sex or race/ethnicity in the measured sphingolipid species. Further, the observed associations between sphingolipid species and insulin sensitivity and insulin secretion were consistent across race/ethnicity and sex.

Association with metabolic variables

Table 3 shows some metabolic correlates of the individual plasma sphingolipid species that exhibited significant associations with insulin sensitivity or insulin secretion. In general, the very-long-chain sphingomyelins and very-long-chain monohexosylceramide C34:0 that were positively associated with insulin sensitivity showed inverse correlations with waist circumference and BMI (Figure 2; Table 3). The very-

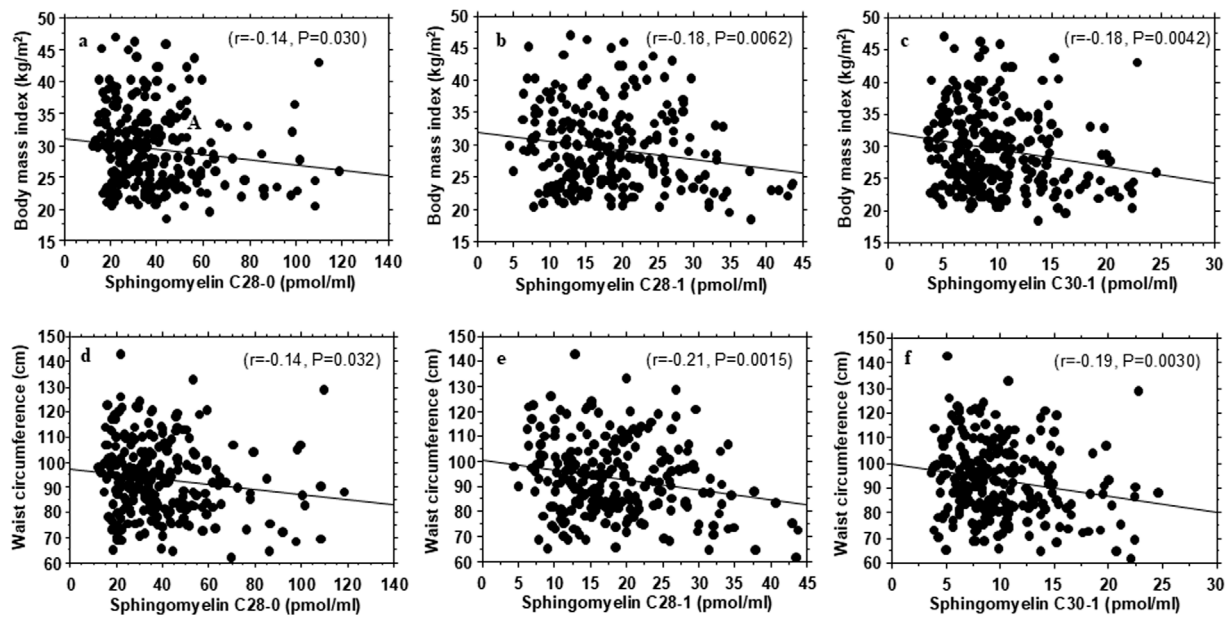


FIGURE 2

Association of plasma very-long-chain sphingomyelins with body mass index (A–C) and waist circumference (D–F) in healthy, normoglycemic adults.

long-chain monohexosylceramide C34:0 and other very-long-chain sphingomyelin species also were inversely correlated with fasting plasma glucose, 2-h plasma glucose or hemoglobin A1c levels (Table 3).

Discussion

Among our healthy, normoglycemic study participants, circulating levels of very-long-chain sphingomyelins correlated positively with insulin sensitivity and inversely with insulin secretion. Remarkably, few of the 58 individual sphingolipid species analyzed in the present study exhibited concurrent associations with insulin sensitivity and insulin secretion, after correction for multiple testing. Directionally, our findings suggest that the association of very-long-chain sphingomyelins with higher insulin sensitivity might be a primary phenomenon that resulted in a compensatory decrease in insulin secretion. It is physiologically less likely that a primary decrease in insulin secretion would trigger an increase in insulin sensitivity. Generally, improvements in insulin action result in decreased insulin demand (secretion).

The positive associations between very-long-chain sphingomyelins with insulin sensitivity suggest that higher levels of those moieties might portend a beneficial glucoregulatory profile, whereas lower levels might connote a less favorable profile. In fact, we found that plasma levels of

very-long-chain sphingomyelins were inversely correlated with measures of obesity and glycemia. Thus, participants with higher plasma levels of very-long-chain sphingomyelins were more likely to have higher insulin sensitivity, lower BMI, waist circumference and lower plasma glucose levels, compared with participants with lower levels. Consonant with our findings, lower plasma sphingomyelin levels have been linked to higher risk of developing type 2 diabetes and prediabetes during longitudinal follow-up [15, 32]. Interestingly, weight loss was accompanied by post-operative increases in circulating sphingomyelin levels following gastric bypass surgery [32]. In a previous report, we noted modest differences in plasma levels of some sphingolipid species in people with parental history of type 2 diabetes versus those without a family history of diabetes [32]. In general, circulating levels of ceramide, monohexosylceramide, and sphingosine species were lower and those of sphingomyelin species were higher in individuals with parental history of type 2 diabetes versus people without a family history of diabetes [33].

Very-long-chain fatty acids (>26 carbon chain) are synthesized by ELOVL4 (ELongation of Very Long chain fatty acid 4) in the endoplasmic reticulum. The very-long-chain fatty acids in sphingolipid classes are acylated by ceramide synthase 3 to a sphingoid backbone to generate very-long-chain ceramides, which are converted to very-long-chain sphingomyelins [1–4, 34–36]. Thus, increased generation of very-long-chain sphingomyelins is associated with decreased abundance of very-long-chain ceramides [34]. Ceramides induce

insulin resistance, and higher plasma levels of sphingosine have been shown to predict prediabetes risk [7–10, 15]. Taken together, our finding of a positive correlation between plasma very-long-chain sphingomyelins and whole-body insulin sensitivity is physiologically congruent, as higher sphingomyelins levels would predict a lower abundance of toxic ceramides and sphingosine [34]. Moreover, very-long-chain sphingolipids can regulate insulin action via their specialized role in transmembrane signal transduction [1–10, 37–40]. Notably, exposure to hyperglycemia decreases the levels of very long-chain sphingolipids released by cultured cells [38].

In the present study, the plasma levels of long-chain ceramide C18:1 were inversely associated with insulin sensitivity (i.e., higher levels indicated greater insulin resistance), whereas levels of very-long-chain ceramide C26:0 were positively associated with insulin sensitivity. Remarkably, no other ceramide species with fatty acid carbon chain length C14:0 – C34:0 analyzed in the present study showed significant associations with insulin sensitivity in our normoglycemic cohort. Previous studies that enrolled healthy persons and individuals with obesity and type 2 diabetes had reported similar findings of an inverse association between plasma levels of long-chain dihydroceramides (including C18:0, C20:0, and C22:0) and insulin sensitivity [9, 18].

Elevated ceramide levels were once thought to be uniformly detrimental to metabolic function through induction of insulin resistance, lipotoxicity, and beta-cell dysfunction [5, 6, 8, 10]. However, that view has been modified by reports of heterogeneity in the association between individual ceramide species and insulin sensitivity, based on acyl chain length. Higher levels of long-chain (C16–C22) ceramides are associated with insulin resistance, whereas very-long-chain (C > 22) ceramides are associated with improved insulin sensitivity [40–43]. Thus, our present findings align with the expanded understanding of the complex relationship between ceramides and insulin signaling. A similar dissociation between acyl chain length of ceramides and biological effect has been reported in the cancer literature [42].

The strengths of the present study include the focus on healthy, normoglycemic subjects, which enhances the physiological relevance of our findings. Further, we employed rigorous methodologies for the assessment of insulin sensitivity and acute insulin secretion. We also minimized the risk of false discovery by adjusting the significance of our data for multiple comparisons. Furthermore, it was reassuring that the plasma levels of the selected sphingolipid species measured in the present study were in the same range as values reported in pooled human plasma from healthy men and women in a representative of the US population [44]. One limitation of our study is that we did not include dihydro species of ceramide, monohexosylceramide, sphingomyelins, and other sphingoid base-containing species in our sphingolipid assays. Thus, we were unable to explore associations of insulin sensitivity and secretion with those unmeasured sphingolipid moieties. For example, dihydroceramide desaturase 1-catalyzed conversion of dihydroceramides to ceramides

has been suggested to play a role in the pathogenesis of insulin resistance [45]. Thus, inclusion of data on dihydroceramides could have provided a fuller picture on the relationship between sphingolipids and insulin action.

In conclusion, among normoglycemic Black and White American adults, circulating levels of the long-chain sphingolipids (C18:1 ceramide and C18:1 sphingomyelin) were associated inversely with insulin sensitivity, whereas the levels of several very-long-chain sphingolipids were associated positively with insulin sensitivity. We further demonstrate selective association of very-long-chain sphingomyelins with insulin sensitivity, insulin secretion, and adiposity in our normoglycemic adults. Our findings suggest that very-long-chain sphingomyelins may be agents or markers of underlying mechanisms related to optimal metabolic health.

Author contributions

SD-J participated in the concept and design of the study, supervised the acquisition and interpretation of data, and drafted the manuscript; NM participated in the concept and design of the study, interpretation of data, and review and revision of the manuscript; PA participated in the interpretation of data, and drafting, review, and revision of the manuscript; NF participated in the interpretation of data, and review and revision of the manuscript; FS participated in the interpretation of data, and review and revision of the manuscript; JW performed statistical analysis, reviewed and revised manuscript. All authors contributed to the article and approved the submitted version.

Author disclaimer

The content is solely the responsibility of the authors and does not represent the official views of the National Institutes of Health.

Data availability

The original contributions presented in the study are included in the article/Supplementary Material, further inquiries can be directed to the corresponding author.

Ethics statement

The studies involving humans were approved by The University of Tennessee Health Science Center (UTHSC) Institutional Review Board (IRB Approval #21-07936-FB). The studies were conducted in accordance with the local legislation and institutional requirements. The participants provided their written informed consent to participate in this study.

Funding

The author(s) declare that financial support was received for the research and/or publication of this article. The CASPID study is supported by a grant from the National Institute of Diabetes Digestive and Kidney Diseases (R01DK128129). The POP-ABC/PROP-ABC study was supported by a grant from the National Institute of Diabetes Digestive and Kidney Diseases (R01 DK067269).

Acknowledgments

The authors thank the research volunteers who participated in the POP-ABC study and the University of Tennessee Clinical Research Center staff for their assistance during the conduct of the study.

References

- Bartke N, Hannun YA. Bioactive sphingolipids: metabolism and function. *J Lipid Res* (2009) **50**(Suppl. 1):S91–96. doi:10.1194/jlr.r800080-jlr200
- Chen Y, Liu Y, Sullards MC, Merrill AH, Jr. An introduction to sphingolipid metabolism and analysis by new technologies. *NeuroMolecular Med* (2010) **12**(4):306–19. doi:10.1007/s12017-010-8132-8
- Meyer zu Heringdorf D, van Koppen CJ, Jakobs KH. Molecular diversity of sphingolipid signalling. *FEBS Lett* (1997) **410**(1):34–8. doi:10.1016/s0014-5793(97)00320-7
- Hannun YA, Obeid LM. Sphingolipids and their metabolism in physiology and disease. *Nat Rev Mol Cell Biol* (2018) **19**(3):175–91. doi:10.1038/nrm.2017.107
- Chaurasia B, Summers SA. Ceramides - lipotoxic inducers of metabolic disorders. *Trends Endocrinol and Metab* (2015) **26**(10):538–50. doi:10.1016/j.tem.2015.07.006
- Turpin-Nolan SM, Brüning JC. The role of ceramides in metabolic disorders: when size and localization matters. *Nat Rev Endocrinol* (2020) **16**(4):224–33. doi:10.1038/s41574-020-0320-5
- Li C, Li G. Editorial: the role of sphingolipid metabolism in endocrine diseases. *Front Endocrinol (Lausanne)* (2024) **15**:1506971. doi:10.3389/fendo.2024.1506971
- Sokolowska E, Blachnio-Zabielska A. The role of ceramides in insulin resistance. *Front Endocrinol (Lausanne)* (2019) **10**:577. doi:10.3389/fendo.2019.00577
- Zarini S, Brozinick JT, Zemski Berry KA, Garfield A, Perreault L, Kerege A, et al. Serum dihydroceramides correlate with insulin sensitivity in humans and decrease insulin sensitivity *in vitro*. *J Lipid Res* (2022) **63**(10):100270. doi:10.1016/j.jlr.2022.100270
- Mandal N, Gramberg R, Mondal K, Basu SK, Tahia F, Dagogo-Jack S. Role of ceramides in the pathogenesis of diabetes mellitus and its complications. *J Diabetes its Complications* (2021) **35**(2):107734. doi:10.1016/j.jdiacomp.2020.107734
- Haus JM, Kashyap SR, Kasumov T, Zhang R, Kelly KR, DeFronzo RA, et al. Plasma ceramides are elevated in obese subjects with type 2 diabetes and correlate with the severity of insulin resistance. *Diabetes* (2009) **58**(2):337–43. doi:10.2337/db08-1228
- Yun H, Sun L, Wu Q, Zong G, Qi Q, Li H, et al. Associations among circulating sphingolipids, β -cell function, and risk of developing type 2 diabetes: a population-based cohort study in China. *Plos Med* (2020) **17**(12):e1003451. doi:10.1371/journal.pmed.1003451
- Chew WS, Torta F, Ji S, Choi H, Begum H, Sim X, et al. Large-scale lipidomics identifies associations between plasma sphingolipids and T2DM incidence. *JCI Insight* (2019) **5**(13):e126925. doi:10.1172/jci.insight.126925
- Chen GC, Chai JC, Yu B, Michelotti GA, Grove ML, Fretts AM, et al. Serum sphingolipids and incident diabetes in a US population with high diabetes burden: the Hispanic Community Health Study/Study of Latinos (HCHS/SOL). *The Am J Clin Nutr* (2020) **112**(1):57–65. doi:10.1093/ajcn/nqaa114

Conflict of interest

The author(s) declared no potential conflicts of interest with respect to the research, authorship, and/or publication of this article.

Generative AI statement

The author(s) declare that no Generative AI was used in the creation of this manuscript.

Supplementary material

The Supplementary Material for this article can be found online at: <https://www.ebm-journal.org/articles/10.3389/ebm.2025.10538/full#supplementary-material>

- Dagogo-Jack S, Asuzu P, Wan J, Gramberg R, Stentz F, Mandal N. Plasma ceramides and other sphingolipids in relation to incident prediabetes in a longitudinal biracial cohort. *The J Clin Endocrinol and Metab* (2024) **109**(10):2530–40. doi:10.1210/clinem/dgae179
- Ye J, Ye X, Jiang W, Lu C, Geng X, Zhao C, et al. Targeted lipidomics reveals associations between serum sphingolipids and insulin sensitivity measured by the hyperinsulinemic-euglycemic clamp. *Diabetes Res Clin Pract* (2021) **173**:108699. doi:10.1016/j.diabres.2021.108699
- Lemaitre RN, Yu C, Hoofnagle A, Hari N, Jensen PN, Fretts AM, et al. Circulating sphingolipids, insulin, HOMA-IR, and HOMA-B: the strong heart family study. *Diabetes* (2018) **67**(8):1663–72. doi:10.2337/db17-1449
- Bergman BC, Brozinick JT, Strauss A, Bacon S, Kerege A, Bui HH, et al. Serum sphingolipids: relationships to insulin sensitivity and changes with exercise in humans. *Am J Physiology-Endocrinology Metab* (2015) **309**(4):E398–408. doi:10.1152/ajpendo.00134.2015
- Alka K, Mohammad G, Kowluru RA. Regulation of serine palmitoyl-transferase and Rac1-Nox2 signaling in diabetic retinopathy. *Sci Rep* (2022) **12**(1):16740. doi:10.1038/s41598-022-20243-2
- Zietzer A, Jahnel AL, Bulic M, Gutbrod K, Düsing P, Hosen MR, et al. Activation of neutral sphingomyelinase 2 through hyperglycemia contributes to endothelial apoptosis via vesicle-bound intercellular transfer of ceramides. *Cell Mol Life Sci* (2021) **79**(1):48. doi:10.1007/s00018-021-04049-5
- Parhofer KG. Interaction between glucose and lipid metabolism: more than diabetic dyslipidemia. *Diabetes Metab J* (2015) **39**(5):353–62. doi:10.4093/dmj.2015.39.5.353
- DeFronzo RA. From the triumvirate to the ominous octet: a new paradigm for the treatment of type 2 diabetes mellitus. *Diabetes* (2009) **58**(4):773–95. doi:10.2337/db09-9028
- Ward WK, Beard JC, Halter JB, Porte D, Jr. Pathophysiology of insulin secretion in diabetes mellitus. *Adv Exp Med Biol* (1985) **189**:137–58. doi:10.1007/978-1-4757-1850-8_9
- Dagogo-Jack S, Edeoga C, Nyenwe E, Chapp-Jumbo E, Wan J. Pathobiology of prediabetes in a biracial cohort (POP-ABC): design and methods. *Ethn Dis* (2011) **21**(1):33–9.
- Dagogo-Jack S, Edeoga C, Ebenibo S, Chapp-Jumbo E, Pathobiology of Prediabetes in a Biracial Cohort (POP-ABC) Research Group. Pathobiology of Prediabetes in a Biracial Cohort (POP-ABC) study: baseline characteristics of enrolled subjects. *The J Clin Endocrinol and Metab* (2013) **98**(1):120–8. doi:10.1210/jc.2012-2902
- DeFronzo RA, Tobin JD, Andres R. Glucose clamp technique: a method for quantifying insulin secretion and resistance. *Am J Physiology-Endocrinology Metab* (1979) **237**(3):E214–223. doi:10.1152/ajpendo.1979.237.3.e214
- Matthews D, Hosker J, Rudenski S, Naylor B, Treacher D, Turner C. Homeostasis model assessment: insulin resistance and β -cell function from

fasting plasma glucose and insulin concentrations in man. *Diabetologia* (1985) **28**(7):412–9. doi:10.1007/bf00280883

28. Weyer C, Bogardus C, Mott DM, Pratley RE. The natural history of insulin secretory dysfunction and insulin resistance in the pathogenesis of type 2 diabetes mellitus. *J Clin Invest* (1999) **104**(6):787–94. doi:10.1172/jci7231

29. Kahn SE, Prigeon RL, McCulloch DK, Boyko EJ, Bergman RN, Schwartz MW, et al. Quantification of the relationship between insulin sensitivity and β -cell function in human subjects. Evidence for a hyperbolic function. *Diabetes* (1993) **42**(11):1663–72. doi:10.2337/diab.42.11.1663

30. Shaner RL, Allegood JC, Park H, Wang E, Kelly S, Haynes CA, et al. Quantitative analysis of sphingolipids for lipidomics using triple quadrupole and quadrupole linear ion trap mass spectrometers. *J Lipid Res* (2009) **50**(8):1692–707. doi:10.1194/jlr.d800051-jlr200

31. Wilmott LA, Gramberg RC, Allegood JC, Lyons TJ, Mandal N. Analysis of sphingolipid composition in human vitreous from control and diabetic individuals. *J Diabetes its Complications* (2019) **33**(3):195–201. doi:10.1016/j.jdiacomp.2018.12.005

32. Carlsson ER, Grundtvig JLG, Madsbad S, Fenger M. Changes in serum sphingomyelin after Roux-en-Y gastric bypass surgery are related to diabetes status. *Front Endocrinol (Lausanne)* (2018) **9**:172. doi:10.3389/fendo.2018.00172

33. Mandal N, Stentz F, Asuzu PC, Nyenwe E, Wan J, Dagogo-Jack S. Plasma sphingolipid profile of healthy Black and white adults differs based on their parental history of type 2 diabetes. *The J Clin Endocrinol and Metab* (2024) **109**(3):740–9. doi:10.1210/clinem/dgad595

34. Gault CR, Obeid LM, Hannun YA. An overview of sphingolipid metabolism: from synthesis to breakdown. *Adv Exp Med Biol* (2010) **688**:1–23. doi:10.1007/978-1-4419-6741-1_1

35. Agbaga MP, Mandal MN, Anderson RE. Retinal very long-chain PUFAs: new insights from studies on ELOVL4 protein. *J Lipid Res* (2010) **51**(7):1624–42. doi:10.1194/jlr.r005025

36. Kady NM, Liu X, Lydic TA, Syed MH, Navitskaya S, Wang Q, et al. ELOVL4-mediated production of very long-chain ceramides stabilizes tight junctions and prevents diabetes-induced retinal vascular permeability. *Diabetes* (2018) **67**(4):769–81. doi:10.2337/db17-1034

37. Mondal K, Gramberg RC, Gangaraju R, Mandal N. A comprehensive profiling of cellular sphingolipids in mammalian endothelial and microglial cells cultured in normal and high-glucose conditions. *Cells* (2022) **11**(19):3082. doi:10.3390/cells11193082

38. Hopiavuori BR, Anderson RE, Agbaga MP. ELOVL4: very long-chain fatty acids serve an eclectic role in mammalian health and function. *Prog Retin Eye Res* (2019) **69**:137–58. doi:10.1016/j.preteyeres.2018.10.004

39. Deák F, Anderson RE, Fessler JL, Sherry DM. Novel cellular functions of very long chain-fatty acids: insight from ELOVL4 mutations. *Front Cell Neurosci* (2019) **13**:428. doi:10.3389/fncel.2019.00428

40. Montgomery MK, Brown SH, Lim XY, Fiveash CE, Osborne B, Bentley NL, et al. Regulation of glucose homeostasis and insulin action by ceramide acyl-chain length: a beneficial role for very long-chain sphingolipid species. *Biochim Biophys Acta (Bba) - Mol Cell Biol Lipids* (2016) **1861**(11):1828–39. doi:10.1016/j.bbalip.2016.08.016

41. Park JW, Park WJ, Kuperman Y, Boura-Halfon S, Pewzner-Jung Y, Futerman AH. Ablation of very long acyl chain sphingolipids causes hepatic insulin resistance in mice due to altered detergent-resistant membranes. *Hepatology* (2013) **57**(2):525–32. doi:10.1002/hep.26015

42. Hartmann D, Lucks J, Fuchs S, Schiffmann S, Schreiber Y, Ferreirós N, et al. Long chain ceramides and very long chain ceramides have opposite effects on human breast and colon cancer cell growth. *The Int J Biochem and Cell Biol* (2012) **44**(4):620–8. doi:10.1016/j.biocel.2011.12.019

43. Castell AL, Vivoli A, Tippetts TS, Frayne IR, Angeles ZE, Moullé VS, et al. Very-long-chain unsaturated sphingolipids mediate oleate-induced rat β -cell proliferation. *Diabetes* (2022) **71**(6):1218–32. doi:10.2337/db21-0640

44. Quehenberger O, Armando AM, Brown AH, Milne SB, Myers DS, Merrill AH, et al. Lipidomics reveals a remarkable diversity of lipids in human plasma. *J Lipid Res* (2010) **51**(11):3299–305. doi:10.1194/jlr.m009449

45. Chaurasia B, Tippetts TS, Mayoral Monibas R, Liu J, Li Y, Wang L, et al. Targeting a ceramide double bond improves insulin resistance and hepatic steatosis. *Science* (2019) **365**(6451):386–92. doi:10.1126/science.aav3722



OPEN ACCESS

*CORRESPONDENCE

Zhong-Zheng Zheng,
✉ zzz@catb.org.cn,
✉ shcatb@163.com

[†]These authors have contributed equally to this work and share first authorship

RECEIVED 26 July 2023

ACCEPTED 02 April 2025

PUBLISHED 11 July 2025

CITATION

Zhang L-L, Wang Z, Zhou Y, Li D-Y, Tu X-N, Li Y-X, Du K-M and Zheng Z-Z (2025) An innovative full-size pathogenic tandem duplication mutation precise detection system based on next-generation sequencing. *Exp. Biol. Med.* 250:10128. doi: 10.3389/ebm.2025.10128

COPYRIGHT

© 2025 Zhang, Wang, Zhou, Li, Tu, Li, Du and Zheng. This is an open-access article distributed under the terms of the [Creative Commons Attribution License \(CC BY\)](https://creativecommons.org/licenses/by/4.0/). The use, distribution or reproduction in other forums is permitted, provided the original author(s) and the copyright owner(s) are credited and that the original publication in this journal is cited, in accordance with accepted academic practice. No use, distribution or reproduction is permitted which does not comply with these terms.

An innovative full-size pathogenic tandem duplication mutation precise detection system based on next-generation sequencing

Li-Li Zhang[†], Zhe Wang[†], Ying Zhou, Dai-Yang Li, Xiao-Nian Tu, Yu-Xia Li, Ke-Ming Du and Zhong-Zheng Zheng*

Shanghai Tissuebank Biotechnology Co., Ltd., Shanghai, China

Abstract

Accurate identifying internal tandem duplication (ITD) mutation is indispensable for diagnosis and prognosis of acute myeloid leukemia (AML) patients, but specialized full-size detection tools are lacking. Therefore, we aimed to develop a reliable system for accurate assessment of ITD mutations of various size ranges and improve prognosis for AML. Bone marrow samples from AML patients from December 2021 to March 2022 were collected for methodology establishment. After a large-scale sample testing by next-generation sequencing (NGS), a short-read tandem duplication recognition system based on soft-clip was established. During performance validation, the lower detection limit was set to a parameter close to capillary electrophoresis ("gold standard") by adjusting reference values (sensitivity 3–5%). Data simulation was performed using the FLT3 gene CDS as wild-type data. Methodological concordance of this system with capillary electrophoresis was analyzed. The applicability to other pathogenic tandem duplication mutations was validated. We have developed an innovative NGS-based system named "ITDFinder" for accurate detection of ITD mutations, with the lower detection limit of 4%, corresponding to a sequencing depth of 1000X. Compared to capillary electrophoresis, ITDFinder exhibited good consistency (mean difference: −0.0085) in mutation detection and correlation across various length of ITD. Clinical case validation (n = 1,032) showed an overall agreement rate of 96.5% between the two approaches used for characterization. In addition, data simulation results suggested that the new system could observe BCOR-ITD and KMT2A-PTD mutations (depths, 500–1300X; mutation rates, 0.04–0.8). The innovative mutation detection system is appropriate to small-to large-sized ITDs and other pathogenic tandem duplication mutations, expected

to save 96.3% of the workload. This offers significant potential for accurate clinical assessment of ITD mutations and subsequent prognosis in AML patients.

KEYWORDS

internal tandem duplication, next-generation sequencing, acute myeloid leukemia, prognosis, mutation detection

Impact statement

We developed a new NGS-based pathogenic tandem repeat mutation precision detection system named “ITDFinder” that goes beyond capillary electrophoresis and towards multi-sized mutation length. NGS enables identification of single nucleotide mutations and gene mutations with lower detection limits and provides more objective quantification of FLT3-ITD allele load, with the advantages of short run time, low testing cost for large-scale samples, and flexible library preparation and analysis strategies to address the challenges of challenging genomic fractions. The ITDFinder system has two key advantages: first, the negative results from this ITDFinder system can be approximately equivalent to negative capillary electrophoresis results, eliminating the need for capillary electrophoresis experiments (nearly 97% of these samples based on high-volume sample validation) and shortening the NGS experimental cycle. The ITDFinder system can also accurately detect tandem repeat mutation ratios in other disorders, such as BCOR-ITD and KMT2A-PTD.

Introduction

Acute myeloid leukemia (AML) is a common malignant hematologic neoplasm caused by complementary functional pathogenic gene mutations leading to uncontrolled proliferation and maturation arrest of bone marrow progenitor cells. The FMS-like tyrosine kinase 3 (FLT3)-internal tandem duplication (ITD) is one of the most frequent mutations in AML (up to 25–30% mutation rate [1, 2]). Selection of resistant FLT3 clones, avoidance of FLT3 inhibition, or insufficient therapeutic response all contribute to FLT3-ITD persistence [3, 4]. Genetic aberrations permit accurate categorization with hazard evaluation in 50–55% of AML cases [5]. Therefore, accurate identification and mutation assessment of AML-causing genes such as ITD is indispensable for the diagnosis, treatment and prognosis of patients.

The “gold standard” for quantifying ITD mutations in clinical practice has been viewed as capillary electrophoresis [6], but it solely provides data on mutation frequency and sequence length, not other ITD-related information like the precise sequence of the insertion or the location of the insertion in the gene. Only complementary validation by

Sanger sequencing could further acquire the information mentioned above, but due to its own constraints, Sanger sequencing is much less sensitive to detect low frequency variations of ITD [7].

Modern advances in next-generation sequencing (NGS) have made it viable to realize FLT3-ITD at single-nucleotide resolution, successfully overcoming the drawbacks of conventional approaches, and minimizing the time and resource waste associated with nonsense mutation detection [8, 9]. However, barriers of NGS in detecting large ITDs and accurately reporting ITD frequencies have been reported. Furthermore, existing methods for identifying insertions and deletions (indels) (e.g., Pindel) can detect small-to medium-sized ITDs, whereas large-sized ITDs (>100 bp) are frequently detected by tools designed to detect structural variations (SVs) [8]. Clearly, tools specifically designed for ITD detection and accurate reporting across the entire size range are lacking.

Hence, in order to develop a reliable tool for accurate clinical assessment of ITD mutations in AML patients of various size ranges and improve prognosis, this study set out to develop a novel NGS-based ITD mutation detection system named “ITDFinder” to achieve rapid detection of small-to large-sized ITDs. The ITDFinder system would also provide comprehensive information including accurate quantification, insertion length, and insertion location.

Materials and methods

Sample source

Bone marrow samples from AML patients at the time of initial diagnosis from December 2021 to March 2022 were collected and sent to Shanghai Tissuebank Biotechnology Co., Ltd (China) for high-throughput screening of genes related to hematological disorders for testing the performance of the newly established system. The study was approved by the local ethics committee. All participants signed an informed consent form.

NGS flow

Each sample was first captured in a certain amount of DNA using a stacked probe, followed by NGS library construction sequencing as previously reported [10]. Then, quality control

filtering was performed on each input sample using Fastq (v0.19.5, parameter `-c-q30`), after which the reads were mapped to the human reference genome hg19 using the Burrows-Wheeler Alignment (BWA) tool v0.7.17, and the output SAM file was compressed, sorted, and indexed through SAMtools v1.10 [11–13]. Finally, software analysis was performed as follows: the obtained BAM file was partially aligned to FLT3 exons 14–15 (1787–2024 in ENST00000241453, 1705–1942 in coding sequence [CDS]) of the soft-clip (SC) reads. Each SC was classified according to its position at the beginning (sSC) or end (eSC) of the alignment region [13–15], and then aligned returned to the target region using local alignment, with the obtained terminal position acting as the anchor of the reads and those scoring <50% discarded. The section enclosed by the alignment position given by BWA and the local alignment was the ITD candidate position determined by means of the reads.

Dilution method

To analyze the presence of FLT3-ITD mutations, DNA and cDNA samples were subjected to fragment analysis using PCR followed by capillary electrophoresis. Based on the capillary electrophoresis results from patient samples, DNA extracted from the K562 cell line, which is known to lack the FLT3-ITD mutation, was used to dilute the patient samples. This created a series of diluted samples with varying ITD proportions. For the detection of FLT3-ITD mutations, nested PCR was performed on the prepared DNA and cDNA samples. The first round of PCR was followed by a second round of nested PCR, which enhances the sensitivity and specificity of the detection. The PCR products were then analyzed by capillary electrophoresis to determine the presence and size of the ITD mutations. PCR products containing the FLT3-ITD mutations were selected for library preparation. Libraries were constructed according to the manufacturer's protocol and sequenced using a high-throughput next-generation sequencing platform (e.g., Illumina).

Establishment of a SC-based short-read tandem duplication recognition system

Considering that SC is a prominent feature for the occurrence of short-read tandem duplication, we first located the position of ITD on the genome starting from SC [16].

Statistics of SC in alignment files

The BAM file records the alignment results between offline reads and reference genomes. When aligning the reads with the

reference genome, if one end of the reads mismatched with the reference genome, it was recorded as a SC in the BAM file. Information on the reads where SCs occurred in the alignment records and their corresponding positions to the reference genome were collected.

Positioning the beginning and end of ITD

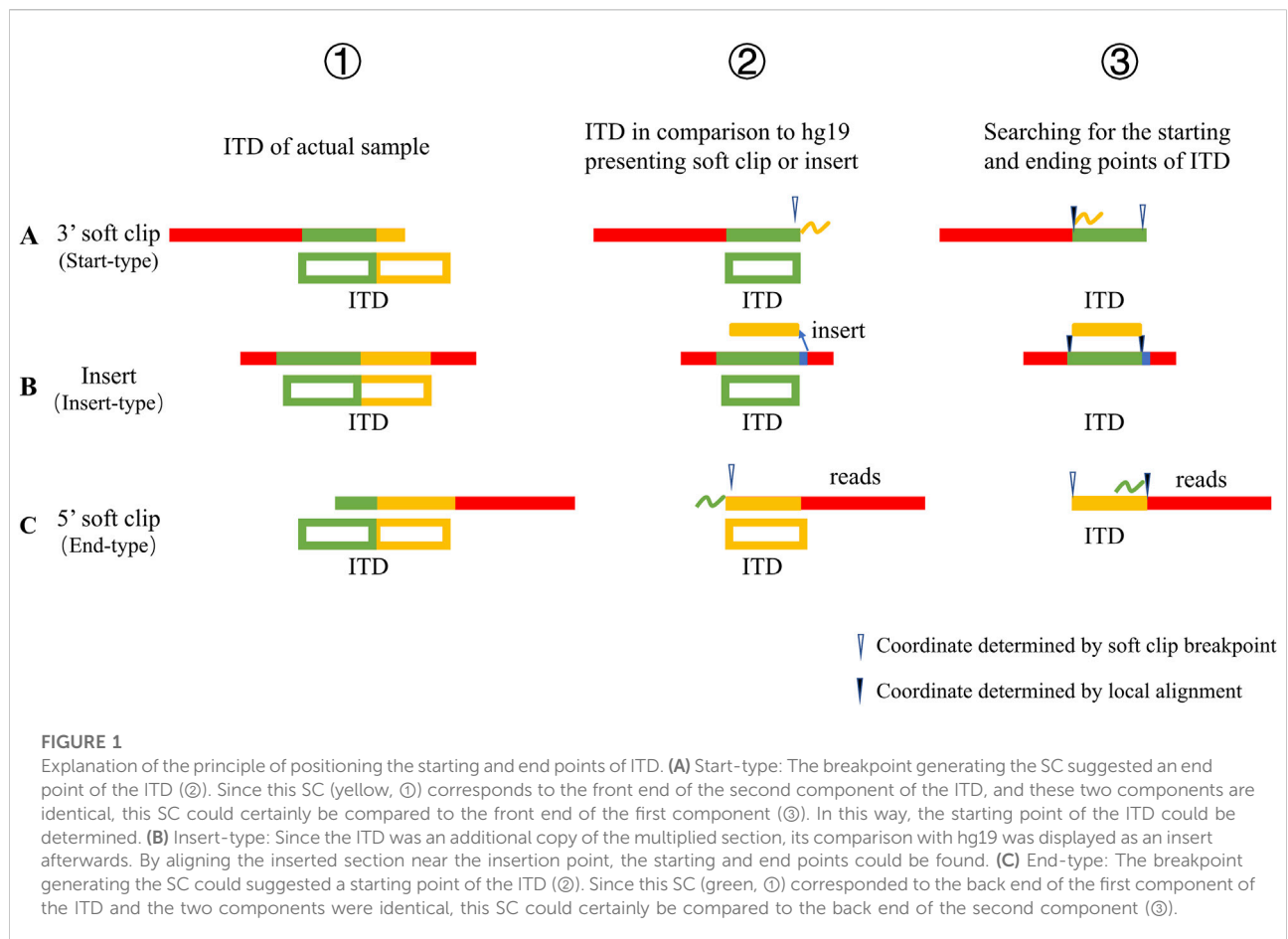
The reads were randomly covered to each position of the ITD, and for the reads falling on the junction of two components of the ITD, a SC could be formed by comparison with hg19; for the reads completely covered to both components of the ITD, an insert could be formed by comparison with hg19. The three specific types of ITDs were composed of Start-type (Figure 1A), Insert-type (Figure 1B), and End-type (Figure 1C). In this way, the end point of the ITD could be determined.

Determination of the starting and end points of ITDs

In accordance with experimental principles, each reads was known to determine the starting and end points of an ITD, that is, this ITD could be regarded as a candidate ITD, and the corresponding reads could be considered evidence of a candidate ITD. After filtering all candidate ITDs, the number of reads each candidate ITD owned was calculated, and the authenticity of the ITD was judged by the number of reads. If there were more than two different types of reads pointing to the same ITD, the likelihood of the position being a true ITD was high. The matches produced due to chance sequence similarity, often with only one-sided evidence, were recorded as “only start” or “only end” in the result file.

Initial parameter adjustment settings

After large-scale sample testing, the following initial parameters (thresholds) were chosen to maintain appropriate sensitivity and specificity during alignment: *min_sc_length*, if the SC or insertion was below the value, then the subsequent alignment was excluded; the penalty points for *gap_open* and *gap_extend*, respectively, in the alignment; *min_score_ratio* and *min_sc_aln_length*, respectively, representing the alignment quality and length filtering threshold. Parameters of the output included: *base_level_num*, which was used to screen for low-support ITDs and then pair different types of evidence-based candidate ITDs; *prominent_level*, defined as high confidence positive if above this threshold; and *uncertain_threshold*, a candidate ITD supported only by unilateral evidence that was not lower than this threshold was classified as such, otherwise it was classified as negative.



Output results

The results satisfying the set parameters (thresholds) were output according to the logic, as shown in Figure 2.

Performance validation

The performance validation of the detection method was conducted by evaluating its sensitivity and accuracy in identifying tandem duplications within a simulated dataset. We established the lower detection limit by modifying the reference values to align with the performance of capillary electrophoresis, setting a sensitivity threshold between 3% and 5% (median 4%) based upon previous studies. [17]. Data simulation was conducted via the dwgsim program (version 0.1.11). The CDS of the FLT3 gene (ENST00000241453) served as the wild-type reference sequence. The CDS encompasses nucleotide locations 1705–1942, and a tandem duplication was modelled by introducing a piece of variable length (5–70 base pairs) at a fixed location inside the FLT3 CDS (position 1610) of the hg19 reference genome. This facilitated the creation of simulated short-read tandem duplication mutations of varying durations. The simulation was regulated with

the -c parameter in dwgsim, which specifies the sequencing depth. A coverage range of 900X to 1300X was applied to the simulated data, and the impact of varied mutation rates was analyzed by combining variable fractions of wild-type and mutant reads. The simulation outcomes, displayed as combinations of wild-type and mutant reads, facilitated the evaluation of detection capabilities at various mutation frequencies and sequencing depths. This method validated the system's capacity to identify tandem duplications with excellent sensitivity, even at reduced mutation rates.

Validation of the applicability to other pathogenic tandem duplication mutations

To evaluate the system's efficacy regarding additional harmful tandem duplication mutations beyond FLT3-ITD, we concentrated on haematologic malignancies and a range of tumour types. Utilising previously validated BCOR-ITD sequences for clear cell sarcoma of the kidney (CCSK), we produced simulated data for four sequence types employing dwgsim v0.1.11 software [18]. We investigated histone-lysine N-methyltransferase 2A (KMT2A)-partial tandem duplication (PTD) as a prospective therapeutic target and biomarker for

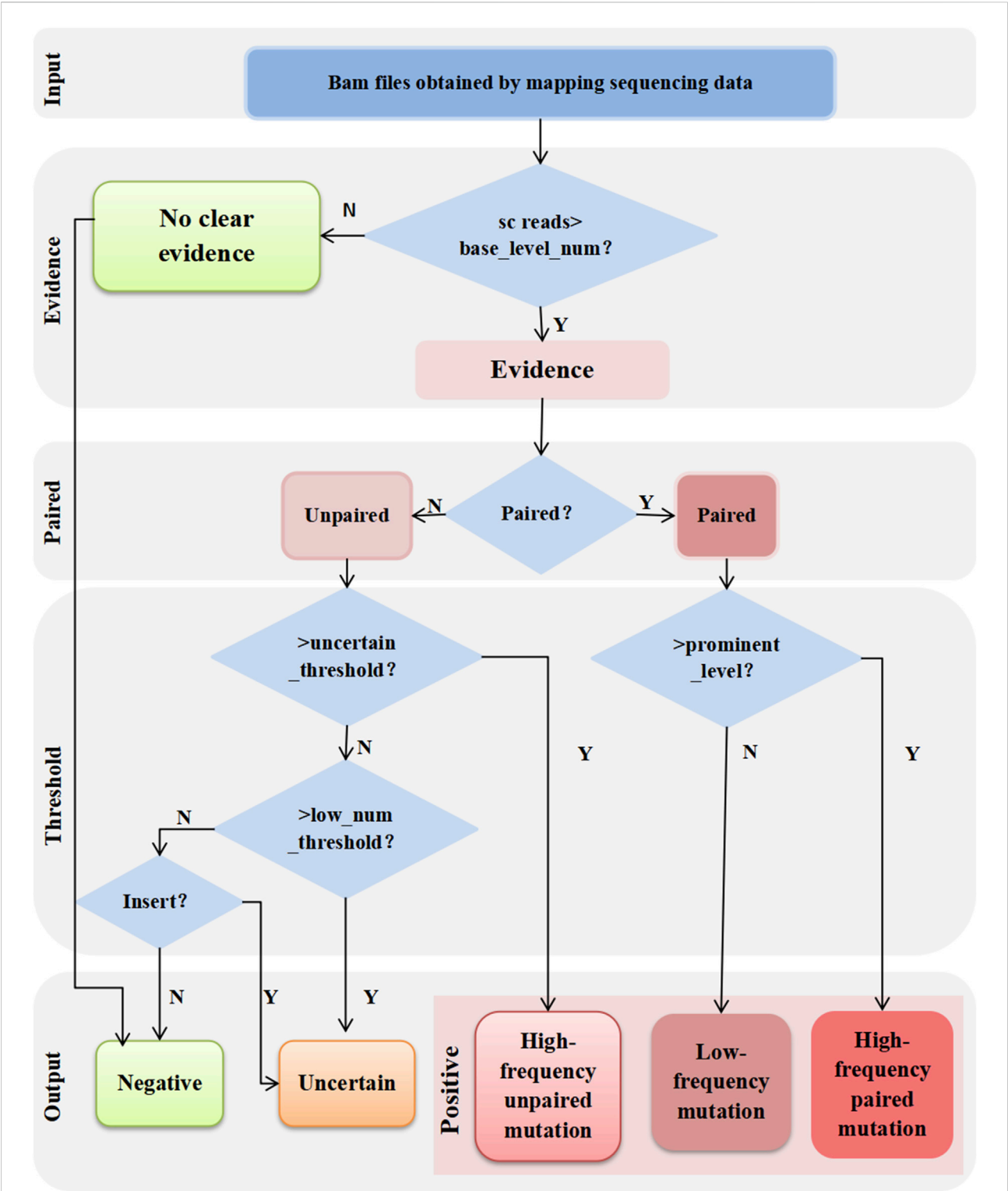


FIGURE 2
Output results logic diagram. Candidate ITDs with the number of supported reads below the threshold of *base_level_num* are filtered out. Those above the threshold of *base_level_num* are paired with supporting evidence to see which candidate ITDs are supported by multiple types of evidence. Candidate ITDs that are supported by multiple types of evidence are output as positive, while those that cannot be paired are considered as ITDs supported by only unilateral evidence. For ITDs supported by unilateral evidence only, if it meets the threshold of *uncertain_threshold*, the output is positive or indeterminate according to whether it meets the threshold of *prominent_level* for capillary electrophoresis verification; those below the threshold of *uncertain_threshold* are judged as indeterminate if they are insert type, otherwise they are judged as negative.

minimum residual disease in acute myeloid leukaemia (AML) and myelodysplastic syndrome (MDS). [19]. A recent investigation yielded 25 clinically validated KMT2A-PTD sequences, from which four were randomly selected for the creation of simulation data. We established varying sequencing depths for each sequence class, specifying mutation rates for each gradient. Each simulation was conducted five times to verify reliability. This methodology illustrates the system's wider application to other pathogenic tandem duplications, hence augmenting its utility in clinical contexts.

Statistical analysis

Count data were described using absolute frequencies and percentages. Bland-Altman plots, scatter plots and mosaics were generated to analyze the methodological agreement of this new system with capillary electrophoresis. All statistical analyses were performed with GraphPad Prism 8 and R (4.2.0) software.

Results

Presentation form of the new system

We developed an innovative NGS-based system named "ITDFinder" for accurate detection of pathogenic tandem duplication mutations. The presentation of tandem duplication region reads in positive samples in Integrative Genomics Viewer is shown in Figure 3A. In addition, a FLT3-ITD had multiple mutation items with consecutive insertion positions. An example of the output file for positive sample results reported by the ITDFinder system was displayed in Figure 3.

Performance evaluation of the new system

Lower detection limit

When the mutation rate of the test samples was below 4%, some of the samples were not detected (marked in red), whilst the mutation rate above 4% could be detected, thus the lower detection limit of the system was 4%, corresponding to a sequencing depth of 1000X (Table 1).

Methodological consistency comparison

The mean difference between the mutation rate detection results of the ITDFinder system and capillary electrophoresis was -0.0085 (range, -0.1835 to 0.1644), indicating that ITDFinder was in good consistency with capillary electrophoresis and feasible for ITD

quantification (Figure 4A). In addition, there was a good correlation between the length of ITDFinder and capillary electrophoresis, indicating that ITDFinder has the ability to detect multiple sizes of ITDs (Figure 4B).

Clinical case validation

Among the 1,032 clinical samples used for validation, 51 samples (4.94%) were completely consistent with the positive capillary electrophoresis validation by the ITDFinder system, all of which were positive. Of the remaining samples with negative capillary electrophoresis verification results ($n = 981$), 96.3% were recognized as negative by ITDFinder, with the two methods in agreement; 3.4% were identified as positive by ITDFinder, contradicting the capillary electrophoresis verification results; and the remaining 0.3% were inconclusive (Table 2). Thus, the overall agreement rate between the two approaches used for characterization was 96.5%. It was assumed that the both ways are equivalent in most cases of determination, but the ITDFinder system can additionally identify positive mutation cases that cannot be measured by means of capillary electrophoresis.

The above results also indicated that ITDFinder was expected to save 96.3% of the workload (i.e., its determination results were used directly without capillary electrophoresis verification), while the remaining 3.7% of the samples were categorized as negative for capillary electrophoresis verification (meaningless retest).

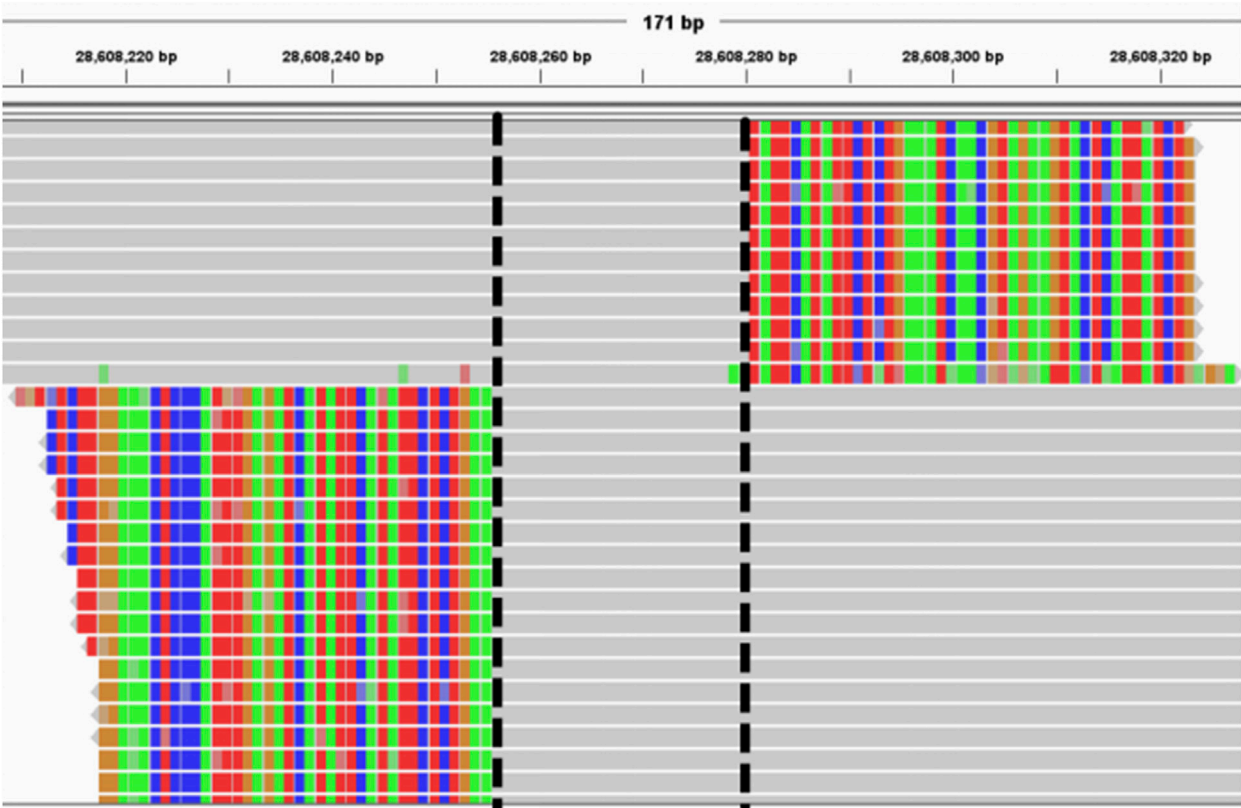
Validation of the applicability of the new system to BCOR-ITD and KMT2A-PTD

Using clinically validated typical ITD mutations in hematologic and non-hematologic diseases that have been mentioned as simulation objects, the above ITD sequences were made into simulation data and used to verify the applicability of the ITDFinder system to ITDs other than FLT3-ITD. Based on the data simulation results, ITDFinder can observe BCOR-ITD (Figure 5) and KMT2A-PTD mutations (Figure 6) with mutation depths in the vary of 500–1300X and mutation rates in the range of 0.04–0.8. Together with the aforementioned results, they collectively demonstrated that ITDFinder is a reliable tool specifically for ITD detection, not only for full-sized ITD mutations including FLT3-ITD, but also for mutations with longer sequences (e.g., PTD).

Discussion

In the present study, we developed an innovative NGS-based pathogenic tandem duplication mutation precision detection system, called as "ITDFinder", beyond capillary electrophoresis and towards multi-sized mutation length.

(A)



(B)

Samplename	Chr	Pos	Length	Description	Start count	End count	Insert count	Total count
S1_23	chr13	28608256	23	paired-all	76	72	88	236
S1_73	chr13	28608228	73	paired_start_end	81	77	0	158
S1_104	chr13	28608209	104	paired_start_end	19	25	0	44
S1_55	chr13	28608218	55	paired_start_end	22	19	0	41

FIGURE 3
Example of redundant FLT3-ITD lists generated by the new system. **(A)** Integrative Genomics Viewer screenshot of a positive sample (FLT3-ITD of 20 bp at chr13: 28,608,256–28,608,276). Reads covering ITD are marked as colored SC. The colored strips on either side of the dashed line represent the SC segments, and the part between the two dashed lines represents the short-read tandem duplication region. The black dotted line represents the left and right breakpoints formed by aligning these reads to the reference genome, and the sequences between the two breakpoints represent the duplicated fragments. **(B)** FLT3-ITD lists detected by the new system. Terms in the header are explained as follows: *chr* represents the chromosome name; *pos* represents absolute chromosome position; *length ITD* represents the length of ITD; *description* represents the type of reads supporting this ITD; *start count* represents the count of Start-type reads; *end count* represents the count of End-type reads; *insert count* represents the count of Insert-type reads; and *total count* represents the total number of reads supporting this ITD.

TABLE 1 Validation results of the lower detection limit of this new system.

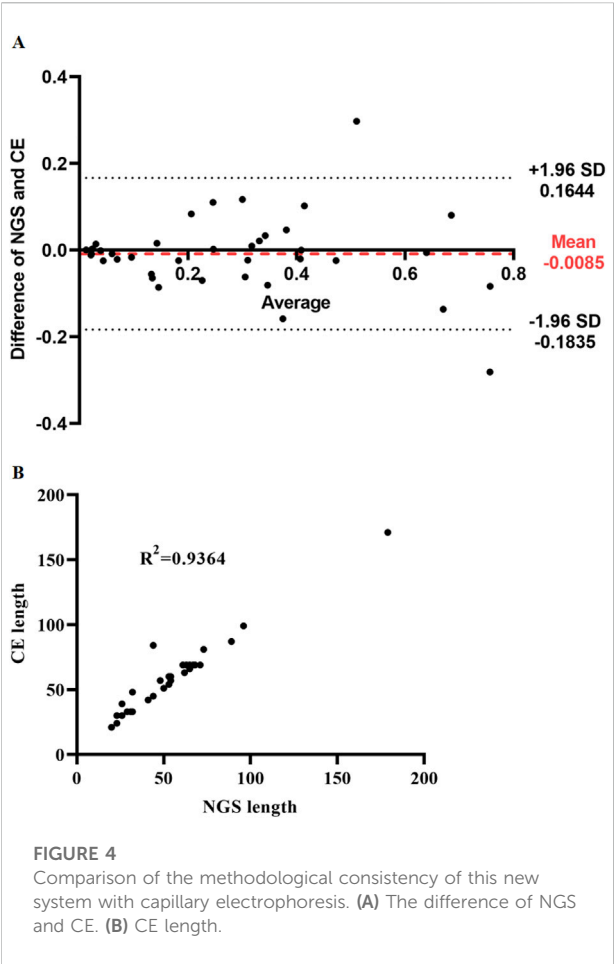
ITD length	Simulated sequencing depth (X)	Mutation rate (%)					
		2	4	6	8	10	20
5	900	19	37	34	71	99	163
	1100	26	45	61	76	80	209
	1300	24	55	66	96	113	220
10	900	15	31	43	66	53	150
	1100	13	29	49	83	78	203
	1300	25	44	66	80	103	249
20	900	Below threshold	22	45	65	68	167
	1100	16	35	34	75	100	213
	1300	17	42	63	91	123	246
30	900	Below threshold	27	46	65	57	164
	1100	15	37	59	94	96	209
	1300	Below threshold	42	71	86	119	252
40	900	Below threshold	14	38	65	92	172
	1100	Below threshold	33	59	72	100	208
	1300	Below threshold	39	63	92	121	225
50	900	22	33	31	57	89	165
	1100	11	42	56	71	87	218
	1300	13	48	70	107	120	222
60	900	12	34	43	69	88	155
	1100	Below threshold	29	64	83	99	215
	1300	12	49	75	98	121	213
70	900	Below threshold	30	52	56	81	195
	1100	17	38	58	81	105	204
	1300	13	49	82	87	124	237

Since AML with FLT3-ITD mutations yields a high prevalence, rapid relapse rate, and generally poor prognosis, their early identification does have a considerable potential to ameliorate the aforementioned events [20–23]. Furthermore, ITD is the most common type of FLT3 mutation in AML patients, raising the bar for understanding FLT3-ITD and, by extension, AML pathogenesis [24].

Given the nature of heterogeneity, routine AML screening relies on a variety of technical equipment at the cytogenetic and molecular levels. NGS technology, amongst others, obtains and validates results comparable to many conventional molecular and cytogenetic analyses by means of inspecting the giant quantity of genomic information obtained in a single assay with extensive use of multiple bioinformatics algorithms [25].

Compared with regular capillary electrophoresis, NGS allows the identification of single nucleotide and gene mutations with lower detection limits and presents more objective FLT3-ITD allele load quantification, with the benefits of short running time, low fee of large-scale pattern detection, and flexible library preparation and analysis strategies to tackle the challenges of difficult-to-sequence genomic fractions [26, 27]. In this study, FLT3-ITD was detected based on NGS, which could assist apprehend the genetic mutation composition of AML, in turn guide the classification of AML by mutation, and is expected to more accurately combine FLT3-ITD with adverse prognosis in AML patients [5].

The sequence and length of ITD mutations are heterogeneous and vary by patient. Research has shown that



longer ITD in patients with positive FLT3-ITD mutations is associated with shorter overall survival and relapse-free survival [28]. Current study found a poor correlation between risk and high mutation load in the FLT3-ITD mutation subgroup [29]. In contrast, the existing detection tools suffer from poor accuracy, inapplicable to low-frequency variants, and unable to notice larger ITD frequencies. FLT3-ITD detection by NGS is challenging primarily because standard bioinformatics algorithms are not optimized for large insertion/deletion (>20 bp) detection. Upon optimization and validation, the NGS system was found to be 100% consistent in detecting FLT3-ITD in presence of variable size (3–231 bp) and insertion sites [6]. Due to the dependence of small- and large-sized ITDs on the detection of insertion and structural mutations, neither of them could be achieved with currently available software [5]. Hence, in order to settle these issues, ITDFinder for accurate detection of FLT3-ITD mutations was created, based on the NGS data collected from existing AML samples, which can rapidly detect full-size ITD mutations, and negative results can be directly used as a reference after comparison with capillary electrophoresis. According to reports, an increase in the

TABLE 2 Comparison of the qualitative results of this new system with capillary electrophoresis for clinical samples.

		Capillary electrophoresis (CE)				Total
		Positive		Negative		
		N	%	N	%	
New system	Positive	51	100%	33 (FP)	3.4% (FPR)	84
	Negative	-	-	945	96.3%	945
	Uncertain	-	-	3	0.3%	3
Total		51	100%	981	100%	1032

FP, false positive; FPR, false positive rate.

frequency of FLT3-ITD mutations in refractory AML predicted a decrease in complete remission rate and overall survival rate after relapse [30]. Therefore, precise detection of ITD mutations using NGS may provide a basis for studying the molecular mechanisms of refractory or relapsed leukemia, and open up a new perspective for dynamic risk assessment of AML. Notably, both FLT3-ITD and KMT2A-PTD in AML patients involve the adverse outcome-related molecular features [31]. Recent evidence emphasizes that considering KMT2A-PTD mutations as a potential adverse prognostic factor for AML patients [32]. Therefore, we confirmed the performance of the ITDFinder system for the detection of other types of ITD (i.e., BCOR-ITD) and PTD (i.e., KMT2A-PTD) through simulated data.

Importantly, by comparing eight available and most representative software platforms for detecting FLT3-ITD (Table 3) [9, 33–40], it is not difficult to see that the shortcomings of the above tools can be addressed through our tool ITDFinder. Specifically, ITDFinder has the ability to accurately determine the percentage of tandem repeat mutations in multiple diseases, not limited to AML. In addition, it can quickly identify both large and small ITD mutations; its short runtime allows it to identify full-sized ITD mutations, such as FLT3-ITD.

Overall, ITDFinder has two significant advantages. First, negative results achieved with ITDFinder are roughly equivalent to negative capillary electrophoresis results, thereby removing the necessity for capillary electrophoresis experiments (almost 97% of samples based on high volume validation) and shortening NGS cycle times. Additionally, as a system specifically designed for ITD detection, it is additionally appropriate for accurate detection of tandem duplication mutation ratios in different diseases, which includes BCOR-ITD and KMT2A-PTD. The former is essential for the diagnosis and therapeutic strategy of CCSK [18]; and the latter is valuable as an AML causative gene in the

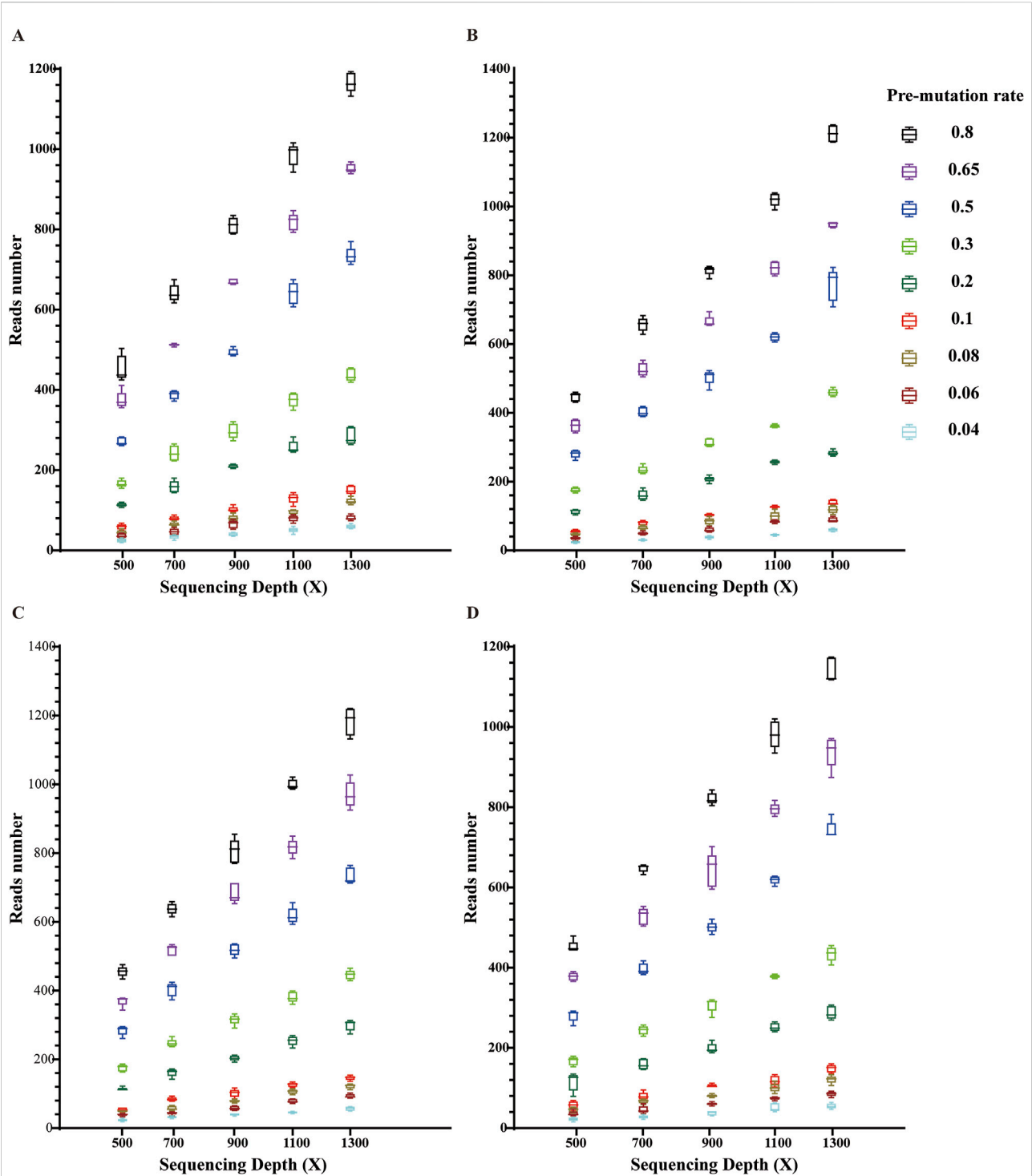


FIGURE 5
Validation of the applicability of this new system in BCOR-ITD mutation detection. Each box indicates each repetition; different colors indicate different preset mutation frequencies in the range of 0.04–0.8. (A) Reptition 1, (B) Reptition 2, (C) Reptition 3, (D) Reptition 4.

dynamic monitoring of tumor burden and can be used as one of the markers of disease onset, progression and clonal evolution [37, 41].

The limitation of the ITDFinder system is that it cannot fundamentally improve the limitation of the NGS technology’s filtering operation, which may change the ratio of normal reads

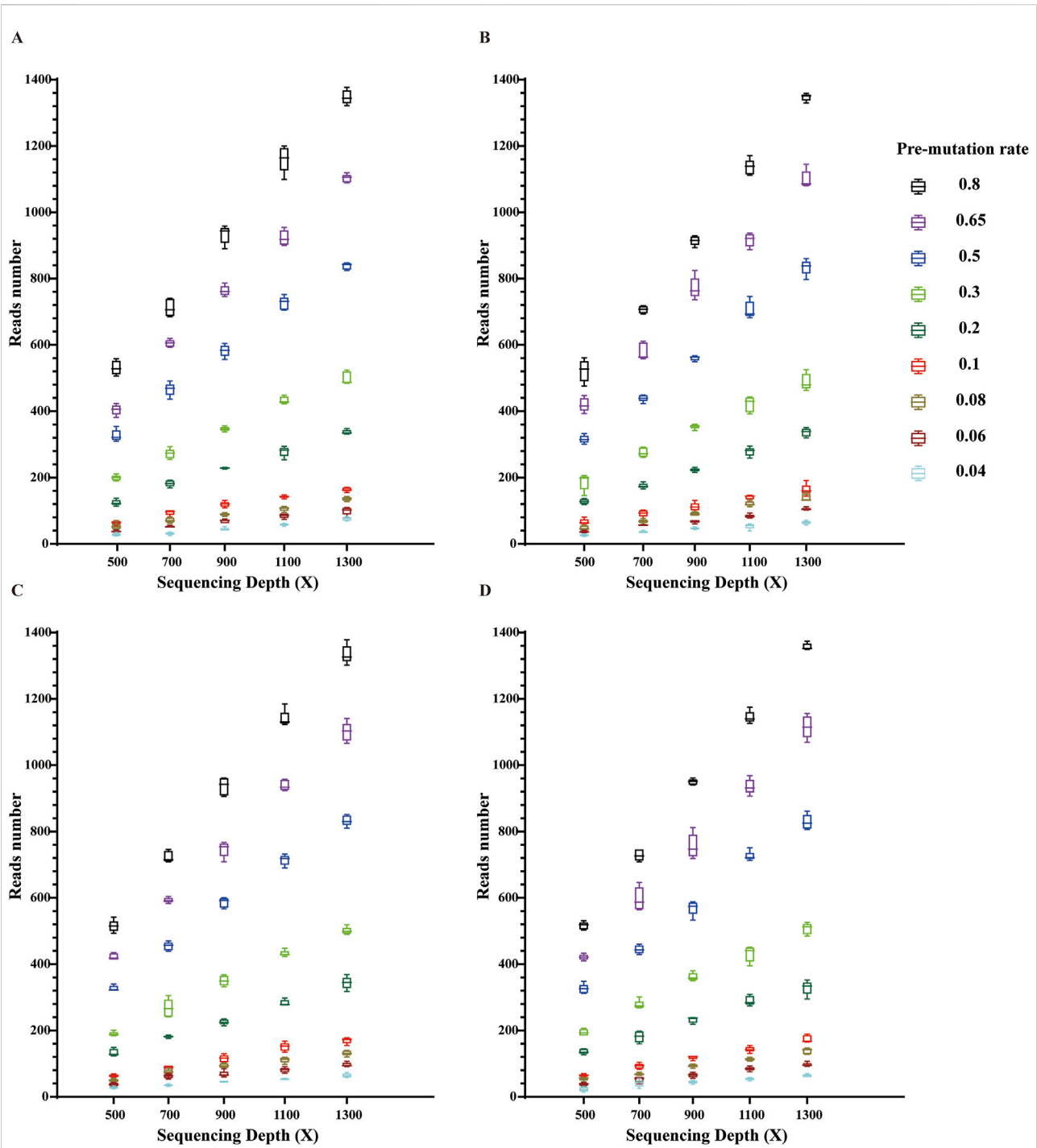


FIGURE 6 Validation of the applicability of this new system in KMT2A-PTD mutation detection. Each box indicates each repetition; different colors indicate different preset mutation frequencies in the range of 0.04–0.8. (A) Reptition 1, (B) Reptition 2, (C) Reptition 3, (D) Reptition 4.

to wild-type reads, often leading to uncontrollable errors in the results, ambiguous judgments on the normal or mutant type of reads [42], leaving its ability to calculate accurately to be

improved. Further and substantial advancements in this field may be achieved in the future by attempting to utilise approaches such as triple sequencing [42].

TABLE 3 Representative software programs for detecting FLT3-ITD.

Tool	Theory	Strength	Limitation
Pindel [33]	Split-read strategy using a pattern growth algorithm	- Ability to detect breakpoints of large deletions and medium-sized insertions from paired-end short reads - Ability to detect short (10–200 bp) tandem duplications and structural variants	- Low frequency of detected mutations
ITDDetector [34]	Assembly strategy	- effective avoidance of deviations caused by alignment errors	- Inability to detect ITDs with more than two duplicates - Only for somatic ITD detection, not for germline detection
ITDseek [35]	Soft-clipping with the alignment information	- Reporting all insertions of FLT3 exons 14 and 15 in the result as itds - Dependent on the -M parameter of BWA-MEM to mark shorter split hits as secondary	- Lack of research or evaluation on unreported hybridization capture sequencing data - Inability to differentiate shorter insertions and tandem repeats
getITD [36]	High-quality sequencing reads aligning to the reference genome to identify insertions	- Detecting and fully annotating all tested itds - Achieving 100% sensitivity and specificity	- Inability to parse large files, requiring manual extraction of reads in a certain region - The upper limit of detected ITD length affected by sequencing data length
ScanITD [37]	Soft-clipping with the alignment information	- The string rotation method, distinguishing between insertions of new sequences and duplications of genome sequences	- Inability to detect complex types of FLT3-ITD
FLT3_ITD_ext [38]	Central clustering-based greedy algorithm SUMACLUSt	- Ability to effectively solve the shortcomings of existing methods that underestimate mutation frequency	- Inability to identify large, purely non-templated insertions
ABRA2 [39]	Assembly strategy	- Good performance on short Indels and FLT3 ITDs with <100 bases	- Significantly delay in result generation, owing to the increased processing time caused by compute resource
FiLT3r [9]	k-mers	- Ability to detect duplications in any gene once the reference sequence is known - More precise (neither false-positive nor false-negative)	- Inability to detect duplications that would occur at the beginning or end of a read

Conclusion

The ITDFinder system for accurate detection of pathogenic tandem duplication mutations is equivalent to capillary electrophoresis assays in most cases of determination and can additionally identify positive mutation cases that cannot be measured by the assay, saving 96.3% of the workload. ITDFinder is capable of detecting not only full-size ITD mutations including FLT3-ITD, but also PTD mutations, and offers significant potential for accurate clinical assessment of ITD mutations in AML patients, predicting prognostic risk, and optimizing therapy options.

Author contributions

Project Implementation and Editing: ZW; Information Collection: L-LZ; Literature Review: L-LZ; Manuscript Writing: L-LZ and YZ; Manuscript Review and Editing: D-YL;

Data Supervision: X-NT; Data Visualization: Y-XL; Supervising: K-MD; Correspondence: Z-ZZ; All authors contributed to the article and approved the submitted version.

Data availability

The original contributions presented in the study are included in the article/supplementary material, further inquiries can be directed to the corresponding author.

Ethics statement

The studies involving humans were approved by the Ethics Committee of Shanghai Tissuebank Medical Laboratory. The studies were conducted in accordance with the local legislation and institutional requirements. The participants provided their written informed consent to participate in this study.

Funding

The author(s) declare that no financial support was received for the research and/or publication of this article.

References

- Zhao J, Song Y, Liu D. Gilteritinib: a novel FLT3 inhibitor for acute myeloid leukemia. *Biomark Res* (2019) 7:19. doi:10.1186/s40364-019-0170-2
- Bjelosevic S, Gruber E, Newbold A, Shembrey C, Devlin JR, Hogg SJ, et al. Serine biosynthesis is a metabolic vulnerability in FLT3-ITD-driven acute myeloid leukemia. *Cancer Discov* (2021) 11:1582–99. doi:10.1158/2159-8290.cd-20-0738
- Arindrarto W, Borrás DM, de Groen R, van den Berg RR, Locher IJ, van Diessen S, et al. Comprehensive diagnostics of acute myeloid leukemia by whole transcriptome RNA sequencing. *Leukemia* (2021) 35:47–61. doi:10.1038/s41375-020-0762-8
- Schmalbrock L K, Dolnik A, Cocciardi S, Strang E, Theis F, Jahn N, et al. Clonal evolution of acute myeloid leukemia with FLT3-ITD mutation under treatment with midostaurin. *Blood* (2021) 137:3093–104. doi:10.1182/blood.202007626
- He R, Devine DJ, Tu ZJ, Mai M, Chen D, Nguyen PL, et al. Hybridization capture-based next generation sequencing reliably detects FLT3 mutations and classifies FLT3-internal tandem duplication allelic ratio in acute myeloid leukemia: a comparative study to standard fragment analysis. *Mod Pathol* (2020) 33:334–43. doi:10.1038/s41379-019-0359-9
- Tipu HN, Shabbir A. Evolution of DNA sequencing. *J Coll Physicians Surgeons-Pakistan : JCPSP* (2015) 25:210–5.
- Li Y, Gao G, Lin Y, Hu S, Luo Y, Wang G, et al. Pacific Biosciences assembly with Hi-C mapping generates an improved, chromosome-level genome. *Gigascience* (2020) 9:giaa114. doi:10.1093/gigascience/giaa114
- Mack E, Marquardt A, Langer D, Ross P, Ultsch A, Kiehl MG, et al. Comprehensive genetic diagnosis of acute myeloid leukemia by next-generation sequencing. *Haematologica* (2019) 104:277–87. doi:10.3324/haematol.2018.194258
- Au CH, Wa A, Ho DN, Chan TL, Ma ES. Clinical evaluation of panel testing by next-generation sequencing (NGS) for gene mutations in myeloid neoplasms. *Diagn Pathol* (2016) 11:11. doi:10.1186/s13000-016-0456-8
- Li H, Durbin R. Fast and accurate short read alignment with Burrows-Wheeler transform. *Bioinformatics* (2009) 25:1754–60. doi:10.1093/bioinformatics/btp324
- Li H, Durbin R. Fast and accurate long-read alignment with Burrows-Wheeler transform. *Bioinformatics* (2010) 26:589–95. doi:10.1093/bioinformatics/btp698
- Danecek P, Bonfield JK, Liddle J, Marshall J, Ohan V, Pollard MO, et al. Twelve years of SAMtools and BCFtools. *Gigascience* (2021) 10:giab008. doi:10.1093/gigascience/giab008
- Li H, Handsaker B, Wysoker A, Fennell T, Ruan J, Homer N, et al. The sequence alignment/map format and SAMtools. *Bioinformatics* (2009) 25:2078–9. doi:10.1093/bioinformatics/btp352
- Bonfield JK, Marshall J, Danecek P, Li H, Ohan V, Whitwham A, et al. HTSlib: C library for reading/writing high-throughput sequencing data. *Gigascience* (2021) 10:giab007. doi:10.1093/gigascience/giab007
- Hedges DJ. RNA-Seq fusion detection in clinical oncology. *Adv Exp Med Biol* (2022) 1361:163–75. doi:10.1007/978-3-030-91836-1_9
- Lyu XD, Zou Z, Peng H, Fan RH, Song YP. Application of multiple nucleotide polymorphism analysis in chimerism detection after allogeneic hematopoietic stem cell transplantation. *Zhonghua Xue Ye Xue Za Zhi* (2019) 40:662–6. doi:10.3760/cma.j.issn.0253-2727.2019.08.007
- Roy A, Kumar V, Zorman B, Fang E, Haines KM, Doddapaneni H, et al. Recurrent internal tandem duplications of BCOR in clear cell sarcoma of the kidney. *Nat Commun* (2015) 6:8891. doi:10.1038/ncomms9891
- Tsai HK, Gibson CJ, Murdock HM, Davineni P, Harris MH, Wang ES, et al. Allelic complexity of KMT2A partial tandem duplications in acute myeloid leukemia and myelodysplastic syndromes. *Blood Adv* (2022) 6:4236–40. doi:10.1182/bloodadvances.2022007613
- Bazarbachi A, Bug G, Baron F, Brissot E, Ciceri F, Dalle IA, et al. Clinical practice recommendation on hematopoietic stem cell transplantation for acute myeloid leukemia

Conflict of interest

Authors L-LZ, ZW, YZ, D-YL, X-NT, Y-XL, K-MD, and Z-ZZ were employed by Shanghai Tissuebank Biotechnology Co., Ltd.

patients with FLT3-internal tandem duplication: a position statement from the Acute Leukemia Working Party of the European Society for Blood and Marrow Transplantation. *Haematologica* (2020) 105:1507–16. doi:10.3324/haematol.2019.243410

20. Burchert A, Bug G, Fritz LV, Finke J, Stelljes M, Rolig C, et al. Sorafenib maintenance after allogeneic hematopoietic stem cell transplantation for acute myeloid leukemia with FLT3-internal tandem duplication mutation (SORMAIN). *J Clin Oncol* (2020) 38:2993–3002. doi:10.1200/jco.19.03345

21. Daver N, Schlenk RF, Russell NH, Levis MJ. Targeting FLT3 mutations in AML: review of current knowledge and evidence. *Leukemia* (2019) 33:299–312. doi:10.1038/s41375-018-0357-9

22. Rehman A, Akram AM, Chaudhary A, Sheikh N, Hussain Z, Alsanie WF, et al. RUNX1 mutation and elevated FLT3 gene expression cooperates to induce inferior prognosis in cytogenetically normal acute myeloid leukemia patients. *Saudi J Biol Sci* (2021) 28:4845–51. doi:10.1016/j.sjbs.2021.07.012

23. Borrow J, Dyer SA, Akiki S, Griffiths MJ. Terminal deoxynucleotidyl transferase promotes acute myeloid leukemia by priming FLT3-ITD replication slippage. *Blood* (2019) 134:2281–90. doi:10.1182/blood.2019001238

24. Kim B, Lee H, Jang J, Kim SJ, Lee ST, Cheong JW, et al. Targeted next generation sequencing can serve as an alternative to conventional tests in myeloid neoplasms. *Plos One* (2019) 14:e0212228. doi:10.1371/journal.pone.0212228

25. Tung JK, Suarez CJ, Chiang T, Zehnder JL, Stehr H. Accurate detection and quantification of FLT3 internal tandem duplications in clinical hybrid capture next-generation sequencing data. *The J Mol Diagn* (2021) 23:1404–13. doi:10.1016/j.jmoldx.2021.07.012

26. Akabari R, Qin D, Hussaini M. Technological advances: CEBPA and FLT3 internal tandem duplication mutations can be reliably detected by next generation sequencing. *Genes* (2022) 13:630. doi:10.3390/genes13040630

27. Engen C, Hellesoy M, Grob T, Al Hinai A, Brendehaug A, Wergeland L, et al. FLT3-ITD mutations in acute myeloid leukaemia - molecular characteristics, distribution and numerical variation. *Mol Oncol* (2021) 15:2300–17. doi:10.1002/1878-0261.12961

28. Wang M, Wang R, Wang H, Chen C, Qin J, Gao X, et al. Difference in gene mutation profile in patients with refractory/relapsed versus newly diagnosed acute myeloid leukemia based on targeted next-generation sequencing. *Leuk and Lymphoma* (2021) 62:2416–27. doi:10.1080/10428194.2021.1919661

29. Marshall A, Heide F, Fischer T, Ronnstrand L. Internal tandem duplication mutations in the tyrosine kinase domain of FLT3 display a higher oncogenic potential than the activation loop D835Y mutation. *Ann Hematol* (2018) 97:773–80. doi:10.1007/s00277-018-3245-5

30. Yamato G, Kawai T, Shiba N, Ikeda J, Hara Y, Ohki K, et al. Genome-wide DNA methylation analysis in pediatric acute myeloid leukemia. *Blood Adv* (2022) 6:3207–19. doi:10.1182/bloodadvances.2021005381

31. Antherieu G, Bidet A, Huet S, Hayette S, Migeon M, Boureau L, et al. Allogeneic stem cell transplantation abrogates negative impact on outcome of AML patients with KMT2A partial tandem duplication. *Cancers* (2021) 13:2272. doi:10.3390/cancers13092272

32. Yuan D, He X, Han X, Yang C, Liu F, Zhang S, et al. Comprehensive review and evaluation of computational methods for identifying FLT3-internal tandem duplication in acute myeloid leukaemia. *Brief Bioinform* (2021) 22:bbab099. doi:10.1093/bib/bbab099

33. Chiba K, Shiraishi Y, Nagata Y, Yoshida K, Imoto S, Ogawa S, et al. Genomon ITDetector: a tool for somatic internal tandem duplication detection from cancer genome sequencing data. *Bioinformatics* (2015) 31:116–8. doi:10.1093/bioinformatics/btu593

34. Blatte TJ, Schmalbrock LK, Skambraks S, Lux S, Cocciardi S, Dolnik A, et al. getITD for FLT3-ITD-based MRD monitoring in AML. *Leukemia* (2019) 33:2535–9. doi:10.1038/s41375-019-0483-z

35. Wang TY, Yang R. ScanITD: detecting internal tandem duplication with robust variant allele frequency estimation. *Gigascience* (2020) 9:giaa089. doi:10.1093/gigascience/giaa089

36. Craven KE, Fischer CG, Jiang L, Pallavajjala A, Lin MT, Eshleman JR. Optimizing insertion and deletion detection using next-generation sequencing in the clinical laboratory. *The J Mol Diagn* (2022) **24**:1217–31. doi:10.1016/j.jmoldx.2022.08.006
37. Tsai HK, Brackett DG, Szeto D, Frazier R, MacLeay A, Davineni P, et al. Targeted informatics for optimal detection, characterization, and quantification of FLT3 internal tandem duplications across multiple next-generation sequencing platforms. *The J Mol Diagn* (2020) **22**:1162–78. doi:10.1016/j.jmoldx.2020.06.006
38. Kim JJ, Lee KS, Lee TG, Lee S, Shin S, Lee ST. A comparative study of next-generation sequencing and fragment analysis for the detection and allelic ratio determination of FLT3 internal tandem duplication. *Diagn Pathol* (2022) **17**:14. doi:10.1186/s13000-022-01202-x
39. Mohammad NS, Nazli R, Zafar H, Fatima S. Effects of lipid based Multiple Micronutrients Supplement on the birth outcome of underweight pre-eclamptic women: a randomized clinical trial. *Pak J Med Sci* (2022) **38**:219–26. doi:10.12669/pjms.38.1.4396
40. Ye K, Schulz MH, Long Q, Apweiler R, Ning Z. Pindel: a pattern growth approach to detect break points of large deletions and medium sized insertions from paired-end short reads. *Bioinformatics* (2009) **25**:2865–71. doi:10.1093/bioinformatics/btp394
41. Dai B, Yu H, Ma T, Lei Y, Wang J, Zhang Y, et al. The application of targeted RNA sequencing for KMT2A-partial tandem duplication identification and integrated analysis of molecular characterization in acute myeloid leukemia. *The J Mol Diagn* (2021) **23**:1478–90. doi:10.1016/j.jmoldx.2021.07.019
42. Akaçın İ, Ersoy Ş, Doluca O, Güngörmüşler M. Comparing the significance of the utilization of next generation and third generation sequencing technologies in microbial metagenomics. *Microbiol Res* (2022) **264**:127154. doi:10.1016/j.micres.2022.127154



OPEN ACCESS

*CORRESPONDENCE

F. D. Partey,
✉ fpartey@noguchi.ug.edu.gh

RECEIVED 19 November 2024

ACCEPTED 19 June 2025

PUBLISHED 21 July 2025

CITATION

Partey FD, Pobee ANA, Dampsey IK, Osei F, Owusu-Amponsah MMAK, Ansah YAA, Ye C, Bradfute S, Hurwitz I, Quashie PK, Ofori MF, Kusi AK, Perkins DJ and Awandare GA (2025) Functional antibody responses to SARS-CoV-2 variants before and after booster vaccination among adults in Ghana. *Exp. Biol. Med.* 250:10440. doi: 10.3389/ebm.2025.10440

COPYRIGHT

© 2025 Partey, Pobee, Dampsey, Osei, Owusu-Amponsah, Ansah, Ye, Bradfute, Hurwitz, Quashie, Ofori, Kusi, Perkins and Awandare. This is an open-access article distributed under the terms of the [Creative Commons Attribution License \(CC BY\)](https://creativecommons.org/licenses/by/4.0/). The use, distribution or reproduction in other forums is permitted, provided the original author(s) and the copyright owner(s) are credited and that the original publication in this journal is cited, in accordance with accepted academic practice. No use, distribution or reproduction is permitted which does not comply with these terms.

Functional antibody responses to SARS-CoV-2 variants before and after booster vaccination among adults in Ghana

F. D. Partey^{1*}, A. N. A. Pobee¹, I. K. Dampsey¹, F. Osei¹, M. M. A. K. Owusu-Amponsah¹, Y. A. A. Ansah¹, C. Ye², S. Bradfute², I. Hurwitz², P. K. Quashie³, M. F. Ofori¹, A. K. Kusi¹, D. J. Perkins² and G. A. Awandare³

¹Department of Immunology, Noguchi Memorial Institute for Medical Research, College of Health Sciences, University of Ghana, Accra, Ghana, ²Center for Global Health, Department of Internal Medicine, University of New Mexico School of Medicine, University of New Mexico, Albuquerque, NM, United States, ³West African Center for Cell Biology of Infectious Pathogens, College of Basic and Applied Sciences, University of Ghana, Accra, Ghana

Abstract

COVID-19 booster vaccinations are needed to enhance waning immunity and the emergence of new variants. In Africa, where COVID-19 vaccine coverage is low, there is a paucity of data on COVID-19 vaccine-induced immunity, particularly in the post-omicron era. This study examined the functional activity of vaccine-induced antibody responses against different variants before and after booster vaccinations in adults in Ghana, between November 2022 and February 2023. SARS-CoV-2 nucleocapsid protein and spike receptor binding domain (RBD) antigen-specific IgG levels against different viral variants were determined in plasma. Plasma was tested for the ability to inhibit ACE-2 binding to RBD variants. N antigen-specific antibody levels were comparable between vaccinated and previously infected, but unvaccinated individuals. However, RBD IgG levels before booster vaccinations were significantly higher in vaccinated participants than in exposed, unvaccinated individuals, except for Omicron. RBD IgG levels remained unchanged after the booster in participants with three prior vaccine doses but were significantly higher than in those with only primary vaccinations (Wild type $p = 0.0315$, Alpha $p = 0.0090$, Beta $p = 0.0020$, Delta $p = 0.0040$) except Omicron ($p = 0.09$). Participants who received the Pfizer-BioNTech vaccine showed a significant increase ($p < 0.05$) in RBD IgG levels against all tested variants from baseline to 3 months. In contrast, participants who received the J&J vaccine only showed a significant increase in RBD IgG to Wildtype ($p = 0.04$), Alpha ($p < 0.0001$), and Beta ($p < 0.0001$), but not Delta and Omicron. The inhibition of ACE-2 binding and live virus neutralization titers were significantly higher in vaccinated individuals than in unvaccinated individuals before the booster ($p < 0.001$). Virus neutralization titers against Wildtype were significantly high 3 months after booster ($p < 0.001$), but

neutralization titers against Omicron remained stable from baseline to 3 months after booster. Extended interval between vaccinations may enhance vaccine-induced antibody responses.

KEYWORDS

COVID-19 vaccination, COVID-19 booster, SARS-CoV-2, booster vaccination, COVID-19

Impact statement

Information on COVID-19 booster vaccine-induced immunity and the timing of booster vaccination for enhanced immunity against emerging viral variants in sub-Saharan Africa is scanty. This study provides knowledge on the efficacy of COVID-19 booster vaccines specifically within the African population by examining the functional activity of vaccine-induced antibody responses against different.

SARS-CoV-2 variants. This work offers new insights into COVID-19 vaccine effectiveness and durability in Ghanaian adults, showing that booster doses enhance antibody levels and cross-reactive responses, though they have limited impact on omicron-specific responses. It also finds that Pfizer-BioNTech's mRNA vaccine is more effective than the J&J vaccine in boosting antibody responses. Our data supports extended dosing intervals for enhanced vaccine-induced responses. This finding has implications for guiding vaccination policies and resource allocation in resource-limited settings.

Introduction

The global administration of COVID-19 vaccines significantly reduced mortality rates during the SARS-CoV-2 pandemic [1]. Vaccination further reduces the risk of severe disease [2–5], hospitalizations [6–8] and post-disease conditions [9, 10]. However, declining immune response following both natural infections and vaccinations, along with the emergence of viral variants with enhanced transmission, necessitates booster vaccinations to enhance and/or maintain immunity. In many advanced countries, additional booster vaccinations have been recommended. A meta-analysis examining the declining efficacy of COVID-19 vaccines by the number of doses against the SARS-CoV-2 Delta and Omicron variants found that protection is significantly enhanced and more durable after booster vaccinations compared to primary vaccination [11]. However, there remains a significant knowledge gap regarding the durability of vaccine-induced immune responses after booster vaccinations within the broader sub-Saharan African (SSA) population. Understanding the longevity of these immune responses within populations is crucial for informing vaccination strategies to mitigate future epidemics.

Several studies among Africans demonstrate that even among HIV uninfected individuals, there is chronic immune

dysregulation when compared to other populations [12–15]. This observation is characterised by low CD4⁺ T cells count and a skewed CD4/CD8 ratio. Immune dysregulation is largely triggered by environmental factors [12, 16]. A key environmental factor is infection with helminths which attenuate responses to parasitic [17], bacterial [18, 19] and viral infections [20]. Similarly, helminth-driven immune dysregulation has been found to negatively affect vaccine efficacy in African populations [21, 22]. Helminth-infected individuals elicit reduced vaccine-induced immune responses against malaria [23], tetanus toxoid [24], and *Bacillus Calmette-Guérin* (BCG) [25]. The mechanisms by which co-infections attenuate vaccine-induced immune responses include systemic immunosuppression [26], depletion of immune cells [21] and increased activation of immune tolerogenic signals [22].

Earlier studies on both mRNA and adenoviral-vectored COVID-19 vaccines revealed high vaccine immunogenicity among African adult populations [27–30], comparable to studies from developed countries and other low- and middle-income countries (LMICs) with similar demographics. These studies demonstrated heightened antibody responses in previously infected individuals compared to those in infection-naïve individuals. However, these studies primarily reported on binding antibody titers and did not assess the functionality of vaccine-induced antibodies, such as virus-neutralizing antibody titers. Neutralization assays estimate the ability of circulating virus-specific antibodies to prevent viral entry into the host cells. Serum neutralizing antibody titers have been shown to strongly correlate with protection in both clinical and animal studies [31–33]. ACE-2 inhibition assays are surrogate neutralization assays that quantify the capacity of antibodies to block the binding of the SARS-CoV-2 spike protein to ACE-2 [34]. Together, these assays provide insights into the quality of vaccine-induced humoral responses and potential vaccine efficacy beyond antibody magnitude. Furthermore, the dynamics of immune responses to heterologous vaccination regimens after additional booster shots in SSA populations remain poorly understood.

Ghana was the first African country to receive nCoV-Chadox 1 (Oxford/AstraZeneca) vaccines from the COVID-19 Vaccines Global Access (COVAX) facility, a platform created to ensure equitable access to vaccines. mRNA-based (Pfizer-BioNTech BNT162b2 and Moderna mRNA-1273) and adenoviral-vectored [Sputnik V and Johnson & Johnson (J&J)] vaccines were introduced to the public as they became available. While the

mRNA, AstraZeneca, and Sputnik V vaccines were administered in two doses, the J&J vaccine was primarily given as a single dose. Due to the logistical challenges in vaccine supply, the Ghana Health Service endorsed the use of different COVID-19 vaccines for the two-dose regimens, depending on the availability of vaccines in the country.

The population level COVID-19 vaccine efficacy within the African population outside clinical trials is unknown. Additionally, the impact of parasitic and other viral coinfections on vaccine-induced immune responses remains poorly defined.

In the present study, we examine the functional activity of COVID-19 vaccine-induced antibody responses against various SARS-CoV-2 variants after booster vaccinations among vaccinated and unvaccinated Ghanaian adults with prior SARS-CoV-2 infection.

Materials and methods

Study design and participant

The present study was conducted between November 2022 and February 2023. Previously vaccinated individuals ≥ 18 years who were willing to receive COVID-19 booster vaccines were enrolled in the study. Participants were recruited after informed consent, from vaccination centers around the University of Ghana, Legon, and its environs in the capital city, Accra. Blood samples were collected from participants before the last booster vaccination and 3 months after receiving the booster vaccination. Blood samples from unvaccinated individuals who were COVID-19-positive, either by PCR or rapid diagnostic test, were used as controls. Control samples were collected in April 2021 before the mass vaccination campaign was launched in Ghana. The samples were used as naturally exposed unvaccinated controls to examine vaccine-induced responses in naturally exposed individuals, as exposure was high in the study population. We randomly selected archived samples for which sufficient biological material was available for all assays. For all participants, blood was drawn into heparinized tubes and centrifuged at $800 \times g$ for 5 min to separate plasma from the cellular fraction. Plasma was stored at -30°C until ready for use.

SARS-CoV-2 antigens

The nucleocapsid (N) antigen used in the study was expressed in *Escherichia coli*, while the receptor binding domain (RBD) of the spike protein of the ancestral strain was expressed in freestyle 293F cell systems as described elsewhere [18, 35]. Alpha and Beta RBD were optimized for expression in the ExpreS2 platform as described [9, 36]. Delta RBD (Sino Biological # 40592-V08H115) and Omicron RBD (Sino Biological # 40592-V08H143) were expressed with a polyhistidine tag at the C-terminus in HEK293 cells.

Enzyme-linked immunosorbent assay for SARS-CoV-2 antigens

An indirect ELISA was used to measure plasma antigen-specific IgG to N and RBD of the various SARS-CoV-2 variants as previously described [37, 38]. Nunc Maxisorp plates were individually coated with either 0.5 $\mu\text{g/mL}$ of N antigen, Ancestral RBD, Alpha RBD, and Beta RBD or 1 $\mu\text{g/mL}$ of Delta RBD and Omicron RBD at 4°C overnight. Plates were then washed with 0.05% Tween in PBS and blocked with 1% BSA in PBS for an hour at room temperature (RT) before use. Subsequently, plasma was added to the wells in duplicate at a dilution of 1:100 for all antigens and incubated for 1 h at RT. Plates were washed and HRP-conjugated rabbit anti-human secondary antibody (1:3000) was added and incubated at RT for 1 h. Wells were developed by adding 3,3',5,5'-tetramethylbenzidine (TMB) as substrate and stopped with 2 N H_2SO_4 . Absorbance in each well was read at 450 nm using a microplate reader.

To establish a cutoff for seropositivity against any antigen, pre-pandemic samples were included in the assay as negative controls, and the COVID-19 convalescent plasma pool was used as a positive control. Positive and negative controls were included on each plate to account for plate-to-plate and inter-assay variations.

SARS-CoV-2 inhibitor screening

Plasma from a subset of participants (vaccinated $n = 21$, unvaccinated $n = 55$) was screened for its ability to inhibit ACE-2 binding to RBD variants using the SARS-CoV-2 Variant Inhibitor Screening Kit (R&D Systems, #VANC00B) following the manufacturer's protocol. Briefly, 96 well plates were coated with His-Tag capture antibody and incubated at 4°C overnight. The plates were washed and blocked for 1 h at 37°C . RBD variants (wild type, alpha, delta, and omicron) were added to different wells in plates and incubated for 1 h at RT. After incubation, the plates were washed, plasma was added to the wells at a dilution of 1:100 and then incubated for 1 h at RT. Biotinylated human ACE-2 was added to wells followed by 90 min incubations. Following washing, streptavidin-HRP conjugate was added to plates and incubated for 30 min at RT. The plates were washed, substrate solution added, followed by incubation at RT for 20 min. The reaction was stopped with 2 N H_2SO_4 and the absorbance was read at 450 nm.

Plaque reduction neutralization test

The same plasma from vaccinated individuals ($n = 55$) tested in the ACE inhibition above was also tested in a live virus neutralization assay against the wild-type and Omicron viral variants (BEI Resources; National Institute of Allergy and Infectious Diseases) as described previously [39]. In summary, the isolates were diluted to 50–100 plaque forming units/200 μL in

TABLE 1 Characteristics of vaccinated and unvaccinated participants.

Variables	Vaccinated	Unvaccinated	P - value
n	86	36	
Age, yr, <i>n</i> (%)			
18–25	48 (55.82)	12 (33.33)	p = 0.004
26–35	22 (25.58)	7 (19.44)	
36–45	8 (9.3)	9 (25)	
46–60	8 (9.3)	8 (22.22)	
Sex, <i>n</i> (%)			
Female	31 (36.05)	22 (64.71)	p = 0.003
Male	55 (63.95)	12 (35.29)	
Previous vaccination, <i>n</i> (%)			
AstraZeneca	40 (46.51)	n. a	
J&J	19 (22.10)		
Moderna	15 (17.44)		
Pfizer	9 (10.47)		
Others	3 (3.49)		
Number of previous vaccine doses <i>n</i> (%)			
1	19 (20.10)	n. a	
2	52 (60.47)		
3	15 (17.44)		
Time since first vaccine dose, days mean (range)	461 (45–734)	n. a	
Time since first vaccine dose, days mean (range)	372 (45–666)		

Abbreviation: n.a, not applicable.

minimum essential medium supplemented with 2.5% heat inactivated fetal calf serum (viral growth medium). Test plasma was heat inactivated at 56°C for 30 min and 2-fold serial dilutions prepared starting from a dilution of 1:40. The diluted plasma was added to equal volumes of diluted virus and incubated for 1 h. The plasma-virus culture was next added to Vero E6 cells and incubated at 37°C for 2 h. Virus-only mixtures were used as controls. Following virus aspiration, cells were overlaid with virus overlay medium by mixing equal volumes of 2x antibiotic-containing virus growth medium and 2% agarose gel and incubated at 37°C for 48 h. Cells were fixed with 4% formaldehyde overnight at 4°C. subsequently, the overlay was removed, and cells were stained with 0.5% crystal violet for 2 min, washed, and dried. Plaques were enumerated to estimate 80% plaque reduction neutralization titers (PRNT80). We determined PRNT80 as a more stringent reduction threshold to detect robust protective neutralization titers and reduce the risk of background cross-reactive antibodies

Statistical analysis

Statistical analyses were performed using GraphPad Prism software version 10.0. The Kruskal–Wallis test was used to compare IgG levels between the groups. Two-way ANOVA was used to compare IgG levels before and after vaccination between and within different participant groups. All comparisons were two-tailed and P values < 0.05 were regarded as statistically significant.

Results

Patient characteristics

This study recruited 86 vaccinated individuals between November 2022 and February 2023. The vaccinated participants comprised 31 females and 55 males with an age range of 18–60 years (Table 1). Most volunteers were aged 18–25

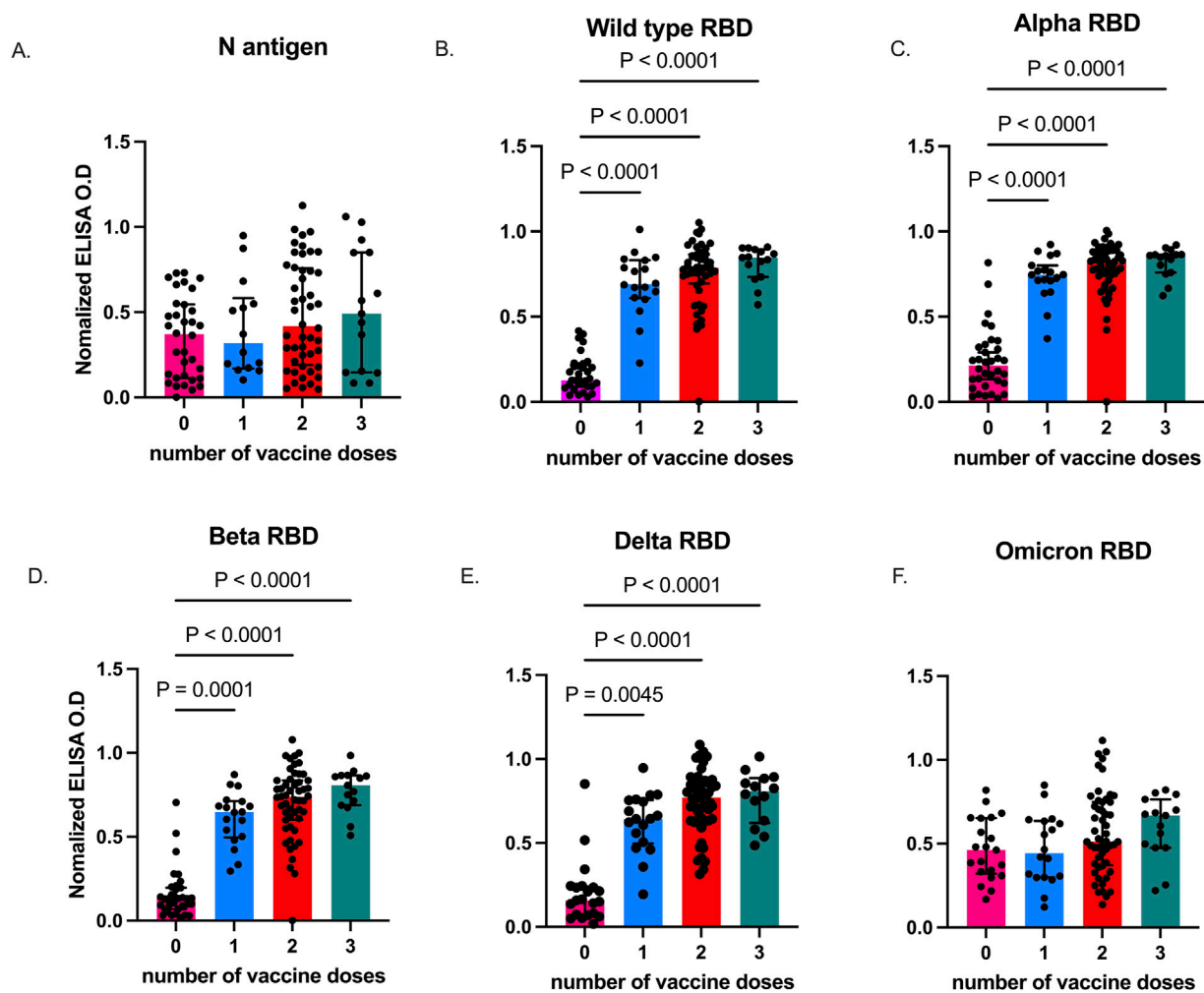


FIGURE 1
SARS-CoV-2-specific IgG levels in vaccinated and unvaccinated adults. Data plots showing plasma N antigen levels (A), and plasma RBD IgG levels against Wild type (B), Alpha (C), Beta (D), Delta (E), and Omicron (F). Bars indicate the median and error bars represent the interquartile range. P values < 0.05 are stated on the graphs. Unvaccinated controls were designated as those who received zero vaccine doses.

(55.82%). At enrolment, the vaccinated participants had previously received at least one shot of one vaccine type, including AstraZeneca (46.51%), J&J (22.1%), Moderna (17.44%), or Pfizer-BioNTech (10.5%). The mean number of days from the primary vaccination to baseline sampling was 461, ranging from 45 to 734 days. The mean number of days from the last vaccination to baseline sampling was 372, ranging from 45 to 666 days, and was significantly higher among participants who had received two vaccine doses than among those who had received only one dose in the study (Supplementary Figure S1). The unvaccinated controls were previously infected individuals with a confirmed RT-PCR or antigen-RDT diagnosis, who were enrolled in a related study in March 2021.

SARS-CoV-2 RBD-specific antibodies are boosted with vaccination in naturally exposed individuals

Previous seroepidemiological studies in Accra and its surrounding areas found high SARS-CoV-2 exposure among the general population [40]. Thus, we first measured antibodies against the nucleoprotein (N) in plasma from all study participants at baseline, before they received booster vaccination and plasma from individuals with confirmed SARS-CoV-2 collected in 2021 were also included as unvaccinated controls. Plasma N antigen-specific IgG levels were comparable between vaccinated individuals who had received at least a single dose of COVID-19 vaccine and exposed unvaccinated individuals ($p = 0.2095$ (Figure 1A). In

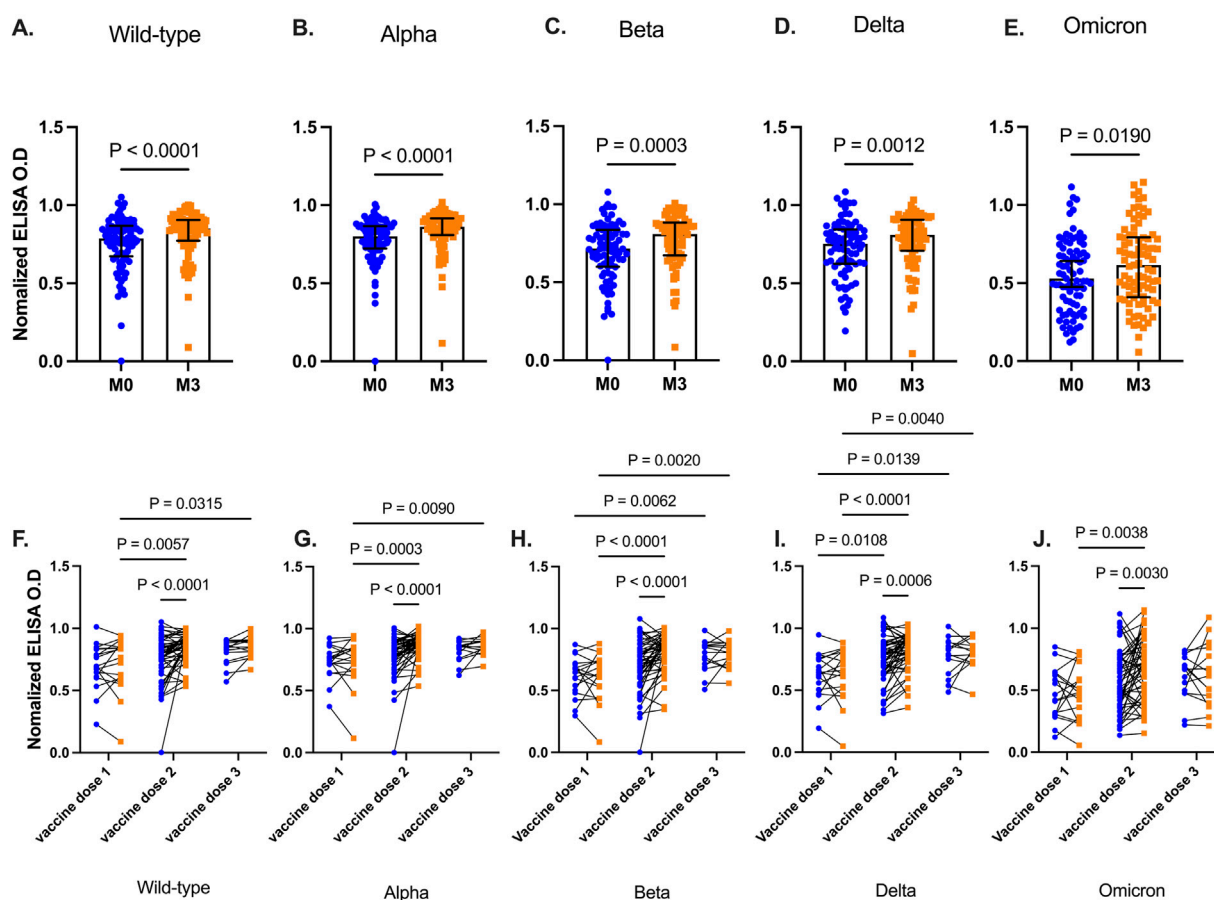


FIGURE 2

SARS-CoV-2 RBD levels before and 3 months after booster vaccinations. Data plots showing plasma RBD IgG levels against Wild type (A), Alpha (B), Beta (C), Delta (D), and Omicron (E). Bars indicate the median and error bars represent the interquartile range. Line plots showing RBD IgG levels before and 3 months post-booster vaccination against Wild type strain (F), Alpha (G), Beta (H), Delta (I), and Omicron (J) variants. Participants are grouped based on the number of COVID-19 vaccines they had received before receiving the additional booster vaccination. Blue-filled circles and orange-filled squares represent IgG levels at baseline and month 3 respectively. Comparisons were done before and after across the number and vaccines received. P values <0.05 are stated on the graphs.

contrast, RBD antibodies against the different viral strains (Figures 1B–E) were significantly higher ($p < 0.0001$) in the vaccinated participants at enrolment when compared to exposed, unvaccinated individuals, except for Omicron ($p = 0.1161$, Figure 1F).

We determined levels of vaccine-induced antibody responses, 3 months post-booster administration. Plasma collected before, and after, booster vaccinations were tested for antibodies against RBD antigens from the five SARS-CoV-2 variants. Plasma RBD-IgG levels increased significantly 3 months after the booster vaccination for Wild type ($p < 0.0001$), Alpha ($p < 0.0001$), Beta ($p = 0.0003$), Delta ($p = 0.0012$), and Omicron ($p = 0.0190$) (Figures 2A–E).

More granularity was achieved when participants were then grouped based on the number of COVID-19 vaccine doses they had received prior to the additional booster (Figures 2F–J). There

was no significant difference between RBD IgG levels at baseline and 3 months after the booster, for all tested viral strain antigens (Wild type $p = 0.64$, Alpha $p = 0.95$, Beta $p = 0.99$, Delta $p = 0.91$, Omicron $p = 0.89$) in participants who received only a single dose of the COVID-19 vaccine. In contrast, individuals who had received two vaccine doses and the booster showed a marked increase (Wild type, Alpha, Beta, $p < 0.001$, Delta $p = 0.0006$, Omicron $p = 0.003$) in RBD IgG levels against all viral strain antigens. Similar results were observed 3 months post booster in participants with three prior vaccine doses except for Omicron ($p = 0.80$), RBD IgG levels increased modestly after the booster. However, for the other viral variants, RBD IgG levels were significantly higher than in those with only primary vaccinations (Wild type $p = 0.032$, Alpha $p = 0.009$, Beta $p = 0.002$, Delta $p = 0.004$).

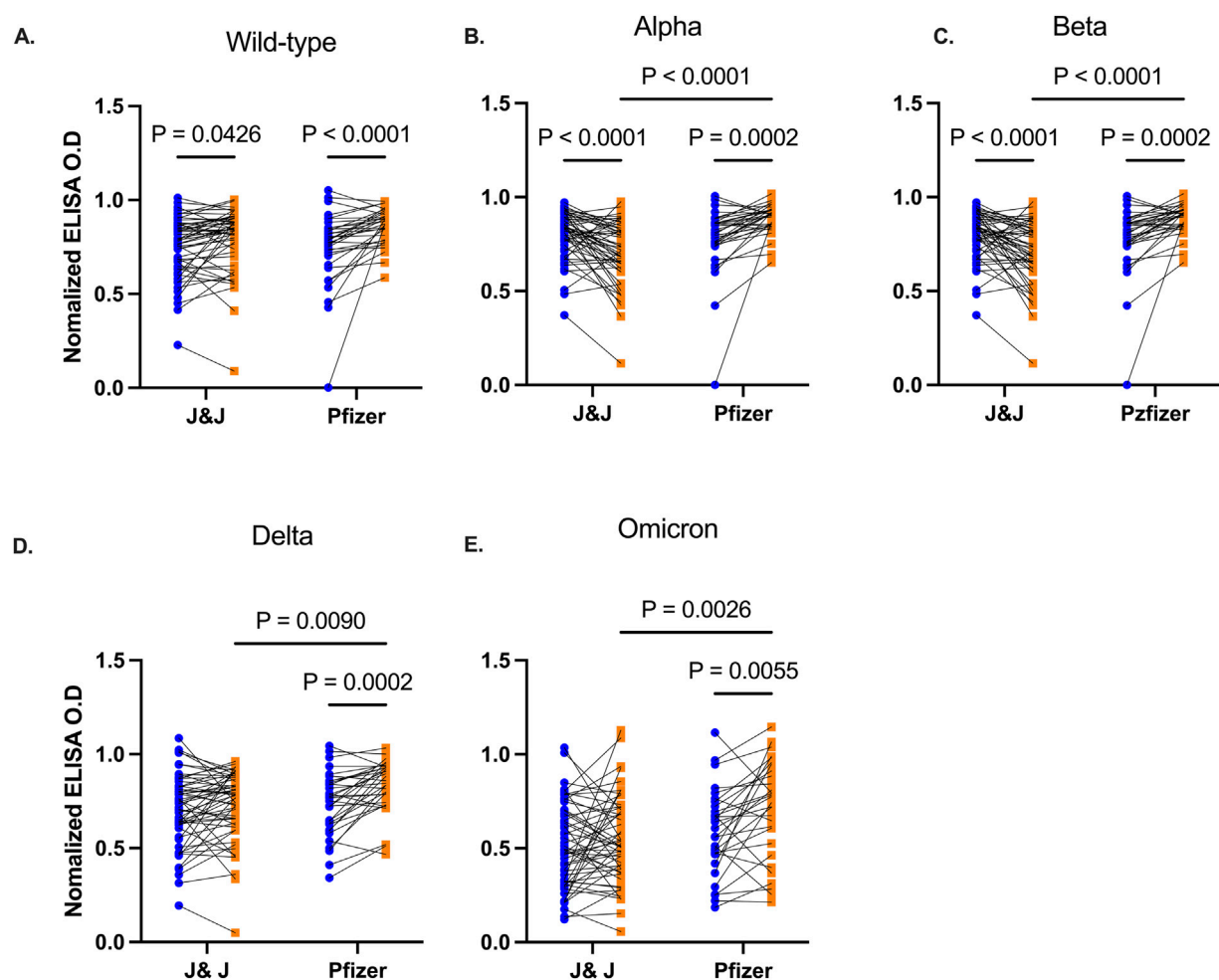


FIGURE 3

Comparative RBD IgG levels between participants receiving Pfizer-BioNTech and J&J vaccine. Line plots showing RBD IgG levels before and 3 months post booster vaccination against Wild type (A), Alpha (B), Beta (C), Delta (D), and Omicron (E) variants. Participants are grouped based on the type of booster vaccine they received. Blue-filled circles and orange-filled squares represent IgG levels at baseline and month 3 respectively. P values < 0.05 are stated on the graphs.

BNT162b2 Pfizer/Bio-n-tech booster vaccination enhances durability of cross-strain reactive antibodies 3 months post booster vaccination

We then examined the durability of vaccine-induced antibodies based on the type of booster, Pfizer-BioNTech or J&J, the participants received. Anti-RBD IgG antibody levels were comparable between individuals prior to receiving the booster. Three months following booster, participants ($n = 34$) who received the Pfizer-BioNTech booster elicited a marked increase in their antibody levels against RBD of all the test viral variants (Wild type $p < 0.0001$, Alpha $p = 0.0002$, Beta $p = 0.0002$, Delta $p = 0.0002$, Omicron $p = 0.0055$, Figures 3A–E). Recipients ($n = 55$) of the J&J booster also showed an increase in

anti-RBD antibody levels against the Wild type ($p = 0.043$), Alpha ($p < 0.0001$) and Beta variants ($p < 0.0001$) but IgG levels against Delta ($p = 0.12$) and Omicron ($p = 0.22$) variants remained unchanged relative to pre-booster levels.

Booster vaccination enhances cross-strain viral-neutralizing antibodies

The functionality of antibodies that would block the binding of SARS-CoV-2 RBD to the angiotensin-converting enzyme (ACE-2) receptor on host cells was assessed by screening plasma from two distinct groups of participants – those who were unvaccinated but had been exposed to SARS-CoV-2, and those who had been vaccinated. Plasma collected from these

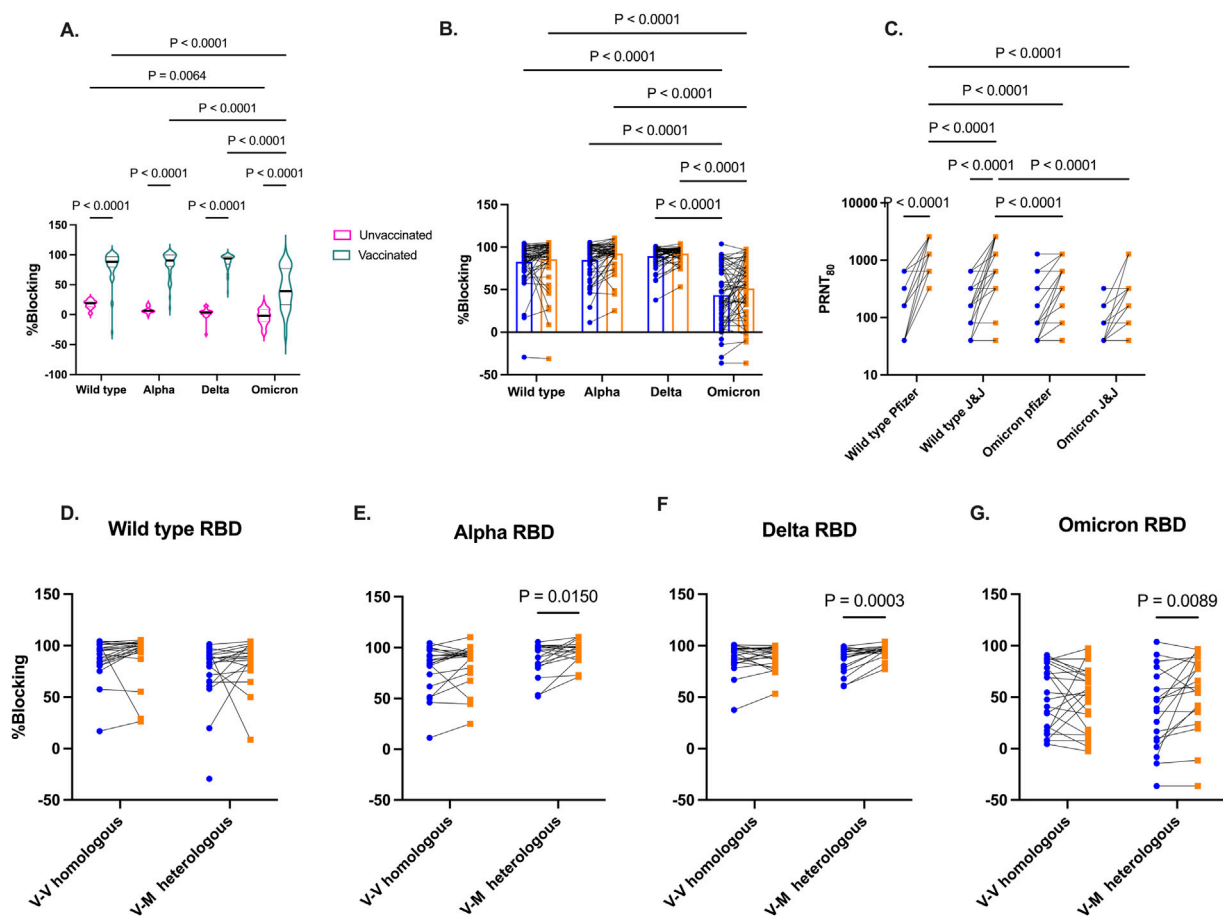


FIGURE 4

Competitive inhibition of ACE-2 binding to RBD and live virus neutralization. *In vitro* inhibition of ACE-2 binding to RBD by plasma from vaccinated and unvaccinated volunteers (A). Percentage blocking among vaccinated individuals before and 3 months after booster vaccinations (B). Live virus neutralization by plasma from vaccinated individuals against wild-type and Omicron variants based booster type received (Pfizer or J&J) (C). Percentage blocking of ACE-2 binding among vaccinated individuals grouped by homologous and heterologous booster vaccination regimen against RBD from Wild type (D), Alpha (E), Delta (F), and Omicron (G). Blue-filled circles and orange-filled squares represent IgG levels at baseline and month 3 respectively. P values <0.05 are stated on the graphs.

participants was screened for inhibition of ACE-2 binding to RBD from Wild type, Alpha, Delta, and Omicron utilizing a commercially available kit. As expected, vaccinated individuals before booster show higher inhibition of ACE-2 binding to Spike RBD across the four SARS-CoV-2 strains compared to those who were exposed but unvaccinated (Figure 4A). In vaccinated group, binding inhibition was found to be lowest against Omicron Spike RBD.

The level of SARS-CoV-2 Spike RBD binding antibodies was examined again 3-month later following booster administration (Figure 4B). While there was an increase in Spike RBD binding antibodies levels across all four viral variants post-booster, the levels of inhibitory antibodies were not found to be significant (Wild type $p = 0.47$, Alpha $p = 0.08$, Delta $p = 0.48$, Omicron ($p = 0.08$). Furthermore, pre- and post-booster plasma were tested in a plaque reduction neutralization test (PRNT) to demonstrate

in vitro neutralization against wildtype and Omicron strains (Figure 4C). Boosted plasma showed a significant enhancement ($p < 0.0001$) in neutralizing wildtype SARS-CoV-2 among recipients of both the Pfizer and Janssen booster shots. However, 3 months post-booster, the neutralizing IgG levels were notably higher in Pfizer recipients compared to those who received the Janssen booster ($p < 0.0001$). In contrast, Omicron neutralizing IgG levels did not significantly increase in both recipient groups from baseline to 3 months post booster. Wildtype neutralizing IgG levels were markedly high than Omicron neutralizing IgG levels 3 months post booster ($p < 0.0001$).

Since most of our participants received viral-vectored vaccines as primary vaccinations, we grouped participants into homologous and heterologous groups. Homologous vaccination received viral-vectored vaccines as both primary and booster

vaccination. Heterologous vaccination received viral-vectored and were subsequently boosted with the mRNA-based Pfizer vaccine. ACE-2 inhibitory antibody levels against the Spike RBD of the viral variants was examined 3 months post booster (Figures 4D–G). No difference was seen in the level of inhibitory IgG levels against the 4 SARS-CoV-2 variants for the homologous group. However, heterologous boosting increased inhibitory antibody levels Against Alpha ($p = 0.02$), Delta ($p = 0.0003$), and Omicron ($p = 0.0089$).

Discussion

The emergence of SARS-CoV-2 variants and waning immunity after infection or vaccination necessitated vaccine boosting to maintain durable immune responses [41]. In sub-Saharan Africa (SSA), there is a paucity of data on the real-world efficacy and durability of COVID-19 vaccine responses, particularly in the post-Omicron era. In the present study, we examined the magnitude and functionality of SARS-CoV-2-specific antibody responses among vaccinated Ghanaian adults 3 months after receiving either Pfizer-BioNTech or J&J booster immunizations and compared these against responses in unvaccinated individuals with natural SARS-CoV-2 infections.

Before the booster, anti-N antibodies were comparable between vaccinated and unvaccinated individuals with a known history of infection. Consistent with findings from different geographical settings [42, 43], vaccination did not impact anti-N antibodies among our participants. This suggests that anti-N antibodies were acquired from natural infections rather than from vaccination. We note a high proportion of vaccinated individuals were seropositive for N antibodies, reinforcing earlier findings that undetected asymptomatic SARS-CoV-2 infection rates in Ghana [37, 40] and other countries in SSA [44] were high.

At baseline, vaccinated individuals had significantly high levels of anti-RBD IgG levels against Ancestral, Alpha, and Delta ($p < 0.05$) but not Omicron ($p = 0.12$), when compared to unvaccinated controls, suggesting the presence of vaccination-induced cross-reactive antibodies. Baseline anti-RBD IgG levels against Omicron did not differ either by the number of prior vaccine doses received or between previously vaccinated and unvaccinated individuals sampled in 2021. Omicron was first reported in Botswana and South Africa in late 2021 [45], and was already in circulation in Ghana at the time of enrolment [46]. The Omicron variant is highly mutated compared to the Delta and other earlier variants. Mutations occur in both structural and non-structural proteins [47] which increases its transmissibility and enhances immune evasion from previous immunity [48–50]. Due to the mutations in the Omicron RBD, it is not surprising we observed reduced omicron-specific IgG binding levels in the vaccinated and unvaccinated groups. Our findings are similar

to previous studies in different populations showing reducing binding and neutralizing antibody against Omicron [51, 52].

Overall, increased anti-RBD IgG levels against all SARS-CoV-2 strains in individuals who had previously received two or three vaccine doses, compared to those who had received only a single dose. Despite the vaccinated individuals' seeming exposure to SARS-CoV-2, one booster dose did not significantly boost RBD IgG levels beyond baseline levels. Since participants were sampled 3 months after receiving their booster, it is possible that antibody levels had peaked earlier and declined more rapidly in participants who received one vaccine dose compared to those who had received at least two vaccine doses. A previous study in Ugandan adults who received the AstraZeneca vaccine [30] reported increase in RBD-specific IgG and IgA levels 14 days after the second vaccine dose, peaking at day 28, followed by a gradual decline in IgG levels.

The administration of a fourth booster dose to participants who were vaccinated three times did not significantly increase RBD IgG levels against all the tested viral strains. This raises a question regarding the timing of booster vaccination. The median time since the last vaccination before administering the booster in the present study was significantly higher among individuals who had received two vaccine doses relative to those who had just received a single dose (Supplementary Figure S1). It is well established that an extended dosing duration between vaccinations could enhance vaccine immunogenicity [53–55]. Another explanation for this observation is that within the settings of the study where natural exposure is high, few vaccine boosters may be required to reach the threshold of antigen stimulated immunity. Under such circumstances, natural infections may offer additional booster effects. Similar observations have been made in other populations within sub-Saharan Africa [27]. In resource-limited settings like SSA with high SARS-CoV-2 exposure, our data suggests that fewer booster vaccinations at longer intervals may help maintain robust antibody responses. However, it is critical to consider the specific needs of target populations, such as the elderly and individuals with comorbidities, who are at the highest risk of severe disease.

Functional antibody responses were assessed using either their capacity to inhibit the binding of a soluble form of the ACE-2 to the RBD from the Wild type, Alpha, Beta, Delta, and Omicron viral variants, or their capacity to neutralize viruses expressing the spike proteins from the Wild type and Omicron SARS-CoV-2 variants. Inhibition to ACE-2 binding to RBD from all tested variants markedly increased among the vaccinated individuals relative to the unvaccinated individuals. However, inhibition of ACE-2 binding to the Omicron RBD was significantly lower compared to the other variants tested. Similarly, cross-strain viral neutralizing activity among the vaccinated individuals was enhanced with booster vaccinations. Our findings are in line with prior studies showing reduced neutralization against Omicron than earlier variants [55].

Participants who received heterogeneous vaccine doses (J&J followed by Pfizer-BioNTech booster) displayed significantly higher ($p < 0.05$) antibody responses quantitatively and

qualitatively compared to those who received homologous vaccine doses (J&J followed by J&J booster). The findings of the present study are consistent with earlier research which demonstrated that [56] mRNA vaccines, when used in heterologous booster regimens, elicit stronger IgG binding and neutralizing activities against Wild-type, Delta and Omicron variants compared to viral-vectored vaccines.

There are several limitations to our study. The limited age range of our study participants prevented us from examining the age effects on vaccine-induced antibody responses. A second limitation is 3-month interval between the booster vaccination and the blood draw. This prevented us from tracking antibody levels during the intervening period. Nonetheless, we still noted the significant increase in IgG levels in recipients of the Pfizer-BioNTech booster in comparison to those receiving the J&J booster. Future experiments would involve longitudinal studies to track IgG antibody levels and neutralization activities at multiple time points post-booster, and to compare these activities in mRNA and viral-vectored vaccines. A third limitation is the variation in the enrolment timelines between our vaccinated participants and unvaccinated controls. When the vaccinated participants were recruited in 2022, Ghana had already experienced four waves of COVID-19 driven by the emergence of new SARS-CoV-2 variants. The consistent levels of anti-N IgG levels in vaccinated individuals before and after booster vaccination would suggest that these participants were not exposed to SARS-CoV-2 in the intervening period. However, we cannot rule out the possibility that vaccinated individuals may have been infected since 2021, when the unvaccinated cohort was recruited. In addition, we noted a significant difference in sex between vaccinated and unvaccinated cohorts. However, we do not observe sex-dependent difference in variant-specific RBD IgG levels from baseline to 3 months post booster (Supplementary Figure S2).

In conclusion, we have shown that booster vaccination increases cross-strain viral IgG binding and neutralizing activity compared to natural infections in Ghanaian adults. Extended interval between vaccinations enhances vaccine-induced antibody responses, and booster vaccinations with the mRNA Pfizer-BioNTech vaccine were more effective than the vectored J&J vaccine.

Author contributions

FP: Funding acquisition, conceptualization, investigation, data curation, formal analysis, methodology, writing of original draft. AP, ID, FO, MO-A, YA, CY, PQ, SB, and IH: data curation, investigation, methodology, and editing of manuscript. MO, AK, DP, and GA: funding acquisition, conceptualization, review and editing of manuscript. All authors contributed to the article and approved the submitted version.

Data availability

The original contributions presented in the study are included in the article/Supplementary Material, further inquiries can be directed to the corresponding author.

Ethics statement

The studies involving humans were approved by The Institutional Review Board of the Noguchi Memorial Institute for Medical Research (NMIMR-IRB CPN 017/22-23). The studies were conducted in accordance with the local legislation and institutional requirements. The participants provided their written informed consent to participate in this study.

Funding

The author(s) declare that financial support was received for the research and/or publication of this article. The study was funded by the National Institutes of Health (NIH) Fogarty International Center Grant (D43TW010543) and the Ghana COVID-19 Trust Fund.

Acknowledgments

We are thankful to the individuals who volunteered to participate in this study and the health workers who supported us. The Authors thank Prof. Ali Salanti for generously providing the Wild type, Alpha and Beta RBD antigens.

Conflict of interest

The author(s) declared no potential conflicts of interest with respect to the research, authorship, and/or publication of this article.

Generative AI statement

The author(s) declare that no Generative AI was used in the creation of this manuscript.

Supplementary material

The Supplementary Material for this article can be found online at: <https://www.ebm-journal.org/articles/10.3389/ebm.2025.10440/full#supplementary-material>

References

- Watson OJ, Barnsley G, Toor J, Hogan AB, Winskill P, Ghani AC. Global impact of the first year of COVID-19 vaccination: a mathematical modelling study. *The Lancet Infect Dis* (2022) 22:1293–302. doi:10.1016/s1473-3099(22)00320-6
- Lin D-Y, Gu Y, Wheeler B, Young H, Holloway S, Sunny S-K, et al. Effectiveness of covid-19 vaccines over a 9-month period in North Carolina. *New Engl J Med* (2022) 386:933–41. doi:10.1056/nejmoa2117128
- Dagan N, Barda N, Kepten E, Miron O, Perchik S, Katz MA, et al. BNT162b2 mRNA covid-19 vaccine in a nationwide mass vaccination setting. *New Engl J Med* (2021) 384:1412–23. doi:10.1056/nejmoa2101765
- Wada N, Li Y, Hino T, Gagne S, Valtchinov VI, Gay E, et al. COVID-19 Vaccination reduced pneumonia severity. *Eur J Radiol Open* (2022) 9:100456. doi:10.1016/j.ejro.2022.100456
- Chung H, He S, Nasreen S, Sundaram ME, Buchan SA, Wilson SE, et al. Effectiveness of BNT162b2 and mRNA-1273 covid-19 vaccines against symptomatic SARS-CoV-2 infection and severe covid-19 outcomes in Ontario, Canada: test negative design study. *BMJ* (2021) 374:n1943. doi:10.1136/bmj.n1943
- Bahl A, Johnson S, Maine G, Garcia MH, Nimmagadda S, Qu L, et al. Vaccination reduces need for emergency care in breakthrough COVID-19 infections: a multicenter cohort study. *The Lancet Reg Health – Americas* (2021) 4:100065. doi:10.1016/j.lana.2021.100065
- Tenforde MW, Self WH, Adams K, Gaglani M, Ginde AA, McNeal T, et al. Association between mRNA vaccination and COVID-19 hospitalization and disease severity. *JAMA* (2021) 326:2043–54. doi:10.1001/jama.2021.19499
- Shoukat A, Vilches TN, Moghadas SM, Sah P, Schneider EC, Shaff J, et al. Lives saved and hospitalizations averted by COVID-19 vaccination in New York City: a modeling study. *The Lancet Reg Health – Americas* (2022) 5:100085. doi:10.1016/j.lana.2021.100085
- Lundberg-Morris L, Leach S, Xu Y, Martikainen J, Santosa A, Gisslén M, et al. Covid-19 vaccine effectiveness against post-covid-19 condition among 589 722 individuals in Sweden: population based cohort study. *BMJ* (2023) 383: e076990. doi:10.1136/bmj-2023-076990
- Lam ICH, Zhang R, Man KKC, Wong CKH, Chui CSL, Lai FTT, et al. Persistence in risk and effect of COVID-19 vaccination on long-term health consequences after SARS-CoV-2 infection. *Nat Commun* (2024) 15:1716. doi:10.1038/s41467-024-45953-1
- Menegale F, Manica M, Zardini A, Guzzetta G, Marziano V, d'Andrea V, et al. Evaluation of waning of SARS-CoV-2 vaccine-induced immunity: a systematic review and meta-analysis. *JAMA Netw Open* (2023) 6:e2310650. doi:10.1001/jamanetworkopen.2023.10650
- Wolday D, Ndungu FM, Gómez-Pérez GP, de Wit TFR. Chronic immune activation and CD4+ T cell lymphopenia in healthy african individuals: perspectives for SARS-CoV-2 vaccine efficacy. *Front Immunol* (2021) 12:693269. doi:10.3389/fimmu.2021.693269
- Kassu A, Tsegaye A, Petros B, Wolday D, Hailu E, Tilahun T, et al. Distribution of lymphocyte subsets in healthy human immunodeficiency virus-negative adult Ethiopians from two geographic locales. *Clin Diagn Lab Immunol* (2001) 8:1171–6. doi:10.1128/cdli.8.6.1171-1176.2001
- Clerici M, Butto S, Lukwiya M, Saresella M, Declich S, Trabatttoni D, et al. Immune activation in Africa is environmentally-driven and is associated with upregulation of CCR5. *AIDS* (2000) 14:2083–92. doi:10.1097/00002030-200009290-00003
- Tsegaye A, Wolday D, Otto S, Petros B, Assefa T, Alebachew T, et al. Immunophenotyping of blood lymphocytes at birth, during childhood, and during adulthood in HIV-1-uninfected Ethiopians. *Clin Immunol* (2003) 109:338–46. doi:10.1016/j.clim.2003.08.008
- Temba GS, Vadaq N, Kullaya V, Pecht T, Lionetti P, Cavalieri D, et al. Differences in the inflammatory proteome of East African and Western European adults and associations with environmental and dietary factors. *eLife* (2023) 12: e82297. doi:10.7554/eLife.82297
- Hartgers FC, Obeng BB, Kruijze Y, Dijkhuis A, McCall M, Sauerwein RW, et al. Responses to malarial antigens are altered in helminth-infected children. *The J Infect Dis* (2009) 199:1528–35. doi:10.1086/598687
- Tristão-Sá R, Ribeiro-Rodrigues R, Johnson LT, Pereira FEL, Dietze R. Intestinal nematodes and pulmonary tuberculosis. *Rev Soc Bras Med Trop* (2002) 35:533–5. doi:10.1590/s0037-86822002000500020
- Resende Co T, Hirsch CS, Toossi Z, Dietze R, Ribeiro-Rodrigues R. Intestinal helminth co-infection has a negative impact on both anti-Mycobacterium tuberculosis immunity and clinical response to tuberculosis therapy. *Clin Exp Immunol* (2007) 147:45–52. doi:10.1111/j.1365-2249.2006.03247.x
- Furch BD, Koethe JR, Kayamba V, Heimburger DC, Kelly P. Interactions of schistosoma and HIV in sub-saharan Africa: a systematic review. *The Am J Trop Med Hyg* (2020) 102:711–8. doi:10.4269/ajtmh.19-0494
- Wait LF, Dobson AP, Graham AL. Do parasite infections interfere with immunisation? A review and meta-analysis. *Vaccine* (2020) 38:5582–90. doi:10.1016/j.vaccine.2020.06.064
- Malhotra I, McKibben M, Mungai P, McKibben E, Wang X, Sutherland LJ, et al. Effect of antenatal parasitic infections on anti-vaccine IgG levels in children: a prospective birth cohort study in Kenya. *PLOS Negl Trop Dis* (2015) 9:e0003466. doi:10.1371/journal.pntd.0003466
- Nouatin O, Mengue JB, Dejon-Agobé JC, Fendel R, Ibáñez J, Ngoa UA, et al. Exploratory analysis of the effect of helminth infection on the immunogenicity and efficacy of the asexual blood-stage malaria vaccine candidate GMZ2. *Plos Negl Trop Dis* (2021) 15:e0009361. doi:10.1371/journal.pntd.0009361
- Riner DK, Ndombi EM, Carter JM, Omondi A, Kittur N, Kavere E, et al. Schistosoma mansoni infection can jeopardize the duration of protective levels of antibody responses to immunizations against hepatitis B and tetanus toxoid. *Plos Negl Trop Dis* (2016) 10:e0005180. doi:10.1371/journal.pntd.0005180
- Malhotra I, McKibben M, Mungai P, McKibben E, Wang X, Sutherland LJ, et al. Effect of antenatal parasitic infections on anti-vaccine IgG levels in children A prospective Birth.pdf (2025). Available online at: <https://journals.plos.org/plosntds/article/file?id=10.1371/journal.pntd.0003466&type=printable> (Accessed May 19, 2025).
- Akoolo L, Rocha SC, Parveen N. Protozoan co-infections and parasite influence on the efficacy of vaccines against bacterial and viral pathogens. *Front Microbiol* (2022) 13:1020029. doi:10.3389/fmicb.2022.1020029
- Serwanga J, Ankunda V, Katende JS, Baine C, Oluka GK, Odoch G, et al. Sustained S-IgG and S-IgA antibodies to Moderna's mRNA-1273 vaccine in a Sub-Saharan African cohort suggests need for booster timing reconsiderations. *Front Immunol* (2024) 15:1348905. doi:10.3389/fimmu.2024.1348905
- Ankunda V, Katende JS, Oluka GK, Sembera J, Baine C, Odoch G, et al. The subdued post-boost spike-directed secondary IgG antibody response in Ugandan recipients of the Pfizer-BioNTech BNT162b2 vaccine has implications for local vaccination policies. *Front Immunol* (2024) 15:1325387. doi:10.3389/fimmu.2024.1325387
- Makhema J, Shava E, Izu A, Gaolathe T, Kuate L, Walker A, et al. Safety of AZD1222 COVID-19 vaccine and low incidence of SARS-CoV-2 infection in Botswana following ChAdOx1(AZD1222) vaccination: a single-arm open-label interventional study – final study results. *IJID Regions* (2024) 10:35–43. doi:10.1016/j.ijregi.2023.11.002
- Serwanga J, Baine C, Mugaba S, Ankunda V, Auma BO, Oluka GK, et al. Seroprevalence and durability of antibody responses to AstraZeneca vaccination in Ugandans with prior mild or asymptomatic COVID-19: implications for vaccine policy. *Front Immunol* (2023) 14:1183983. doi:10.3389/fimmu.2023.1183983
- Marchant A, Van Damme P, Plotkin S, Neels P, Cassetti MC, Cramer J, et al. Enabling the evaluation of COVID-19 vaccines with correlates of protection. *Biologicals* (2024) 85:101723. doi:10.1016/j.biologicals.2023.101723
- McMahan K, Yu J, Mercado NB, Loos C, Tostanoski LH, Chandrashekar A, et al. Correlates of protection against SARS-CoV-2 in rhesus macaques. *Nature* (2021) 590:630–4. doi:10.1038/s41586-020-03041-6
- Sadarangani M, Marchant A, Kollmann TR. Immunological mechanisms of vaccine-induced protection against COVID-19 in humans. *Nat Rev Immunol* (2021) 21:475–84. doi:10.1038/s41577-021-00578-z
- Tan CW, Chia WN, Qin X, Liu P, Chen MI-C, Tiu C, et al. A SARS-CoV-2 surrogate virus neutralization test based on antibody-mediated blockage of ACE2-spike protein-protein interaction. *Nat Biotechnol* (2020) 38:1073–8. doi:10.1038/s41587-020-0631-z
- Wrapp D, Wang N, Corbett KS, Goldsmith JA, Hsieh C-L, Abiona O, et al. Cryo-EM structure of the 2019-nCoV spike in the prefusion conformation. *Science* (2020) 367:1260–3. doi:10.1126/science.abb2507
- Fougeroux C, Goksøyr L, Idorn M, Soroka V, Myeni SK, Dagil R, et al. Capsid-like particles decorated with the SARS-CoV-2 receptor-binding domain elicit strong virus neutralization activity. *Nat Commun* (2021) 12:324. doi:10.1038/s41467-020-20251-8
- Partey FD, Obiri D, Bonney EY, Pobee ANA, Dampsey IK, Ennison K, et al. Efficient transplacental transfer of SARS-CoV-2 antibodies between naturally exposed mothers and infants in Accra, Ghana. *Sci Rep* (2024) 14:10772. doi:10.1038/s41598-024-61496-3
- Tapela K, Oporum PC, Nuokpem FY, Tetteh B, Siaw GK, Humbert MV, et al. Development of an affordable ELISA targeting the SARS-CoV-2 nucleocapsid and

its application to samples from the ongoing COVID-19 epidemic in Ghana. *Mol Diagn Ther* (2023) 27:583–92. doi:10.1007/s40291-023-00655-0

39. Bradfute SB, Hurwitz I, Yingling AV, Ye C, Cheng Q, Noonan TP, et al. Severe acute respiratory syndrome coronavirus 2 neutralizing antibody titers in convalescent plasma and recipients in New Mexico: an open treatment study in patients with coronavirus disease 2019. *The J Infect Dis* (2020) 222:1620–8. doi:10.1093/infdis/jiaa505

40. Mensah BA, Ndong IC, Quashie PK, Guichet E, Abuaku B, Effah-Baafi Y, et al. Population-based sero-epidemiological investigation of the dynamics of SARS-CoV-2 infections in the Greater Accra Region of Ghana. *Sci Rep* (2022) 12:21582. doi:10.1038/s41598-022-25598-0

41. Pooley N, Abdool Karim SS, Combadière B, Ooi EE, Harris RC, El Guerche Seblain C, et al. Durability of vaccine-induced and natural immunity against COVID-19: a narrative review. *Infect Dis Ther* (2023) 12:367–87. doi:10.1007/s40121-022-00753-2

42. Dobaño C, Jiménez A, Rubio R, Alonso S, Ramírez-Morros A, Vidal M, et al. Spike-based COVID-19 immunization increases antibodies to nucleocapsid antigen. *Translational Res* (2022) 240:26–32. doi:10.1016/j.trsl.2021.10.004

43. Bradley T, Grundberg E, Selvarangan R, LeMaster C, Fraley E, Banerjee D, et al. Antibody responses after a single dose of SARS-CoV-2 mRNA vaccine. *New Engl J Med* (2021) 384:1959–61. doi:10.1056/nejmc2102051

44. Jarju S, Wenlock RD, Danso M, Jobe D, Jagne YJ, Darboe A, et al. High SARS-CoV-2 incidence and asymptomatic fraction during Delta and Omicron BA.1 waves in the Gambia. *Nat Commun* (2024) 15:3814. doi:10.1038/s41467-024-48098-3

45. Viana R, Moyo S, Amoako DG, Tegally H, Scheepers C, Althaus CL, et al. Rapid epidemic expansion of the SARS-CoV-2 Omicron variant in southern Africa. *Nature* (2022) 603:679–86. doi:10.1038/s41586-022-04411-y

46. Asante IA, Hsu SN, Boatema L, Kwah L, Adusei-Poku M, Odoom JK, et al. Repurposing an integrated national influenza platform for genomic surveillance of SARS-CoV-2 in Ghana: a molecular epidemiological analysis. *The Lancet Glob Health* (2023) 11:e1075–e1085. doi:10.1016/s2214-109x(23)00189-4

47. Chatterjee S, Bhattacharya M, Nag S, Dhama K, Chakraborty C. A detailed overview of SARS-CoV-2 omicron: its sub-variants, mutations and pathophysiology, clinical Characteristics, immunological landscape, immune escape, and therapies. *Viruses* (2023) 15:167. doi:10.3390/v15010167

48. Cao Y, Wang J, Jian F, Xiao T, Song W, Yisimayi A, et al. Omicron escapes the majority of existing SARS-CoV-2 neutralizing antibodies. *Nature* (2022) 602:657–63. doi:10.1038/s41586-021-04385-3

49. Hoffmann M, Krüger N, Schulz S, Cossmann A, Rocha C, Kempf A, et al. The Omicron variant is highly resistant against antibody-mediated neutralization: implications for control of the COVID-19 pandemic. *Cell* (2022) 185:447–56.e11. doi:10.1016/j.cell.2021.12.032

50. Willett BJ, Grove J, MacLean OA, Wilkie C, De Lorenzo G, Furnon W, et al. SARS-CoV-2 Omicron is an immune escape variant with an altered cell entry pathway. *Nat Microbiol* (2022) 7:1161–79. doi:10.1038/s41564-022-01143-7

51. Carreño JM, Alshammari H, Singh G, Raskin A, Amanat F, Amoako A, et al. Evidence for retained spike-binding and neutralizing activity against emerging SARS-CoV-2 variants in serum of COVID-19 mRNA vaccine recipients. *EBioMedicine* (2021) 73:103626. doi:10.1016/j.ebiom.2021.103626

52. Harthaller T, Falkensammer B, Bante D, Huber M, Schmitt M, Benainouna H, et al. Retained avidity despite reduced cross-binding and cross-neutralizing antibody levels to Omicron after SARS-COV-2 wild-type infection or mRNA double vaccination. *Front Immunol* (2023) 14:1196988. doi:10.3389/fimmu.2023.1196988

53. Voysey M, Costa Clemens SA, Madhi SA, Weckx LY, Folegatti PM, Aley PK, et al. Single-dose administration and the influence of the timing of the booster dose on immunogenicity and efficacy of ChAdOx1 nCoV-19 (AZD1222) vaccine: a pooled analysis of four randomised trials. *The Lancet* (2021) 397:881–91. doi:10.1016/s0140-6736(21)00432-3

54. Grunau B, Goldfarb DM, Asamoah-Boaheng M, Golding L, Kirkham TL, Demers PA, et al. Immunogenicity of extended mRNA SARS-CoV-2 vaccine dosing intervals. *JAMA* (2022) 327:279–81. doi:10.1001/jama.2021.21921

55. Prusinkiewicz MA, Sediqi S, Li YJ, Goldfarb DM, Asamoah-Boaheng M, Wall N, et al. Effect of vaccine dosing intervals on Omicron surrogate neutralization after three doses of BNT162b2. *Heliyon* (2023) 9:e17259. doi:10.1016/j.heliyon.2023.e17259

56. Hastert FD, Hein S, von Rhein C, Benz NI, Husria Y, Oberle D, et al. The SARS-CoV-2 variant omicron is able to escape vaccine-induced humoral immune responses, but is counteracted by booster vaccination. *Vaccines* (2022) 10:794. doi:10.3390/vaccines10050794



OPEN ACCESS

*CORRESPONDENCE

Stacey L. Gorniak,
✉ sgorniak@uh.edu

RECEIVED 04 January 2025

ACCEPTED 30 June 2025

PUBLISHED 24 July 2025

CITATION

Gulley Cox LI, Dias N, Zhang C, Zhang Y and Gorniak SL (2025) Impact of aging and body mass index on upper extremity motor unit number index and size.






Exp. Biol. Med. 250:10491.

doi: 10.3389/ebm.2025.10491

COPYRIGHT

© 2025 Gulley Cox, Dias, Zhang, Zhang and Gorniak. This is an open-access article distributed under the terms of the [Creative Commons Attribution License \(CC BY\)](https://creativecommons.org/licenses/by/4.0/). The use, distribution or reproduction in other forums is permitted, provided the original author(s) and the copyright owner(s) are credited and that the original publication in this journal is cited, in accordance with accepted academic practice. No use, distribution or reproduction is permitted which does not comply with these terms.

Impact of aging and body mass index on upper extremity motor unit number index and size

Lauren I. Gulley Cox ¹, Nicholas Dias ², Chuan Zhang ², Yingchun Zhang ² and Stacey L. Gorniak ^{1*}

¹Department of Health and Human Performance, University of Houston, Houston, TX, United States,

²Department of Biomedical Engineering, University of Houston, Houston, TX, United States

Abstract

The focus of this study was to evaluate motor unit number and size across the upper extremity in older adults (aged 60+ years) versus young healthy adults (aged 20–30 years). We hypothesized that older adults would have: fewer motor units and increased motor unit size as compared to young healthy adults (H1), that motor unit size would differ across the upper extremity muscles as compared to young healthy adults (H2), and higher body mass index (BMI) would be associated with lower motor unit numbers (H3). Compound muscle action potential (CMAP), motor unit number index (MUNIX), and motor unit size index (MUSIX) were evaluated in five muscles of the upper extremity. Group differences in CMAP due to aging were accounted for by increased body mass index (BMI); group differences in MUSIX were not impacted by BMI. No difference in MUNIX was found; however, an influence of BMI was found across groups. While this data provides supporting evidence of age-related motor unit changes, body composition changes with age may confound these conclusions when surface electromyography is utilized as the measurement modality. Adiposity estimation should be considered in future EMG studies, particularly in populations with higher BMI values.

KEYWORDS

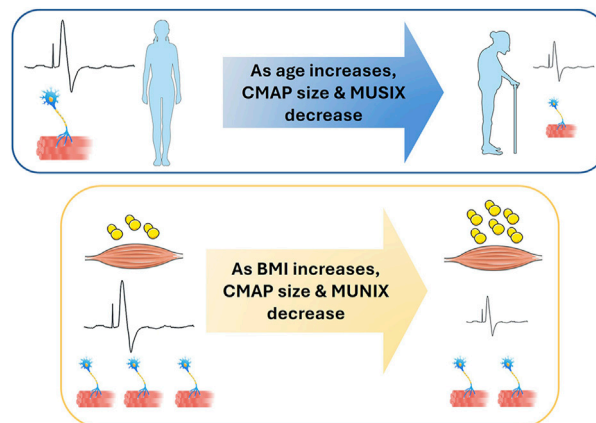
motor unit loss, adiposity, neuromuscular, MUNIX, MUSIX

Impact statement

The data in this project indicate significant changes in motor unit characteristics of the upper extremity in older adults that may be attributable to increased body mass index (BMI) with aging.

Introduction

Motor unit loss is a key characteristic of neuromuscular diseases and motor deficits that are associated with aging [1–5]. At the muscle level, aging is associated with delayed muscle activation in response to stimulus along with altered muscle recruitment—an indicator of



GRAPHICAL ABSTRACT

neuromuscular dysfunction [6]. Despite this, the literature on age-associated neuromuscular dysfunction is inconsistent with data suggesting that muscular alterations are dependent on muscle location and muscle function [2, 7–9].

Work by Dalton et al. [8] did not report differences in motor unit number estimates in select lower extremity muscles between older adults (aged 70+ years) and young healthy adults (aged 20–30 years), concluding there to be no age associated reductions in motor unit number estimates in the lower extremities. Conversely, age associated motor unit loss in muscles of the upper extremity has been reported. Specifically, Brown et al. [7] found subjects over the age of 60 had one half the number of motor units in the biceps brachii as compared to those under 60 years of age. Further investigation by Galea et al. [2] into the number of motor units within the biceps brachii, extensor digitorum brevis, and median innervated thenar muscles did not arrive at the same conclusion, despite reporting diminished peak-to-peak amplitude and reduced area of the maximum M-wave in muscles of the upper extremity with advanced age. Instead, findings from Galea et al. [2] indicate reduced motor unit numbers in distal muscles of the upper extremity; however, supporting data for this conjecture are sparse.

Additional work has shown higher motor unit discharge rates in younger adults via meta-analysis of data collected from the lower extremity; however, variability in methods and muscles assessed in the meta-analysis limits age-related interpretations for the upper extremities [10] in studies that included various upper extremity muscles such as biceps brachii, triceps brachii, abductor digiti minimi, first dorsal interosseus, and extensor digitorum. In contrast, other work indicates more homogeneity of motor unit output primarily in the lower extremities with aging [11]. Taken together, these findings indicate that natural aging affects the neuromuscular system may manifest differently in the upper and lower extremities. These disparities highlight the need for further investigation.

In addition, it is well recognized that body mass index increases (BMI) with age—nearly 1/3 of the US population aged 60+ years meets the BMI criteria for obesity [12]. Increased adiposity (and increased BMI) has been noted as a barrier to muscle tissue assessment via surface electromyography (EMG) [13–15]. It is unclear if increased BMI with age also impacts measured motor unit numbers and estimated motor unit sizes. This inclusion is pertinent given that increased BMI, a common occurrence with aging, could potentially confound the assessment of motor units, blurring the distinction between age-related changes and those due to increased adiposity.

In light of these gaps, the focus of the current study was to evaluate motor unit number and size across the upper extremity in older adults (aged 60+ years) versus young healthy adults (aged 20–30 years). We hypothesized that older adults would have fewer motor units and increased motor unit size in muscles of the upper extremity as compared to young healthy adults (Hypothesis 1), and that motor unit number and size would differ across the upper extremity muscles examined in older adults as compared to young healthy adults (Hypothesis 2). We also hypothesized that BMI would have an impact on CMAP values and motor unit numbers, such that higher BMI values would be associated with lower CMAP values and motor unit numbers, particularly in older adults—as older adults generally exhibit higher BMIs (Hypothesis 3).

Materials and methods

Participants

Thirteen (13) young healthy controls (5M, 8F) and 12 older adult participants (6M, 6F) were recruited for this study from the greater Houston area (population approx. 2.3 million), see Table 1 for demographics. All participants were right-handed (laterality

TABLE 1 Study participant characteristics.

Characteristic	Young	Older adult
N (Males, Females)	13 (6, 7)	12 (6, 6)
Age (y)	24.5 ± 4.0	68.1 ± 4.5
Height (m)	1.635 ± 0.161	1.717 ± 0.099
Mass (kg)	65.07 ± 18.8	89.4 ± 28.7
BMI (kg/m ²)	23.8 ± 3.0	30.3 ± 11.3
LQ	80 ± 18	92 ± 12

Values are mean ± SD or count. BMI, body mass index; LQ, laterality quotient.

quotient (LQ) >40, assessed with the Edinburgh Handedness Inventory). Exclusion criteria for both groups included: diagnosis of Type 1 or Type 2 Diabetes, history of uncontrolled hypertension, history of limb amputation, chemotherapy, or neurological diseases (Alzheimer's Disease, Dementia, Huntington's Disease, Traumatic Brain Injury, Multiple Sclerosis, Parkinson's Disease, Paraproteinemic Demyelinating Neuropathy (PDN), Muscular Dystrophy, Carpal Tunnel Syndrome, Charcot-Marie-Tooth Disorder, and any other neuropathies), and pain in the extremities that limits activities of daily living. This study was approved by the Institutional Review Board (IRB) at the University of Houston in accordance with Declaration of Helsinki. All subjects provided written informed consent.

EMG recording

Multichannel surface EMG was recorded from each muscle using a bioamplifier (FE234 Quad BioAmp, ADInstruments, Colorado Springs, CO, USA) and PowerLab data acquisition system (PowerLab 8/35, ADInstruments, Colorado Springs, CO, USA). Prior to attaching surface electrodes (3M Red Dot 2560 Foam Monitoring Electrodes with Sticky Gel, 3M, Saint Paul, MN, USA), the skin was cleaned with alcohol. Surface electrodes used consisted of diaphoretic solid gel in disc shape; gel disc diameter was 18 mm, size of the electrode was 25 mm × 27 mm inclusive of foam adhesive materials. The longitudinal axis of each of the muscles (abductor pollicis brevis (APB), biceps brachii (BB), extensor digitorum (EDC), flexor digitorum superficialis (FDS), and triceps brachii (TRI)) was identified via palpation. Placement was based on [16]. Two surface electrodes were placed on the muscle belly, along the longitudinal axis of the respective muscle; center-to-center interelectrode distance was 26–30 mm. A reference electrode was placed on a bony process located proximally to the muscle being tested while a ground electrode was placed distally. EMG data was acquired continuously at 1,000 Hz using LabChart software (ADInstruments, Colorado Springs, CO, USA). Any channel crosstalk was inspected manually and electrodes were repositioned if evidence of channel crosstalk was present.

Nerve stimulation and CMAP

Maximum compound muscle action potential (CMAP), a measure that describes the maximal electrophysiological size of the entire motor pool within a muscle, was obtained for each muscle by supra-maximal stimulation of the innervating nerve (APB: median; BB: musculocutaneous; EDC: radial; FDS: median; TRI: radial), with a DS7A muscle current stimulator (Digitimer, United Kingdom). Stimulation intensity generally started around 5–30 mA and was increased in increments of approximately 20% until a maximal response was reached. The duration for a single pulse stimulation was 200 μs. The nerve was then stimulated with 120% of the final intensity to confirm the maximum CMAP was reached and confirmed visually, consistent with [17]. Major differences in the approach employed in the generation of this data set as compared to [18] include the use of 300 ms epochs and standardized electrode placement, as per [16]. The use of 300 ms epochs meets the minimum epoch duration as per [18] to identify tremor, but not the recommended 500 ms. Our data was collected using a standardized electrode placement to ensure reproducibility of the data, in contrast to “electrode placement for CMAP optimization” as endorsed in [18].

Isometric contractions, MUNIX, and MUSIX

For all tasks, participants were seated in a chair facing the testing table with his/her upper arms at approximately 20° of abduction in the frontal plane. The forearm of each participant rested on a padded surface with an elbow angle of approximately 135° in the sagittal plane. The wrist orientation was such that the hand was restrained in a neutral position (neutral flexion/extension, neutral radial/ulnar deviation) during testing. Participants performed isometric contractions via an externally fixed load cell (Model SM-500, Interface Force Measurement Solutions, Scottsdale, AZ, USA) with the hand in: pronation to evaluate TRI and EDC, and in supination to evaluate BB, FDS, and APB. Directionally of the load cell was modified to accommodate force production during testing. Participants performed three maximum voluntary contraction (MVC) trials of 10–15 each, with one minute of rest between trials. The highest MVC force was used to determine the target forces for the submaximal contraction trials. After MVC trials, participants were asked to perform 30-second submaximal isometric contractions each at 5, 15, 25, 50, and 75% MVC. Force produced by the subject was used as visual feedback to maintain the contraction level. This testing procedure was performed for all five muscles (APB, BB, EDC, FDS, and TRI).

The surface EMG interference pattern was recorded throughout each contraction at varying levels of force. Motor unit number index (MUNIX), an electrophysiological measure of the number of motor units within a muscle that is easy to perform

and well tolerated by study participants, was used to estimate the number of motor units contained in each muscle using maximum CMAP produced during voluntary isometric muscle contractions in 300 ms epochs. Additionally, motor unit size was estimated by calculating the motor unit size index (MUSIX), an indicator of the size of motor units within the evaluated motor pool within a muscle, which is derived using MUNIX and CMAP values. Data underwent bandpass filtering (10–450 Hz) prior to analysis. Additional details on how to calculate CMAP, MUNIX, and MUSIX can be found in [19].

Statistical analysis

SPSS version 30.0 (SPSS IBM, New York, NY, USA) was used to perform parametric statistical analyses. Outliers were identified in SPSS using Tukey's method while creating initial boxplots of data. The following # of outliers were removed from the data set as indicated via Tukey's method: CMAP (1 young), MUNIX (2 young, 2 older), MUSIX (5 young, 4 older). For each variable of interest, automatic linear modeling (ALM) was used to select significant covariates (specifically age and BMI) using forward stepwise selection in SPSS [20]. Follow-up correlation analyses were performed for all ALM-identified significant covariates. Data were analyzed using two-way ANCOVAs to compare between *Groups* (T2D and Control). Within-subject factors for neuromuscular evaluation was *Muscle* (APB, BB, EDC, FDS, and TRI) as was a *Group x Muscle* interaction. Regression models between measures of interest (CMAP, MUNIX, and MUSIX) and BMI were calculated in OriginLab 2025 (Northampton, MA, USA) for each group separately.

Results

CMAP

A baseline two-way ANOVA was performed for maximum CMAP amplitude with *Group* (Young and Older Adult) and *Muscle* (APB, BB, EDC, FDS, and TRI) as main factors. *Group* ($F_{1,72} = 6.300$, $p < 0.05$) was found to be significantly different such that the young adult group had significantly larger overall max CMAP amplitude compared to older adults, Figure 1A. No significant main effect of *Muscle* nor *Group x Muscle* interaction were found.

ALM modeling indicated *BMI* as a covariate in the CMAP amplitude model which replaced the *Group* effect, Figure 1B. Follow-up ANCOVA was performed with *Group* and *Muscle* as main factors and *BMI* as a covariate. Only *BMI* ($F_{1,71} = 5.439$, $p < 0.05$) was found to be significant. Increased *BMI* was associated with reduced max CMAP amplitude ($r_{79} = -0.245$, $p < 0.05$). Regression models calculated for each group separately did not show a significant relationship between CMAP and BMI in the

Young group ($p > 0.7$); however, a significant relationship between CMAP and BMI emerged in the Older Adult group ($F_{1,46} = 6.62$, $p < 0.05$), shown in Figure 2A.

MUNIX

A baseline two-way ANCOVA was performed for MUNIX with *Group* (T2D and Control) and *Muscle* (APB, BB, EDC, FDS, and TRI) as main factors. No main effects or interactions were found, Figure 1C.

ALM modeling indicated *BMI* as a covariate in the MUNIX data, Figure 1D. Follow-up ANCOVA was performed with *Group* and *Muscle* as main factors and *BMI* as a covariate. Only *BMI* ($F_{1,68} = 4.701$, $p < 0.05$) was found to be significant. Increased *BMI* was associated with reduced MUNIX ($r_{76} = -0.243$, $p < 0.05$). Regression models calculated for each group separately indicated a nearly significant relationship between MUNIX and BMI in the Young group ($F_{1,31} = 3.03$, $p = 0.09$) and a significant relationship between MUNIX and BMI in the Older Adult group ($F_{1,44} = 4.19$, $p < 0.05$), shown in Figure 2B.

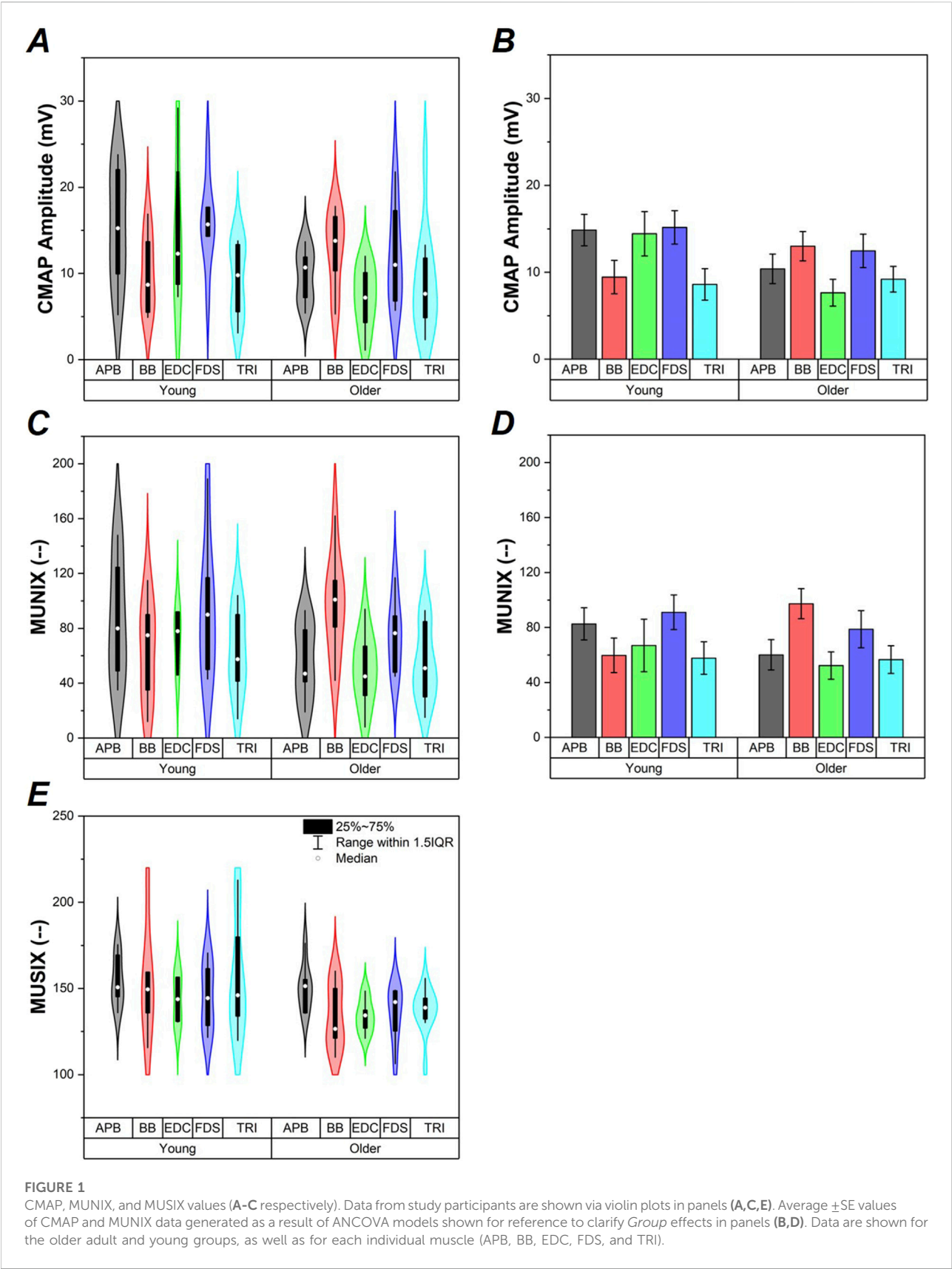
MUSIX

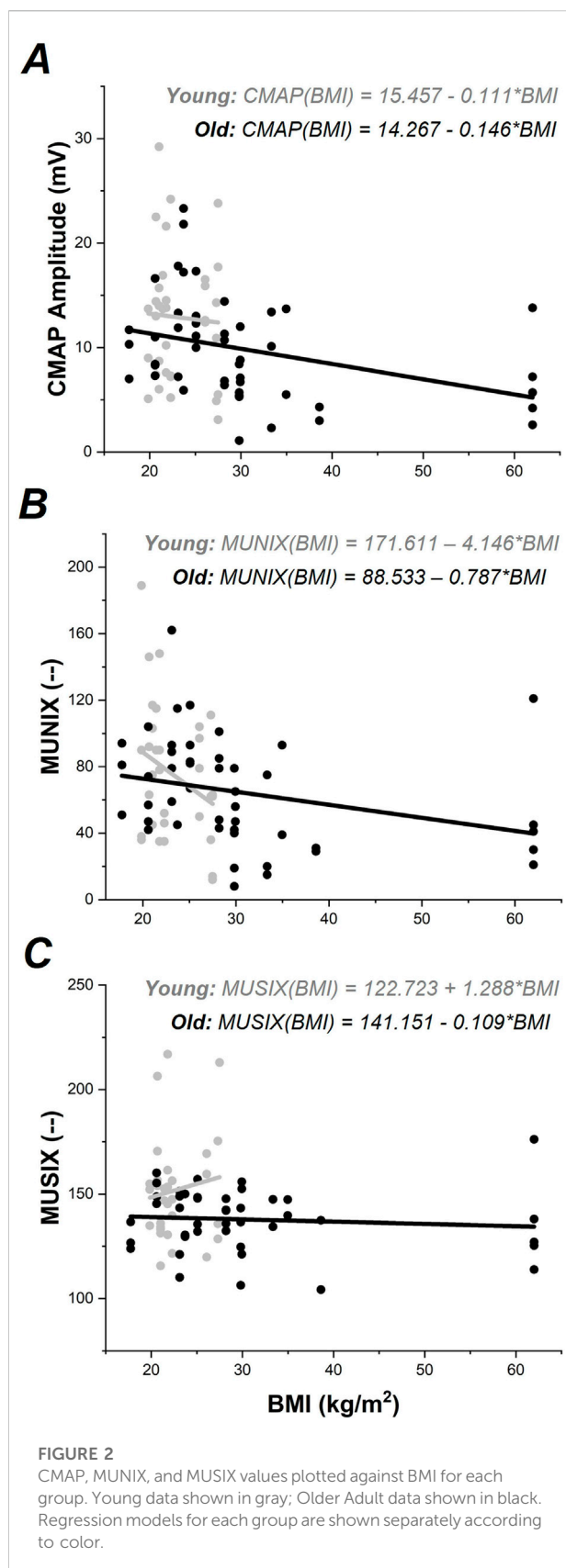
A baseline two-way ANCOVA was performed for MUSIX with *Group* (T2D and Control) and *Muscle* (APB, BB, EDC, FDS, and TRI) as main factors. *Group* ($F_{1,64} = 6.633$, $p < 0.05$) was found to be significantly different such that the young adult group had significantly larger MUSIX compared to older adults, Figure 1E. No significant main effect of *Muscle* nor *Group x Muscle* interaction were found.

ALM modeling did not indicate any significant covariates in the MUSIX data, thus follow-up ANCOVAs were not performed. Regression models calculated for each group separately did not show significant relationships between MUSIX and BMI ($p > 0.5$), Figure 2C.

Discussion

The purpose of this study was to evaluate motor unit characteristics across the upper extremity in older adults (aged 60+ years) as compared to young healthy adults (aged 20–30 years). We hypothesized that older adults would have fewer motor units and increased motor unit size in muscles of the upper extremity as compared to young healthy adults (Hypothesis 1). Overall, this hypothesis was not supported as no age-related changes in MUNIX were found concurrent despite evidence of lower MUSIX in older adults. We also hypothesized that motor unit number and size would differ across the upper extremity muscles examined in older adults





as compared to young healthy adults (Hypothesis 2). This hypothesis was also not supported, as no main effects of *Muscle* were found. In Hypothesis 3, we explored the impact of BMI on CMAP, MUNIX, and MUSIX measures. BMI replaced the age group effect in our CMAP results, was a significant factor in the MUNIX results, but did not impact MUSIX results. The implications of these findings are discussed in the following paragraphs.

The data produced in this study do not support the conjecture that aging is associated with an overall reduction of motor units in the upper extremity. While age-related changes in CMAP values were found between age groups, this difference was accounted for by group differences in BMI—indicating that BMI is an important confounder of electrophysiological activity across the lifespan. This is consistent with emerging reports of increased adiposity as a significant barrier to EMG measurement [13–15, 21, 22], providing a physiological basis for this reported effect. Recent work has indicated that higher amounts of adiposity (generally assessed via BMI) are associated with reduced amplitude of electromyographic (EMG) signals [13–15]. The increased BMI in the older adult group in this study reflects an increase in body mass with aging, as evidenced by Table 1 and Figure 2. This increase in body mass is likely due to increased adiposity concurrent with sarcopenia across the body with age [23]. Increased adiposity with advanced age is preceded by a metabolic cascade, including reduced blood glucose and triglyceride clearance—leading to increased fat deposition within the body as age increases [24, 25]. Increased adiposity results in a thicker insulation layer between the derma and muscle that reduces the strength of EMG signal measured. This in turn reduces the CMAP amplitude measured and impacts any measurements that depend on CMAP measured from surface EMG for computation (e.g., MUNIX and MUSIX). While MUNIX was impacted by BMI in this data set, MUSIX was not—despite a finding of reduced MUSIX values in the older adult group. This is a highly relevant finding, as loss of motor unit number with aging is assumed to precede sarcopenia with advanced age [26]. The data in this paper suggest that the loss of motor unit number may be concurrent with sarcopenia in the upper extremities in older adults.

In order to take into account adiposity-associated EMG signal attenuation in motor unit characterization, adiposity measurement (via dual-energy x-ray absorptiometry (DXA)) or adiposity estimation via BMI should be considered and controlled for statistically in future work, particularly in populations living with higher BMI values due to chronic disease (e.g., cardiovascular disease, stroke, etc.). Use of either DXA or BMI is warranted as attempts to use skinfold thickness to estimate adiposity have been found to be inaccurate, particularly in persons with BMI >30 kg/m [2, 27, 28]; whereas use of either DXA or BMI has produced consistent results with respect to each other in terms of accounting for adiposity impacts in evaluation

of neurological and muscular measurements [21, 22, 29–32]. One way that adiposity as a confound may be accounted for in future work is by creating mathematical or statistical models of adiposity distribution [21, 22] that could be employed in signal processing of EMG data. This approach may aid in distinguishing physiological changes in neuromuscular function from those induced by signal attenuation during EMG measurement due to increased adiposity.

In addition to these findings, none of the measures considered in this project were significantly different based on muscle location. These data are in contrast to work by Galea et al. [2], in which differences in motor unit measures of the distal musculature of the upper extremity (ABP, EDC, FDS) would have been reduced in older adults as compared to motor unit measures in more proximal musculature of the upper extremity (BB). These data support prior findings of [11] in terms of homogeneity of motor unit measures within a limb with aging, in contrast to reports of motor unit loss in the distal musculature with age [2, 33–35]. More work is needed to clarify the physiological mechanisms responsible for distal motor unit changes with age [25]—particularly with the consideration of increased adiposity with age functioning as a confounding factor in EMG measurement.

Conclusion

The data produced in this study do not support the conjecture that aging is associated with a reduction of motor unit number index in the upper extremity; however, evidence to support age-related changes in motor unit size was found. Group differences in CMAP values due to aging were accounted for by increased BMI. The data do not support reports of motor unit loss in distal musculature with age. Adiposity estimation via BMI should be considered and controlled for statistically in future work, particularly in populations living with higher BMI values.

Author contributions

LG: study design, acquisition of data, analysis and interpretation of data, draft of article. ND: acquisition of data, analysis and interpretation of data, revising of article. CZ: acquisition of data, analysis and interpretation of data, revising of article. YZ: study design, interpretation of data, revising of article. SG: study conceptualization and design,

interpretation of data, draft and revision of article. All authors contributed to the article and approved the submitted version.

Data availability

Data analyzed in this project is available from <https://doi.org/10.5281/zenodo.15864514>.

Ethics statement

The studies involving humans were approved by University of Houston Institutional Review Board. The studies were conducted in accordance with the local legislation and institutional requirements. The participants provided their written informed consent to participate in this study.

Funding

The author(s) declare that financial support was received for the research and/or publication of this article. This project was funded by R01 CA200263 via subcontract to SG and 5R56AG080816-01 to SG. Support for materials for this project was provided by the University of Houston GEAR Grant program to SG.

Acknowledgments

The data presented in this manuscript are based on Dr. Gulley-Cox's Ph.D. dissertation.

Conflict of interest

The author(s) declared no potential conflicts of interest with respect to the research, authorship, and/or publication of this article.

Generative AI statement

The author(s) declare that no Generative AI was used in the creation of this manuscript.

References

1. Bromberg MB. Updating motor unit number estimation (MUNE). *Clin Neurophysiol* (2007) **118**:1–8. doi:10.1016/j.clinph.2006.07.304
2. Galea V. Changes in motor unit estimates with aging. *J Clin Neurophysiol* (1996) **13**:253–60. doi:10.1097/00004691-199605000-00010

3. Hara Y, Akaboshi K, Masakado Y, Chino N. Physiologic decrease of single thenar motor units in the F-response in stroke patients. *Arch Phys Med Rehabil* (2000) **81**:418–23. doi:10.1053/mr.2000.3872

4. Hu X, Suresh AK, Li X, Zev Rymer W, Suresh NL. Impaired motor unit control in paretic muscle post stroke assessed using surface electromyography: a preliminary report. In: *2012 annual international conference of the IEEE engineering in medicine and biology society*. p. 4116–9.
5. McNeil CJ, Doherty TJ, Stashuk DW, Rice CL. Motor unit number estimates in the tibialis anterior muscle of young, old, and very old men. *Muscle and Nerve* (2005) **31**:461–7. doi:10.1002/mus.20276
6. Arnold P, Vantieghem S, Gorus E, Lauwers E, Fierens Y, Pool-Goudswaard A, et al. Age-related differences in muscle recruitment and reaction-time performance. *Exp Gerontol* (2015) **70**:125–30. doi:10.1016/j.exger.2015.08.005
7. Brown WF, Strong MJ, Snow R. Methods for estimating numbers of motor units in biceps-brachialis muscles and losses of motor units with aging. *Muscle and Nerve* (1988) **11**:423–32. doi:10.1002/mus.880110503
8. Dalton BH, McNeil CJ, Doherty TJ, Rice CL. Age-related reductions in the estimated numbers of motor units are minimal in the human soleus. *Muscle and Nerve* (2008) **38**:1108–15. doi:10.1002/mus.20984
9. Duque J, Petitjean C, Swinnen SP. Effect of aging on motor inhibition during action preparation under sensory conflict. *Front Aging Neurosci* (2016) **8**:322. doi:10.3389/fnagi.2016.00322
10. Orssatto LBR, Borg DN, Pendrith L, Blazevich AJ, Shield AJ, Trajano GS. Do motoneuron discharge rates slow with aging? A systematic review and meta-analysis. *Mech Ageing Development* (2022) **203**:111647. doi:10.1016/j.mad.2022.111647
11. Kirk EA, Christie AD, Knight CA, Rice CL. Motor unit firing rates during constant isometric contraction: establishing and comparing an age-related pattern among muscles. *J Appl Physiol* (2021) **130**:1903–14. doi:10.1152/jappphysiol.01047.2020
12. Porter Starr KN, Bales CW. Excessive body weight in older adults: concerns and recommendations. *Clin Geriatr Med* (2015) **31**:311–26. doi:10.1016/j.cger.2015.04.001
13. Lanza MB, Balshaw TG, Massey GJ, Folland JP. Does normalization of voluntary EMG amplitude to MMAX account for the influence of electrode location and adiposity? *Scand J Med and Sci Sports* (2018) **28**:2558–66. doi:10.1111/sms.13270
14. Mendez-Rebolledo G, Guzman-Muñoz E, Ramírez-Campillo R, Valdés-Badilla P, Cruz-Montecinos C, Morales-Verdugo J, et al. Influence of adiposity and fatigue on the scapular muscle recruitment order. *PeerJ* (2019) **7**:e7175. doi:10.7717/peerj.7175
15. Ptaszkowski K, Włodarczyk P, Paprocka-Borowicz M. The relationship between the electromyographic activity of rectus and oblique abdominal muscles and bioimpedance body composition analysis - a pilot observational study. *Diabetes Metab Syndr Obes Targets Ther* (2019) **12**:2033–40. doi:10.2147/dmso.s215982
16. Kasman G, Wolf S. Surface EMG made easy: a beginner's guide for rehabilitation clinicians (2022). Available online at: <https://www.noraxon.com/wp-content/uploads/2015/01/nor-19surface-emg-manual.pdf> (Accessed December 13, 2016).
17. Maathuis EM, Henderson RD, Drenthen J, Hutchinson NM, Daube JR, Blok JH, et al. Optimal stimulation settings for CMAP scan registrations. *J Brachial Plex Peripher Nerve Inj* (2012) **7**:4. doi:10.1186/1749-7221-7-4
18. Nandedkar SD, Barkhaus PE, Stålberg EV, Neuwirth C, Weber M. Motor unit number index: guidelines for recording signals and their analysis. *Muscle and Nerve* (2018) **58**:374–80. doi:10.1002/mus.26099
19. Nandedkar SD, Barkhaus PE, Stålberg EV. Motor unit number index (MUNIX): principle, method, and findings in healthy subjects and in patients with motor neuron disease. *Muscle Nerve* (2010) **42**:798–807. doi:10.1002/mus.21824
20. Gorniak SL, Wagner VE, Vaughn K, Perry J, Cox LG, Hernandez AE, et al. Functional neuroimaging of sensorimotor cortices in postmenopausal women with type II diabetes. *Neurophotonics* (2020) **7**:035007–17. doi:10.1117/1.nph.7.3.035007
21. Gorniak SL, Meng H, Pollonini L. Correlation between subcutaneous adipose tissue of the head and body mass index: implications for functional neuroimaging. *Hum Movement Sci* (2022) **85**:102997. doi:10.1016/j.humov.2022.102997
22. Gorniak SL, Meng H, Yazdekhesti S, Pollonini L. Correlation between subcutaneous adipose tissue of the head and body mass index in children and young adults aged 8–19 years: implications for functional neuroimaging. *Exp Biol Med* (2024) **249**:10030. doi:10.3389/ebm.2024.10030
23. St-Onge M-P, Gallagher D. Body composition changes with aging: the cause or the result of alterations in metabolic rate and macronutrient oxidation? *Nutrition* (2010) **26**:152–5. doi:10.1016/j.nut.2009.07.004
24. Carroll MD. *Trends in elevated triglyceride in adults*. United States (2001).
25. Gulley Cox LI, Dias N, Zhang C, Zhang Y, Gorniak SL. Effects of Type II Diabetes on upper extremity muscle characteristics in older adults. *Neurosci Lett* (2025) **844**:138039. doi:10.1016/j.neulet.2024.138039
26. Piasecki M, Ireland A, Jones DA, McPhee JS. Age-dependent motor unit remodelling in human limb muscles. *Biogerontology* (2016) **17**:485–96. doi:10.1007/s10522-015-9627-3
27. Skinfold - an overview. ScienceDirect topics (2023). Available online at: <https://www.sciencedirect.com.ezproxy.lib.uh.edu/topics/medicine-and-dentistry/skinfold> (Accessed October 9, 2023).
28. Watts K, Naylor LH, Davis EA, Jones TW, Beeson B, Bettenay F, et al. Do skinfolds accurately assess changes in body fat in obese children and adolescents? *Med and Sci Sports and Exerc* (2006) **38**:439–44. doi:10.1249/01.mss.00000191160.07893.2d
29. Meng H, O'Connor DP, Lee BC, Layne CS, Gorniak SL. Effects of adiposity on postural control and cognition. *Gait and Posture* (2016) **43**:31–7. doi:10.1016/j.gaitpost.2015.10.012
30. Meng H, O'Connor DP, Lee B-C, Layne CS, Gorniak SL. Alterations in over-ground walking patterns in obese and overweight adults. *Gait Posture* (2017) **53**:145–50. doi:10.1016/j.gaitpost.2017.01.019
31. Meng H, Gorniak SL. Obesity is associated with gait alterations and gait asymmetry in older adults. *Motor Control* (2022) **1**–14. doi:10.1123/mc.2021-0125
32. Meng H, Gorniak SL. Effects of adiposity on postural control and cognition in older adults. *Gait and Posture* (2020) **82**:147–52. doi:10.1016/j.gaitpost.2020.09.004
33. Stalberg E, Fawcett PR. Macro EMG in healthy subjects of different ages. *J Neurol Neurosurg and Psychiatry* (1982) **45**:870–8. doi:10.1136/jnnp.45.10.870
34. Doherty TJ, Vandervoort AA, Brown WF. Effects of ageing on the motor unit: a brief review. *Can J Appl Physiol* (1993) **18**:331–58. doi:10.1139/h93-029
35. Taylor PK. CMAP dispersion, amplitude decay, and area decay in a normal population. *Muscle and Nerve* (1993) **16**:1181–7. doi:10.1002/mus.880161107

Scope

Experimental Biology and Medicine (EBM) is a global, peer-reviewed journal dedicated to the publication of multidisciplinary and interdisciplinary research in the biomedical sciences. The journal covers the spectrum of translational research from T0, basic research, to T4, population health. Articles in EBM represent cutting edge research at the overlapping junctions of the biological, physical and engineering sciences that impact upon the health and welfare of the world's population. EBM is particularly appropriate for publication of papers that are multidisciplinary in nature, are of potential interest to a wide audience, and represent experimental medicine in the broadest sense of the term. However, manuscripts reporting novel findings on any topic in the realm of experimental biology and medicine are most welcome.

EBM publishes Research, Reviews, Mini Reviews, and Brief Communications in the following categories.

- Anatomy/Pathology
- Artificial Intelligence/
Machine Learning Applications
to Biomedical Research
- Biochemistry and Molecular Biology
- Bioimaging
- Biomedical Engineering
- Bionanoscience
- Cell and Developmental Biology
- Clinical Trials
- Endocrinology and Nutrition
- Environmental Health/Biomarkers/
Precision Medicine
- Genomics, Proteomics, and
Bioinformatics
- Immunology/Microbiology/Virology
- Mechanisms of Aging
- Neuroscience
- Pharmacology and Toxicology
- Physiology and Pathophysiology
- Population Health
- Stem Cell Biology
- Structural Biology
- Synthetic Biology
- Systems Biology and
Microphysiological Systems
- Translational Research

Submit your work to Experimental Biology and Medicine at
ebm-journal.org/submission

More information
ebm-journal.org/journals/experimental-biology-and-medicine



**EBM is the official journal of the Society
for Experimental Biology and Medicine**

Experimental Biology and Medicine (EBM) is a global, peer-reviewed journal dedicated to the publication of multidisciplinary and interdisciplinary research in the biomedical sciences.

Discover more of our Special Issues

See more →

Contact

development@ebm-journal.org

See more

ebm-journal.org

publishingpartnerships.frontiersin.org/our-partners

